Performance Analysis of Hybrid Plasmonic Waveguide Devices using Highly
Doped Semiconductors

by:

Md. Omar Faruque

MASTER OF SCIENCE

IN

ELECTRICAL AND ELECTRONIC ENGINEERING

Department of Electrical and Electronic Engineering
Islamic University of Technology (IUT)
Board Bazar, Gazipur-1704, Bangladesh.

November, 2019.

CERTIFICATE OF APPROVAL

The thesis titled '**Performance Analysis of Hybrid Plasmonic Waveguide Devices using Highly Doped Semiconductors**' submitted by Md. Omar Faruque, St. No. 161021005 of Academic Year 2016-17 has been found as satisfactory and accepted as partial fulfillment of the requirement for the Degree MASTER OF SCIENCE IN ELECTRICAL AND ELECTRONIC ENGINEERING on November 08, 2019.

Board of Examiners:

Dr. Rakibul Hasan Sagor (Supervisor)
Assistant Professor,
Electrical and Electronic Engineering Department,
Islamic University of Technology (IUT), Gazipur.

Chairman

Dr. Md. Ruhul Amin (Ex-Officio)
Professor and Head,
Electrical and Electronic Engineering Department,
Islamic University of Technology (IUT), Gazipur.

Member

Dr. Md. Ashraful Hoque
Professor,
Electrical and Electronic Engineering Department,
Islamic University of Technology (IUT), Gazipur.

Member

Dr. Mohammad Rakibul Islam
Professor,
Electrical and Electronic Engineering Department,
Islamic University of Technology (IUT), Gazipur.

Member

Dr. Md. Shah Alam
Professor,
Electrical and Electronic Engineering Department,
Bangladesh University of Engineering and Technology (BUET), Dhaka.
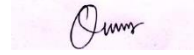
Member (External)

IV

Declaration of Candidate

It is hereby declared that this thesis report or any part of it has not been submitted elsewhere for the award of any Degree or Diploma.

_____
Dr. Rakibul Hasan Sagor
Assistant Professor,
Electrical and Electronic Engineering Department,
Islamic University of Technology (IUT).
Date: November 08, 2019.

_____
Md. Omar Faruque
Student No.: 161021005,
Academic Year: 2016-17.
Date: November 08, 2019.

Dedicated to my family members.

Table of Contents

List of Figures

List of Tables

List of Abbreviation of Technical Terms

MIM	**:**	**M**etal **I**nsulator **M**etal
IMI	**:**	**I**nsulator **M**etal **I**nsulator
CMOS	**:**	**C**omplementary **M**etal **O**xide **S**emiconductor
RI	**:**	**R**efractive **I**ndex
RIU	**:**	**R**efractive **I**ndex Unit
SOI	**:**	**S**ilicon **o**n **I**nsulator
Ag	**:**	Silver
Au	**:**	Gold
Si	**:**	**Si**licon
FEM	**:**	**F**inite **E**lement **M**ethod
PIC	**:**	**P**hotonic **I**ntegrated **C**ircuit
FOM	**:**	**F**igure **o**f **M**erit
PCF	**:**	**P**hotonic **C**rystal **F**iber

ACKNOWLEDGEMENT

First and foremost, I offer gratitude to the Almighty Allah (SWT) for giving me the capability to do this work with good health.

I am grateful to my research supervisor, Dr. Rakibul Hasan Sagor, Assistant Professor of Electrical and Electronic Engineering department of Islamic University of Technology (IUT) for the support and guidance throughout the course of this work. He created a research environment for which I was able to explore many ideas without constraint. I have gained a wealth of knowledge and experience in science and engineering through his direction that is beyond value to my future endeavors.

I would like to thank all the faculty members of the department of EEE, IUT for their inspiration and help.

And last but not the least I am thankful to my family, friends and well-wishers for their support and inspiration. Without them it would never have been possible for me to make it this far.

<div align="right">

Md. Omar Faruque

November, 2019.

</div>

ABSTRACT

In this work, an investigation is made to find an alternative material for metals in plasmonic devices in order to overcome the drawbacks of plasmonic devices formed using conventional plasmonic metals like gold and silver. The plasmonic devices formed with gold and silver have a number of limitations in dealing with optical losses, nanofabrication, tunability, chemical stability, and compatibility with conventional manufacturing processes. Thus, to find a suitable replacement, plasmonic properties of gold and silver are studied and materials with similar properties are searched. As a potential alternative material to gold and silver, heavily doped silicon is mathematically modeled and the theoretical model is compared with experimentally obtained data in order to verify the theoretical modeling. The verified model is compared with metals and the plasmonic properties of heavily doped silicon are found similar to those of metals. The material is then defined with the verified model and waveguide is formed using heavily doped silicon instead of metal. The transmission characteristics of the newly formed waveguide are compared with conventional gold and silver waveguide and the suitable material is selected for designing plasmonic devices. Two plasmonic refractive index sensors are investigated numerically and optimized for obtaining a better result. The first refractive index sensor has a highest sensitivity of 1208.9 nm/RIU and the other one has a highest sensitivity of 4900 nm/RIU which is the highest sensitivity reported for plasmonic refractive index sensor to the best of my knowledge. Both the sensors have resolution as small as 0.005. Moreover, the sensors have very simple structures, one with gratings in a straight waveguide and the other with a ring resonator and thus are suitable for being integrated in optical integrated circuits. However, the main advantage of these devices is that, they use only silicon instead of metals like gold or silver which makes them similar to SOI devices and thus, they become compatible with CMOS technology.

CHAPTER 1

INTRODUCTIONTO PLASMONICS AND PLASMONIC DEVICES

1.1   Surface Plasmon Polaritons (SPPs)

Surface Plasmon Polaritons (SPPs) are infrared or visible frequency electromagnetic waves which travel along a metal-dielectric interface [1]. The term "surface plasmonpolariton" explains that the wave involves both charge motion in the metal ("surface plasmon") and electromagnetic waves in the air or dielectric ("polariton"). Whenever there is an interaction between light and a metal, the free electrons inside the metal produce a wave of charges called the surface plasmon.
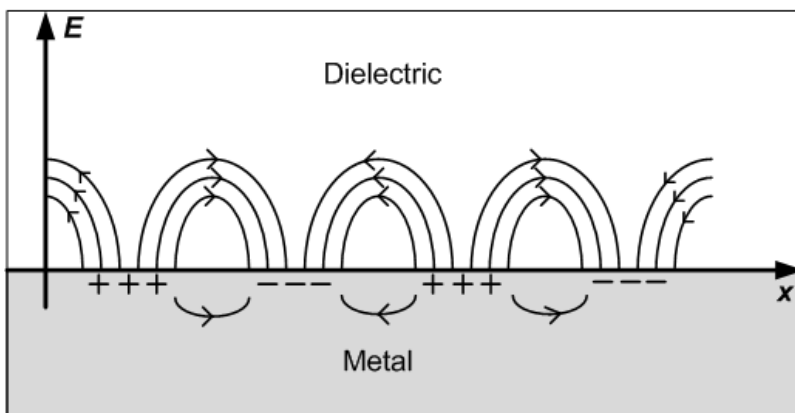
Figure 1.1: Propagation of SPP along metal-dielectric interface.

Diffraction limit is one of the critical factors for the minimization of optical devices [2, 3]. To overcome this diffraction limit in nanophotonic devices and Photonic Integrated Circuits (PICs), SPPs are utilized. SPPs can also confine electromagnetic field to a metal-dielectric interface which allows for nanofocusing with tremendous field enhancement [4, 5]. Thus propagation of SPPs is the basis of all plasmonic applications.

1.2　Plasmonic Waveguides

Although a number of geometrical structures can be formed in order to guide SPPS, most common structures are the Insulator-Metal-Insulator (IMI) and Metal-Insulator-Metal (MIM) waveguides. Since light confinement is one of the key issues in case of plasmonic waveguides, MIM structures are more popularly used compared to IMI structures due to their ability to guide light with high confinement. Silver and gold are the most common metals used as the metal of the MIM structure due to their small ohmic loss or high DC conductivity. Besides Copper can also support SPP propagation and thus can be used to form the plasmonic waveguide. As the insulator, air is mostly used. Silicon, Silicon-di-oxide, Silicon Nitride, etc. are also used sometimes instead of air.

1.3　Plasmonic Devices

Electronic devices suffer from intrinsic delay and large heat generation, which can be solved using the plasmonic devices that lead to high speed, high capacity, and low loss components [6]. Thus, plasmonic waveguide devices are being considered as one of the most suitable alternatives due to their small size, low cost, and high performance. Plasmonic devices also have the capability to process information faster and efficiently compared to electronic devices. Since the scaling of the nanoelectronic components is becoming difficult day by day due to the increasing demand for higher processing speed, plasmonic devices can play a vital role in the applications related to information processing.

Considering Plasmonics as one of the potential replacement of electronics, different types of plasmonic devices are proposed and investigated both numerically and experimentally. These devices include filters [7-9], couplers [10-12], splitters [13-15], sensors [16-18], Bragg reflectors [19-21], Mach–Zehnder interferometers [2, 22-24], etc.

1.3.1 Plasmonic Filters

The plasmonic filter is one of the most important components in the field of signal processing. Plasmonic filters can be used to pass only a desired frequency spectrum of a signal or to remove any unwanted portion from a signal. Thus, it may have a wide range of applications in the field

of wireless communications, radar, etc. [25, 26]. Plasmonic filters have a number of advantages compared to the conventional frequency-selective filters, especially in terms of bandwidth, tunability, and quality factor. A number of plasmonic filters are proposed by the researchers to date. Most of the plasmonic filters are based on ring resonator structure (circular ring, rectangular ring, hexagonal ring, etc.) coupled with a straight waveguide. Figure 1.2 shows some of the proposed plasmonic filters.
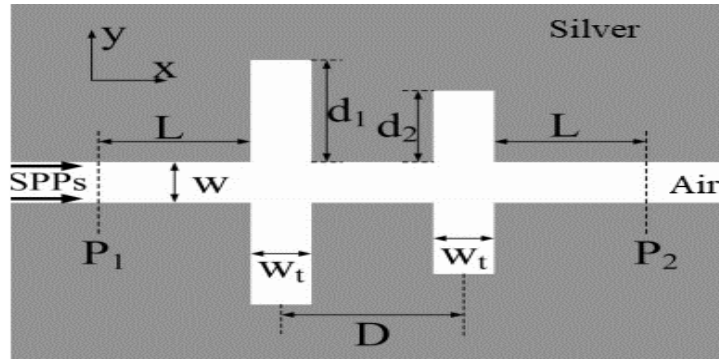
(a)
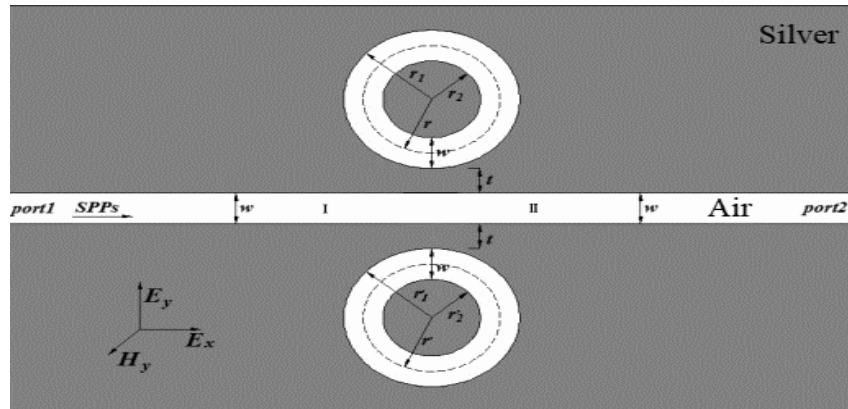
(b)

Figure 1.2: Plasmonic filters proposed by (a) Wang et al. [8], (b) Liu et al. [27].

1.3.2 Plasmonic Couplers

One of the main objectives of plasmonic devices is the guidance of the optical signal along the waveguide. In order to guide optical or light signals efficiently, various types of waveguides such as photonic crystal fiber (PCF), silicon wire waveguides, metallic wires or stripe waveguides,

3

hybrid plasmonic waveguides, plasmonic slot waveguides, etc. are proposed by the researchers. Since different types of waveguides are there, one of the fundamental issues is to couple the light signal between different types of waveguides. In order to couple light signal efficiently between two types of waveguides, a coupler with a high coupling coefficient or coupling efficiency is desirable. Thus, a number of couplers have been demonstrated both numerically and experimentally [9, 28-30]. One of the proposed SPP based coupler is shown in Figure 1.3.
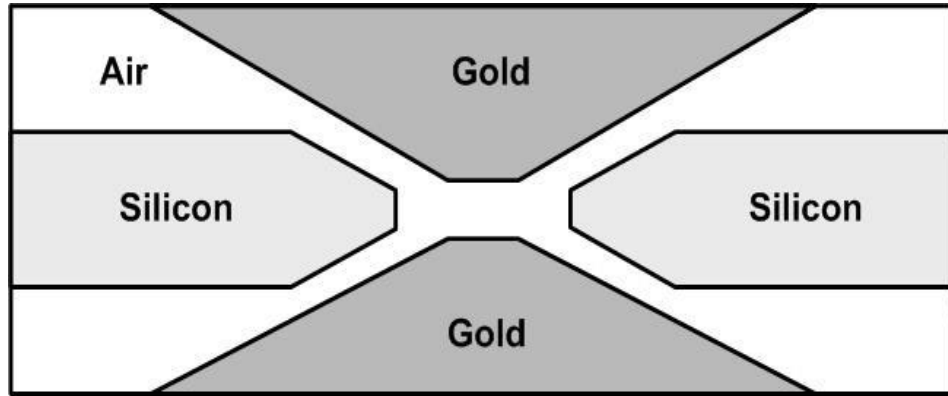
Figure 1.3: Surface Plasmon Polariton coupler proposed by Tian et al. [9].

1.3.3 Plasmonic Splitters

In different types of plasmonic devices, the light signal propagation needs to be controlled in a specific direction, sometimes needs to be split into a certain proportion or the polarization needs to be controlled. In order to meet the above-mentioned demands, plasmonic power splitters, polarization beam splitters, etc. are playing a vital role. In this kind of plasmonic devices, the input signal is fed through the input port, and the desired output signal is obtained at one or more output port. In between the input and output port, the signal is processed using different types of device structures to have the desired output. Till date, a number of plasmonic splitters have been proposed by the researchers which include splitters based on slot cavity, splitters based on dielectric coupler, splitters based on hybrid plasmonic waveguide, etc. [13, 31-33]. Figure 1.4 shows a plasmonic splitter based on slot cavity.
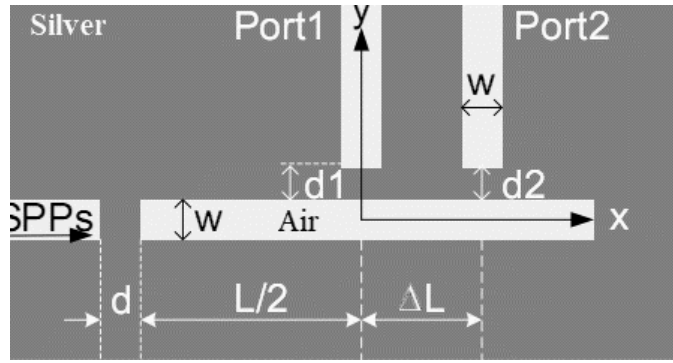
Figure 1.4: A plasmonic splitter based on slot cavity proposed by Guo et al. [13].

1.3.4 Plasmonic Sensors

Among the plasmonic devices, plasmonic sensors have drawn much attention due to their smaller size along with high sensitivity which makes them suitable for integrated optical systems [34]. Most of the plasmonic sensors are based on metal-insulator-metal waveguide along with a resonator which uses different resonance phenomenon and thus acts as different kinds of sensors such as refractive index sensors [17, 18, 35], temperature sensors [35-37], gas sensors [38, 39], biosensors [15, 40, 41]. The main objectives of the researchers are to improve the sensitivity, figure of merit (FOM), resolution of the sensor. Some of the already proposed plasmonic sensors have very high sensitivity. Since plasmonic sensors need to be integrated into other optical circuits, one of their main requirements is to be compatible with the optical circuit system where it needs to be integrated. Figure 1.5 shows one of the plasmonic refractive index sensor and temperature sensor with a highest sensitivity of 3460 nm/RIU and 1.36 nm/°C, made with a silver-air waveguide structure coupled with a ring resonator to hold the material under sensing.
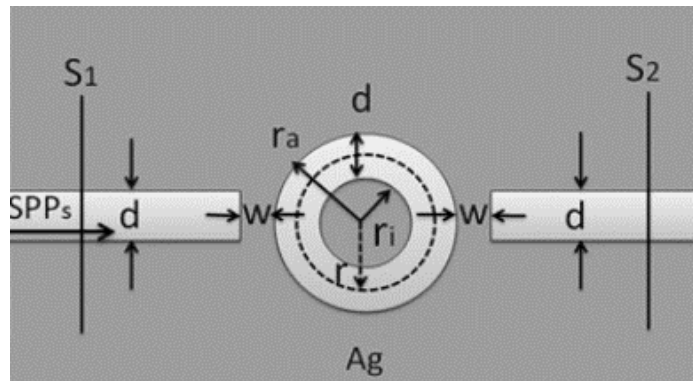
Figure 1.5: Refractive index sensor proposed by Wu et al. [35].

1.3.5 Plasmonic Bragg Reflectors

Bragg reflectors are another class of plasmonic devices which is mainly based on a low refractive index dielectric material (e. g. air) sandwiched by a metal cladding (e.g., silver) and another layer of high index material (e. g. silicon) [42]. Bragg reflectors have found a number of applications in photonic integrated circuits, especially in forming micro cavities, a defect within a Bragg reflector [43, 44]. Plasmonic Bragg reflectors commonly have metal-insulator-metal structures. Hybrid plasmonic Bragg reflectors may also have metal-insulator-semiconductors structures [19]. The main parameters to look for a better Bragg reflector is the loss, ripple factor, bandwidth, and Q factor. Till date, researchers have proposed a number of Bragg reflectors to optimize the parameters [19-21]. Plasmonic Bragg reflectors with two similar structures are shown in Figure 1.6.

(a)

(b)
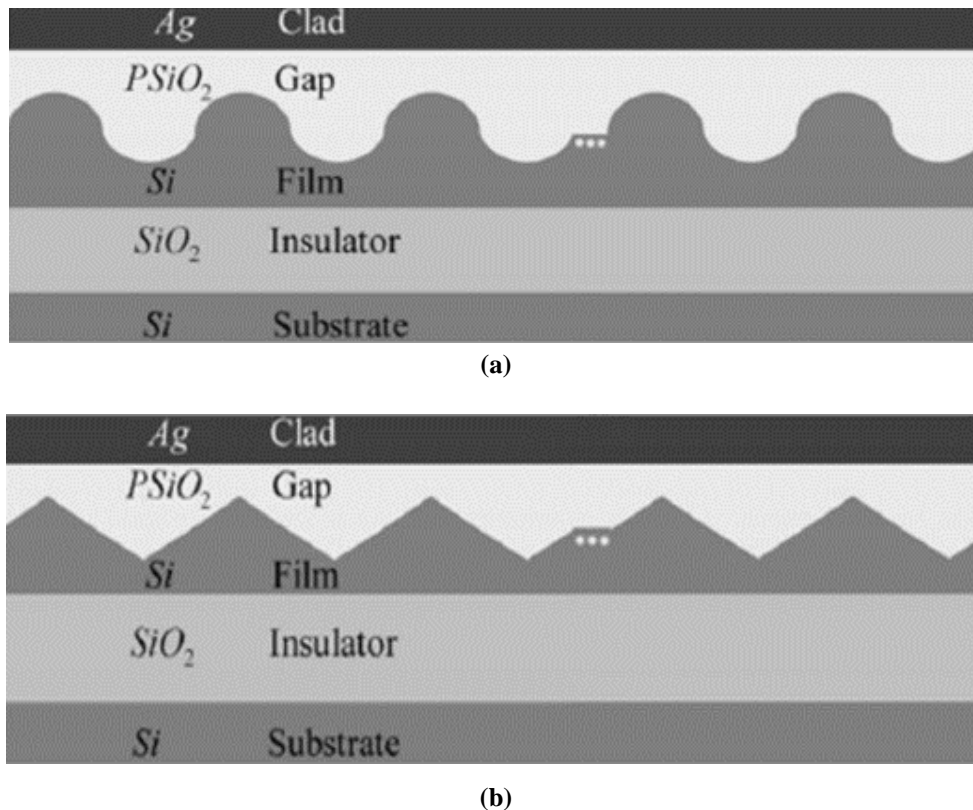
Figure 1.6: Bragg reflector proposed by Daneshmandi et al. [19] with (a) sinusoidal gratings, (b) triangular gratings.

1.3.6 Plasmonic Mach-Zehnder Interferometers

Plasmonic Mach-Zehnder interferometers are the devices which can be used for various other applications like directional coupling [2], optical modulation [22], optical Sensing [23], boisensing [24] etc. Most of the surface plasmon polariton based Mach-Zehnder interferometers are designed with MIM structure. The schematic map of one of such structures is shown in Figure 1.7. Other Mach-Zehnder interferometers may have different structures depending on applications.
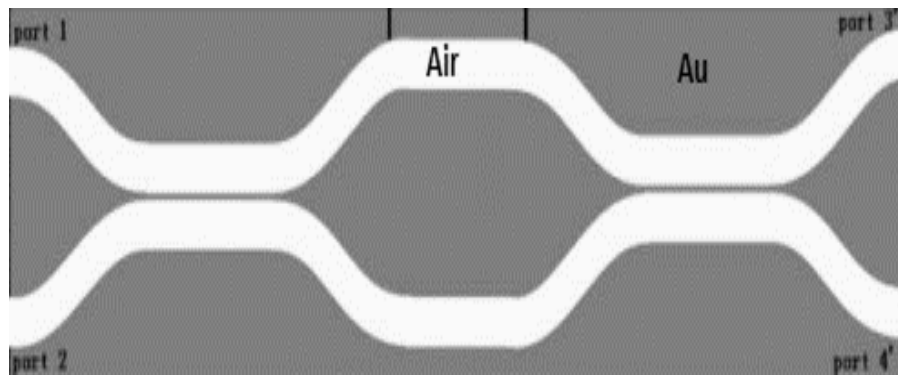
Figure 1.7: Schematic map of a Mach–Zehnder interferometer (MZI) composed of two optical directional couplers proposed by Han et al. [2].

1.3.7 Other Plasmonic Devices

Other plasmonic devices include plasmonic phase modulators [45], plasmonic lens [46], plasmonic nanoantennas[47], plasmonic solar cells [48], absorption switches [49], absorbers [50], nanowires [51], demultiplexers [52, 53] etc. Though most of these plasmonic devices are based on MIM structures, Silicon on Insulator (SOI) based structures are also drawing a lot of attention nowadays due to their compatibility with CMOS technology. Researchers are also proposing hybrid plasmonic devices by making a combination of plasmonic and SOI structures.

1.4   Literature Review

To replace slow electronic circuits by a fast and efficient alternative has been the prime aim of the researchers for a long time. The field of plasmonics is drawing a lot of attention in recent times, although it is originated a long time ago [1, 54, 55]. Since the beginning of the development of plasmonics, material technology is playing a vital role in its development

process. A suitable plasmonic material that can provide advantages in design, fabrication, integration in ICs, tunability can cause a revolution in the field of plasmonics like silicon revolutionized the microelectronics industry. Researchers have tried a number of different alternative materials to design plasmonic devices over the last decades. The contributions from different researchers over the last ten years have been shown in Table 1.1.

Table 1.1: Contribution of the researchers in finding alternative plasmonic materials.

Researchers	Contribution	Year
J. Tian et al. [9]	Tried to improve the efficiency by using the metal-silicon interface instead of the metal-air interface.	2009
Ferreiro-Vila et al. [56]	Tried to improve magneto-optical and plasmonic effects using Ag/Co/Ag layered structures.	2009
P. R. West et al. [57]	Discussed the problems with metals and suggested alternative plasmonic materials more efficient than metals.	2010
Blaber et al. [58]	Reviewed the optical properties of alloys and intermetallics for plasmonics.	2010
Ciattoni et al. [59]	Studied plasmonic devices with memory and power-switching functionalities based on ε-near-zero nonlinear metamaterials.	2011
Naik et al. [60]	Made a comparative study of semiconductor-based plasmonic metamaterials.	2011
Grigorenko et al. [61]	Made a review on graphene plasmonics.	2012
Tokarev et al. [62]	Investigated tunable plasmonic nanostructures from noble metal nanoparticles and stimuli-responsive polymers.	2012
Kim et al. [63]	Optimized Al-doped ZnO films for low loss plasmonic materials at telecommunication wavelengths.	2013
L. Gao et al. [64]	Used hybrid plasmonic waveguide to reduce loss.	2013
Zuccon et al. [65]	Presented and characterized palladium metal films for plasmonic devices.	2014
Cao et al. [66]	Made a review on transparent electrodes for organic optoelectronic devices.	2014
Zhong et al. [67]	Made a review of mid-infrared plasmonic materials which includes transparent conducting oxides, silicides, doped semiconductors, graphene, etc.	2015

Researchers	Contribution	Year
D. Y. Fedyanin et al. [68]	Used CMOS copper waveguide to design an ultra-low loss waveguide.	2015
Wei et al. [69]	Designed plasmonic band-stop filters based on graphene metamaterial.	2016
Song et al. [70]	Proposed an efficient excitation of multiple plasmonic modes on three-dimensional graphene.	2016
Heni et al. [71]	Suggested hybrid material approach using Silicon–Organic and Plasmonic–Organic hybrid Photonics.	2017
Y. Ding et al. [72]	Designed low loss, efficient waveguide using graphene.	2017
Hanske et al. [73]	Suggested silica coated plasmonic metal nanoparticles in plasmonic devices.	2018
Xia [74]	Proposed 2D Materials (graphene, hexagonal boron nitride)-coated plasmonic structures.	2018
Secondo et al. [75]	Proposed a reliable modeling of ultrathin alternative plasmonic material, titanium nitride.	2019

1.5   Thesis Objectives

The main thesis objective is to find a suitable alternative of plasmonic metals which can overcome the limitations of conventional plasmonic metals and to design plasmonic devices using that material. However, more particularly, the objectives include:

- Study of the conventional plasmonic metals and their optical properties.
- To find an alternative material to conventional plasmonic metals.
- Mathematical modeling of that material using already established material models.
- Comparison of the theoretical model properties with the experimental result in order to validate the model.
- To form plasmonic waveguide with the alternative plasmonic material investigated and analyzing the transmission characteristics of the waveguide.
- To design plasmonic devices using the newly designed waveguide and modify the design to achieve better performance.

1.6   Thesis organization

The first chapter of this book, **Chapter 1**, gives a brief introduction about the basics of Plasmonics, plasmonic waveguides, and different plasmonic devices. Contribution from the researchers in the field of plasmonic material technology to date and the outline of this thesis is also described here.

Chapter 2 discusses the conventional plasmonic materials those are used at present in forming plasmonic devices, their plasmonic properties, etc. The problems with conventional plasmonic materials are also discussed here.

In **Chapter 3**, some possible alternatives to conventional plasmonic metals are presented. Their mathematical modeling is done, the theoretically obtained result is compared with the experimentally obtained result, and the model is thus validated. The plasmonic properties are also compared with conventional metals, and the advantages of the designed materials are discussed.

In **Chapter 4**, the newly modeled plasmonic materials are used to form plasmonic waveguides with suitable structures. The transmission characteristics of the waveguides are studied, and the comparison is made with the conventional plasmonic waveguides. This chapter includes the simulation results of the transmission characteristics of the newly designed waveguides simulated using commercial simulation software COMSOL Multiphysics.

Chapter 5 deals with the designing of plasmonic devices utilizing the newly designed plasmonic waveguides using alternative plasmonic materials. The simulation results are compared with the conventional plasmonic devices, and the devices are modified to achieve better performances.

In the last chapter, **Chapter 6**, Conclusion is made about the best plasmonic material investigated here. Other plasmonic devices that can be designed using the material are also suggested, and the future scopes of the research have been discussed.

CHAPTER 2

CONVENTIONAL PLASMONIC MATERIALS AND THEIR PROPERTIES

Material technology is playing a vital role in the recent development of plasmonics and plasmonic devices. SPPs are created depending mostly on the plasmonic property of a material once light is incident on it. Besides, the propagation of SPP is greatly affected by the plasmonic property. Plasmonic materials also act as the building block while realizing the plasmonic devices practically. Thus, in order to have a realizable plasmonic device with good performance, a suitable plasmonic material is the most important thing to look for.

2.1 Plasmonic Properties

Since plasmonic materials are mainly used for their ability to interact with light, their plasmonic properties can be described by two parameters, dielectric permittivity, ε and, magnetic permeability, μ [76]. However, at optical frequencies, the permeability value becomes close to unity. Thus, their behavior can adequately be described by the dielectric permittivity only.

The dielectric permittivity of metal is a complex parameter which has got a real part (ε_1) and an imaginary part (ε_2). The real part accounts for the polarization response of the material, and the imaginary part is responsible for the optical loss. At optical frequencies, the real part of the dielectric permittivity of metal is negative, which is one of the most important plasmonic properties of metals [77]. This negative real part of the permittivity creates SPPs when the material is interacted with light and also supports the propagation of SPPs at the interface. Thus, in order to be used in plasmonic devices, a material must have a negative real part of the complex permittivity.

2.2 Material Models

The optical properties of metallic films have been thoroughly investigated by Rakic et al. [78] and the modeling parameters have been found for eleven metals, including mostly used plasmonic metals, silver, and gold. The optical constants for metals like gold, silver, chromium, titanium, and aluminum has been found by Barchiesi et al. [79]. The material modeling is mainly done using two of the most widely used material models, namely the Drude model and the Lorentz-Drude model.

2.2.1 Drude model

The complex dielectric permittivity of plasmonic metals like gold and silver can be given by the Drude model[34].

$$\varepsilon_D(\omega) = \varepsilon_\infty - \frac{\omega_D^2}{\omega(\omega + i\gamma_D)} \quad \text{...............................} (2.1)$$

where, ω_D is the bulk plasma frequency and γ_D is the intraband damping term (inverse of the relaxation time τ), ε_∞ is the relative permittivity for high frequencies and i is theimaginary unit. The term ω_D can be calculated using the formula,

$$\omega_D = \sqrt{\frac{N_e q^2}{\varepsilon_0 m_0}} \quad \text{................................} (2.2)$$

where, N_e is the density of electrons that contribute to the optical properties, q is the charge of an electron, m_0 is the electron mass, and ε_0 is the relative permittivity of vacuum.

2.2.2 Lorentz-Drude model

The Drude model given by (2.1), considers only intraband electronic transitions without considering the interband transitions [79, 80]. The Lorentz-Drude model combines both the intraband and interband transitions of electrons. The frequency-dependent complex dielectric permittivity of the Lorentz-Drude model given by,

$$\varepsilon_{LD}(\omega) = \varepsilon_{\infty} - \frac{\omega_D^2}{\omega(\omega + i\gamma_D)} - \frac{\Delta\varepsilon\omega_L^2}{\omega^2 - \omega_L^2 + i\gamma_L\omega} \quad \ldots\ldots\ldots\ldots(2.3)$$

where, The plasma frequency ω_L is associated with intraband transitions, $\Delta\varepsilon$ is the oscillator strength and γ_L is the damping term.

2.3   Plasmonic Properties of Silver

The The values of different parameters of (2.1) and (2.3) for silver are obtained by Barchiesi et al. [79] and given in Table 2.1.

Table 2.1: Different parameters of Drude model and Lorentz-Drude model and their values for silver.

Parameters	Value
ε_{∞}	0.114773
ω_D	1.32589×10^{16} rad/s
γ_D	7.05499×10^{15} rad/s
$\Delta\varepsilon$	3.62762
ω_L	41.58116×10^{16} rad/s
γ_L	1.04632×10^{14} rad/s

The complex permittivity of silver is calculated using (2.1) and (2.3) and taking values from Table 2.1. The real part and imaginary parts are separated for different wavelength for both the Drude model and the Lorentz-Drude model and plotted in Figure 2.1.

Figure 2.1 shows that the real part of the permittivity of silver is negative, which is essential for the production and propagation of SPP. The magnitude of the real part is very large compared to the real permittivity of the dielectric, which causes unbalanced polarization response. The magnitude of the imaginary part is also large enough to cause a considerable amount of optical loss.

13
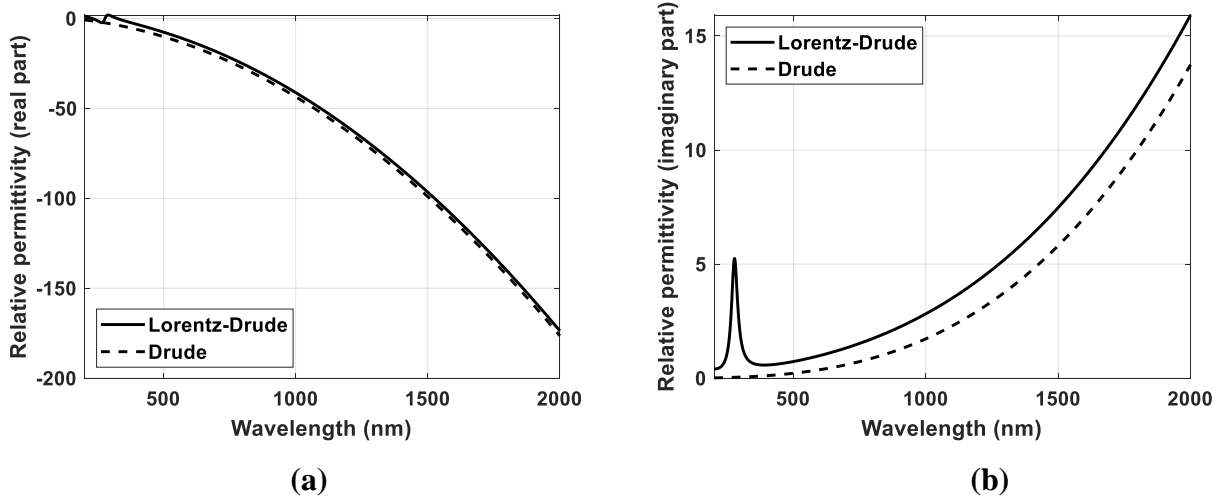
Figure 2.1: Relative permittivity of silver (a) real part, (b) imaginary part using the Drude model and Lorentz-Drude model.

2.4 Plasmonic Properties of Gold

The values of different parameters of (2.1) and (2.3) for gold are also obtained by Barchiesi et al. [5, 79] and given in Table 2.2.

Table 2.2: Different parameters of the Drude model and Lorentz-Drude model and their values for gold.

Parameters	Value
ε_∞	6.90939
ω_D	1.38147×10^{16} rad/s
γ_D	1.75628×10^{15} rad/s
$\Delta\varepsilon$	2.31858
ω_L	4.68266×10^{15} rad/s
γ_L	3.60439×10^{14} rad/s

The complex permittivity of gold is calculated using (2.1) and (2.3) and taking values from Table 2.2. The real part and imaginary parts are separated for different wavelength for both the Drude model and Lorentz-Drude model and plotted in Figure 2.2.

14
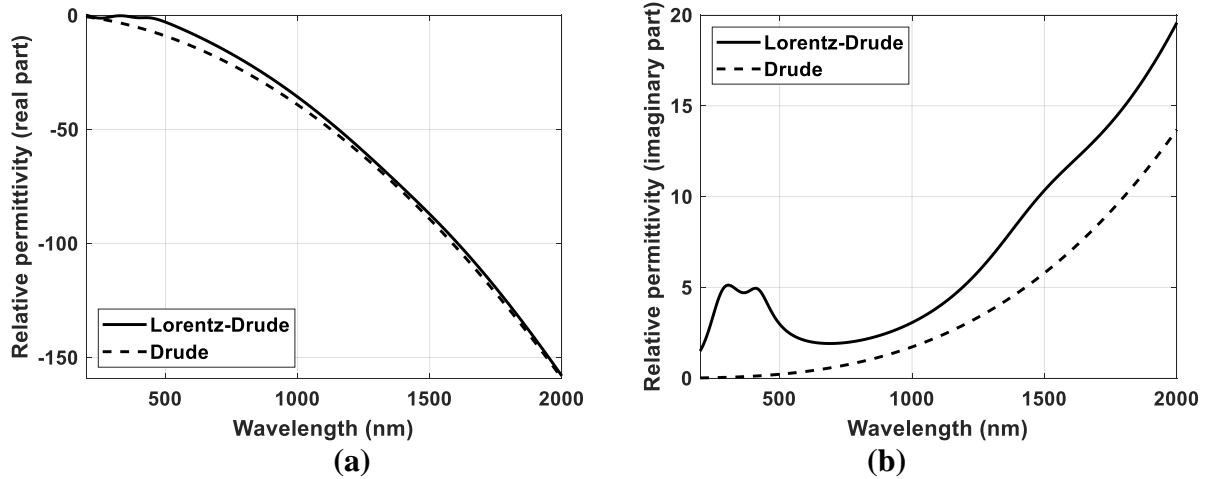
Figure 2.2: Relative permittivity of gold (a) real part, (b) imaginary part using the Drude model and Lorentz-Drude model.

As observed in Figure 2.2, the plasmonic properties of gold are similar to those of silver and thus will face similar kind of drawbacks in plasmonic devices.

2.5 Problems with Conventional Plasmonic Materials

Though metals like gold and silver are mostly used materials in plasmonic applications due to their ability to produce and guide SPPs, they have a number of disadvantages. These disadvantages of natural metals like gold and silver limit the performances of the plasmonic devices to a great extent. Performance parameters like optical loss increases, the tunability of the device reduces, and the fabrication becomes difficult. These performance parameters are discussed below:

(i) Optical loss

One of the main disadvantages of conventional plasmonic materials is that they suffer a substantial optical loss due to the large imaginary part of the complex dielectric permittivity. At optical frequencies, loss mechanisms like interband transitions, intraband transitions, and scattering losses play a crucial role [81]. The interband and intraband transitions occur due to the transition of valence band electrons into another band due to the absorption of energy when light is incident on it, and the scattering losses occur due to the defects in the solids. A higher amount of these three above mentioned losses makes the imaginary part of the complex permittivity

15

larger. From the plasmonic property of gold and silver, it is seen that both of the metals have a large imaginary part of the dielectric permittivity. As a result, the plasmonic devices formed by the materials suffer a huge optical loss.

(ii) Tunability

Gold and silver are the plasmonic materials found in nature. Natural metals have a fixed carrier concentration in the range of 10^{23} cm^{-3}. Due to their high carrier concentration, the real and imaginary part of the complex dielectric permittivity is very large compared to insulators. The large value of the real part of the permittivity causes many problems in plasmonic devices which require a balanced polarization response [82]. The large value of the imaginary part gives rise to a higher optical loss. Both of these values will be reduced if the carrier concentration could be reduced, and the above-mentioned problems may be solved. Besides, many other plasmonic applications may require a larger or smaller value of both the real part and imaginary part of the permittivity. However, the carrier concentration is fixed for natural metals which makes the permittivity values also fixed. Thus, not having adjustable carrier concentration, hence, not adjustable dielectric permittivity, limits natural metals like gold and silver from many plasmonic applications.

(iii) Nanofabrication challenges

In most of the plasmonic devices, metals are used as very thin films. The morphology of metal film is quite different from the bulk metal. Bulk metal is generally composed of larger grains compared to the much smaller grains of thin metal films. Thus, metal films grown or deposited on the substrate do not have the same optical properties as expected [83-85]. Also, in the case of thin-film, smaller grains cause grain-boundary scattering loss in metals [86, 87]. Optical losses in thin metal films can be three to four times more due to grain-boundary scattering loss. The optical loss also arises in ultrathin metal films due to surface roughness [88, 89]. To overcome the challenges, some special technology like wetting layer [90] can be used. However, this kind of special approach has some limitations regarding integration and scalability.

(iv) Chemical instability

Conventional plasmonic metals like gold, silver, or copper are chemically highly reactive. They easily react with air or oxygen present in air and humidity and forms compounds. Copper forms oxides in the air [91, 92] and silver is sensitive to sulfur and forms silver sulfide [93, 94]. As a result of these chemical reactions, they suffer a huge degradation in their optical properties. This increases optical loss and degrades the overall performance of the plasmonic devices.

(v) Incompatible manufacturing process

Metals like gold and silver are not compatible with standard silicon manufacturing processes. Thus, plasmonic devices cannot be manufactured using conventional nanofabrication technologies. This also prevents plasmonic devices to be incorporated in nanoelectronics integrated circuits. They can be diffused into silicon which will alter the optical properties and thus severely degrade the performance of the device [95, 96]. Thus, plasmonic metals like gold and silver are still outside the scope of being manufactured using standard silicon manufacturing technologies and yet to be incorporated in nanoelectronics integrated circuits.

CHAPTER 3

POTENTIAL ALTERNATIVE MATERIALS AND THEIR MATHEMATICAL MODELS

To overcome the drawbacks of conventional plasmonic metals like gold and silver, researchers are searching for better alternatives which can show similar behavior like metals in terms of SPP formation and propagation. To produce and propagate SPPs, the plasmonic property to look for is the negative real part of the complex dielectric permittivity. There are several techniques to make some alteration in the composition of a material to make it behave like metal i.e., to make the real part of dielectric permittivity negative. Some alternative materials suggested by the researchers are:

    i.   Heavily doped semiconductors like silicon[97, 98], germanium[99]etc.

    ii.   Heavily doped group III-IV semiconductors like GaAs, InP[100] etc.

    iii.   Transparent conducting oxides like zinc oxide, cadmium oxide[101, 102] etc.

    iv.   Other oxides and sulfides like $CdSb_2O_6$, $GaInO_3$, $MgIn_2O_4$[103]etc.

    v.   Silicides and Germanides[104].

    vi.   2D plasmonic material like graphene[105].

The primary objective of this thesis is to mathematically model and the plasmonic property analysis of the first group of the material mentioned above, that is the heavily doped semiconductors like silicon and germanium.

3.1 Heavily Doped Silicon

To fabricate optical components and integrated circuits, silicon photonics is one of the key technologies nowadays [106, 107]. It is already being implemented in the commercial-scale [108]. If heavily doped silicon can be used as an alternative to metal, silicon plasmonics has a great possibility in the near future [97, 109, 110]. Silicon can be doped with arsenic, antimony, phosphorus, etc., group V elements, to make it n-type. It can be doped with group III elements like boron, gallium, aluminum, etc. to make it p-type. Different optical properties of doped

silicon have been investigated by Balkanski et al. [111] and Schroder et al. [112]. The solubility of boron, phosphorus, and arsenic impurities in silicon has been investigated by Trumbore[113]. Use of n-type silicon would be a bit advantageous because of the smaller effective mass of electrons compared to holes [114] although both n-type and p-type silicon has the potential to replace metals in plasmonic devices.

3.2 Heavily doped p-Silicon

Since the plasmonic properties of natural metals like gold and silver are described by the dielectric permittivity of the material, the plasmonic properties of p-doped silicon can also be described by its frequency-dependent complex dielectric permittivity. The dielectric permittivity of heavily doped p-silicon has been experimentally investigated by Shahzad et al. [115] for carrier concentrations of $6\times10^{19}\,cm^{-3}$ and $1\times10^{20}\,cm^{-3}$. The real part and the imaginary part of the complex dielectric permittivity of p-silicon carrier concentrations are measured separately. Figure 3.1 shows the real part and imaginary part respectively found by Shahzad et al.[115] for carrier concentrations of $6\times10^{19}\,cm^{-3}$ and $1\times10^{20}\,cm^{-3}$.
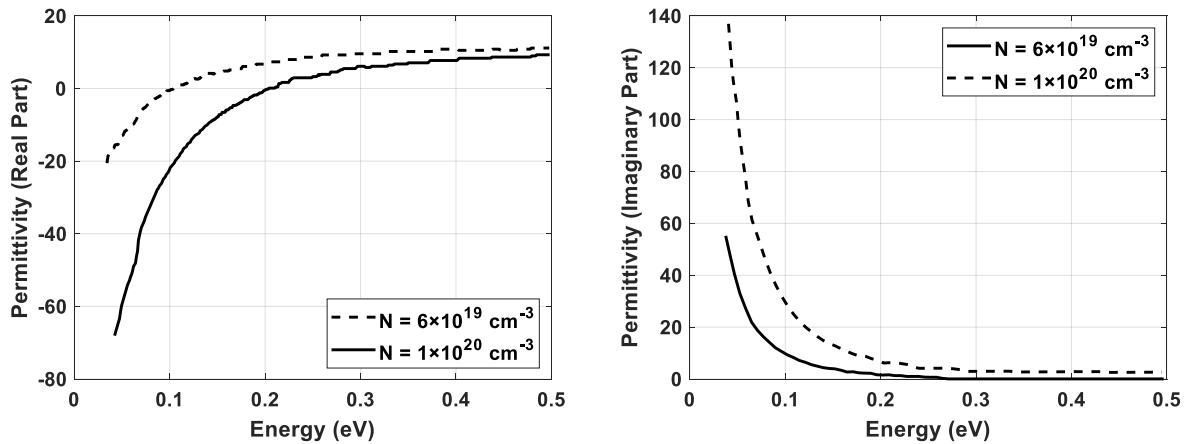
Figure 3.1: (a) Real part, (b) Imaginary part of the experimentally found dielectric permittivity.

3.2.1 Theoretical Model of p-Silicon

For the purpose of simulation and other calculations, p-silicon must be theoretically modeled to express its dielectric property by some mathematical equations. The frequency-dependent

complex dielectric permittivity of highly doped silicon can be described by the Lorentz-Drude model [34].

$$\varepsilon(\omega) = \varepsilon_\infty - \frac{\omega_p^2}{\omega^2\left(1 + i\dfrac{1}{\omega\tau}\right)} \quad \text{..(3.1)}$$

If the real part and imaginary parts are separated, (3.1) becomes,

$$\varepsilon(\omega) = \left(\varepsilon_\infty - \frac{\omega_p^2\tau^2}{1 + \omega^2\tau^2}\right) + i\frac{\omega_p^2\tau}{\omega(1 + \omega^2\tau^2)} \quad \text{........................(3.2)}$$

where, ω_p is the plasma frequency, ε_∞ is the infinite frequency relative permittivity or the background permittivity, τ is the electron/hole relaxation time, $\omega = \dfrac{2\pi c}{\lambda}$ is the angular frequency, c is the speed of light in vacuum, and i is the imaginary unit. In the case of the highly doped degenerate intrinsic semiconductors, $\omega_p^2 = \dfrac{Ne^2}{\varepsilon_0 m_{eff}}$ and $\tau = \dfrac{\mu m_{eff}}{e}$ where, N is the free carrier concentration, μ is the electron/hole's drift mobility and m_{eff} is the averaged electron/hole effective mass [116]. Usually, the angular frequency $\omega \gg \omega_p$ and $\omega\tau \gg 1$ [117]. Thus, (3.2) can be rewritten as,

$$\varepsilon(\omega) = \left(\varepsilon_\infty - \frac{\sigma}{\omega^2\varepsilon_0\tau}\right) + i\frac{\sigma}{\omega^3\tau^2\varepsilon_0} \quad \text{.....................................(3.3)}$$

where, $\sigma \approx eN\mu$ is the conductivity of the doped silicon and e is the charge of an electron and ε_0 is the free space permittivity. The infinite frequency relative permittivity or the background permittivity is the high-frequency limiting value that is approximately 11.7 for silicon and is independent of the doping concentration [60, 118]. Here, $\mu = 50$ [112] and $m_{eff} = 0.37 \times m_0$, where, m_0 is the mass of the electron [119].

3.2.2 Verification of the Mathematical Model

The theoretical model can be verified by comparing dielectric permittivity calculated using (3.3) with the experimentally obtained value by Shahzad et al. [115]. In order to compare the

theoretical and experimental values, the theoretical values must be calculated for carrier concentration of 6×10^{19} cm^{-3} and 1×10^{20} cm^{-3} since the experimental values are found at those carrier concentrations. The values of different parameters of (3.3) for p-silicon carrier concentration of 6×10^{19} cm^{-3} and 1×10^{20} cm^{-3} is shown in Table 3.1.

Table 3.1: Model parameters of heavily doped p-silicon by Lorentz-Drude model.

Parameters	Values	
	Carrier Concentration of 6×10^{19} cm^{-3}	Carrier Concentration of 1×10^{20} cm^{-3}
ε_0	11.7	11.7
e	1.60217662×10^{-19}	1.60217662×10^{-19}
μ	50	50
m_{eff}	$3.5526595884\times10^{-31}$	$3.5526595884\times10^{-31}$
τ	$1.2417416061807\times10^{-10}$	$1.2417416061807\times10^{-10}$
σ	$5.3833134432\times10^{08}$	8.972189072×10^{08}

Comparison between the dielectric permittivity calculated from (3.3) and the experimental value for carrier concentration of 6×10^{19} cm^{-3} and 1×10^{20} cm^{-3} has been shown in Figure 3.2.
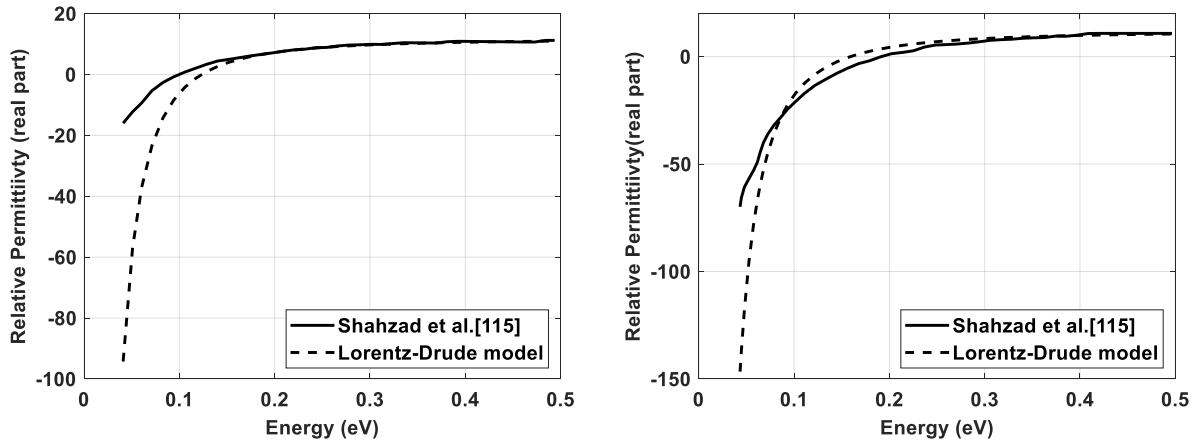
Figure 3.2: Comparison of the real parts of the permittivity between theoretical value and experimental value for carrier concentration of (a) 6×10^{19} cm^{-3} (b) 1×10^{20} cm^{-3}.

The percentages of error between the theoretically calculated value using Lorentz-Drude model and the experimentally obtained value by Shahzad et al. [115] at different wavelengths for p-

silicon carrier concentration of 6×10^{19} cm^{-3} and 1×10^{20} cm^{-3} has been shown in Table 3.2 and Table 3.3 respectively.

Table 3.2: Comparison of real parts of relative permittivity of p-Silicon between the theoretical value and the experimental value for a carrier concentration of 6×10^{19} cm^{-3}.

| Energy (eV) | Wavelength (µm) | Values of Relative Permittivity (Real Part) | | Percentage of Error (%) |
		Experimental (Shahzad et al. [115])	Theoretical (Lorentz-Drude Model)	
0.14	8.1	4.43	2.64	40
0.15	7.49	4.95	3.97	19.88
0.16	6.96	5.53	5.02	9.27
0.17	6.5	6.12	5.87	3.95
0.28	4.08	9.67	9.4	2.84
0.35	3.27	10.41	10.22	1.83
0.42	2.73	10.82	10.67	1.45
0.45	2.52	10.71	10.82	1.02

Table 3.3: Comparison of real parts of relative permittivity of p-Silicon between the theoretical value and the experimental value for a carrier concentration of 1×10^{20} cm^{-3}.

Energy (eV)	Wavelength (μm)	Values of Relative Permittivity (Real Part)		Percentage of Error (%)
		Experimental (Shahzad et al. [115])	Theoretical (Lorentz-Drude Model)	
0.064	17.69	-44.85	-60.24	34.33
0.067	16.72	-39.97	-52.62	31.66
0.11	10.23	-17.14	-12.40	27.60
0.29	3.86	6.88	8.29	20.35
0.30	3.71	7.56	8.53	12.86
0.34	3.34	8.53	9.14	7.12
0.43	2.63	10.81	10.11	6.43
0.46	2.49	10.81	10.27	4.98
0.5	2.28	10.81	10.5	2.85

From Figure 3.3 and Table 3.2, it is observed that for a carrier concentration of 6×10^{19} cm^{-3}, the percentage of error between the real part of the theoretical value and the experimental value is very high (>160%) for wavelengths greater than 9.69 μm, high (40%) for wavelengths between 6.5 μm to 9.69 μm and very low ($\leq$ 3.95%) for wavelengths less than 6.5 μm. For a carrier concentration of 1×10^{20} cm^{-3}, the percentage of error is very high (>109.7%) for wavelengths greater than 26.23 μm, high (20.35% - 34.33%) for wavelengths between 3.86μm to 17.69 μm and low ($\leq$ 7.12%) for wavelengths smaller than 3.34 μm. Analyzing the data from Table 3.2 and Table 3.3, it is evident that the model shows a low percentage of error for wavelengths smaller

than 3.34 µm. Thus, this model of heavily doped p-silicon can be used for the plasmonic devices which work in the range of wavelengths smaller than 3.34 µm, which is the case for most of the plasmonic applications.

Heavily doped p-silicon can also be modeled at other carrier concentrations and wavelengths. The relationship of both the real part and imaginary part of the permittivity with carrier concentration and wavelength is almost linear. Figure 3.3 shows the plot of relative permittivity against carrier concentration for different wavelengths and Figure 3.4 shows the plot of relative permittivity against wavelength for different carrier concentration.

(a)   (b)
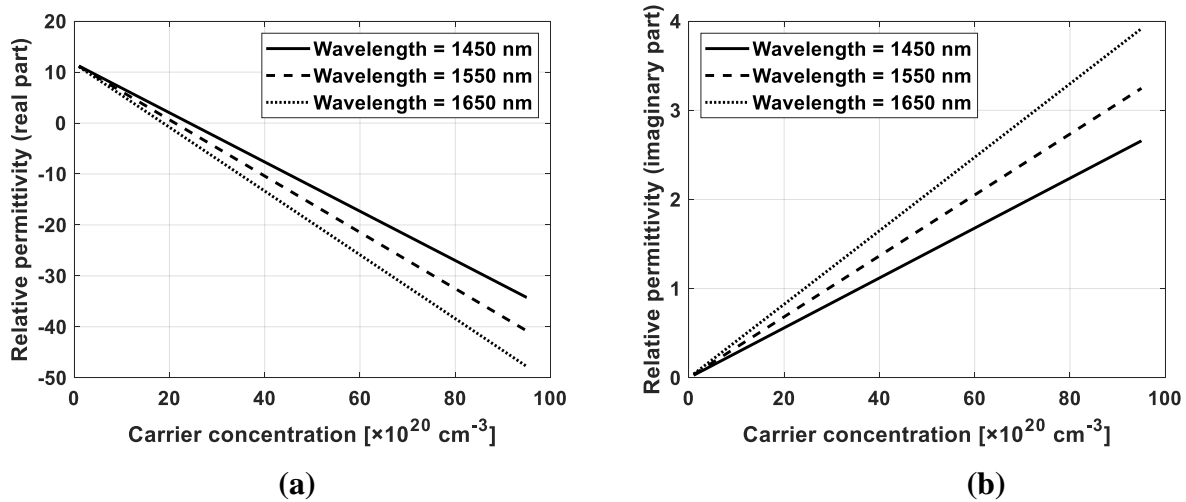
Figure 3.3: Relative permittivity (a) real part, (b) imaginary part versus carrier concentration at different wavelength**s.**

(a)   (b)
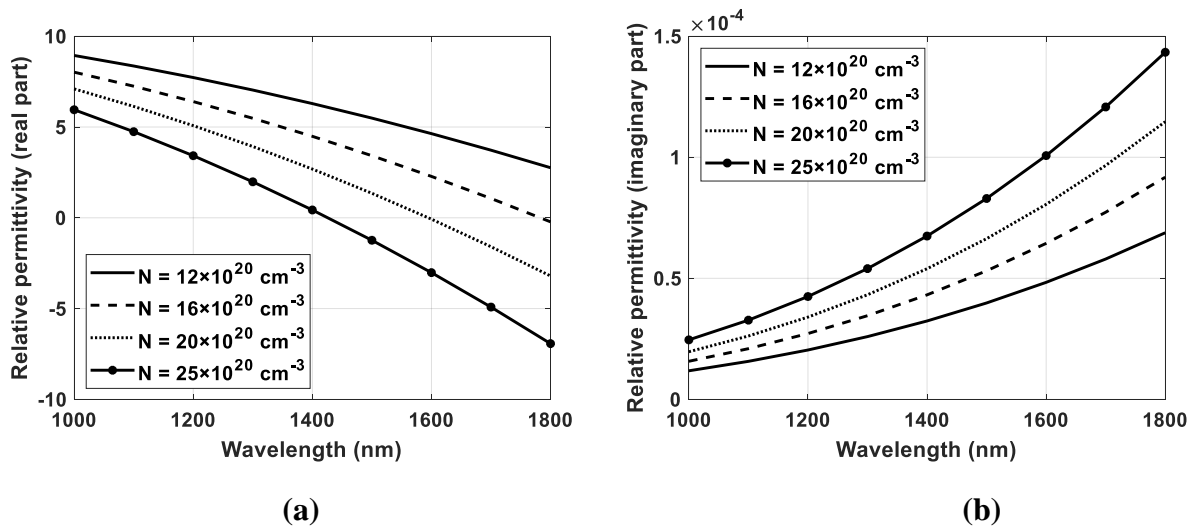
Figure 3.4: Relative permittivity (a) real part, (b) imaginary part versus wavelength at different carrier concentration.

3.2.3 Comparison with Conventional Plasmonic Metals

The complex dielectric permittivity of p-silicon can be compared with the dielectric permittivity of commonly used metals like gold and silver in order to have some idea about the performance of p-silicon in plasmonic devices. Since the relative permittivity is a complex quantity, it will have both real and imaginary part. Figure 3.5 shows the real part of both gold and silver plotted along with the real part of the permittivity of p-silicon for different carrier concentration. The comparison between the imaginary parts is shown in Figure 3.6.
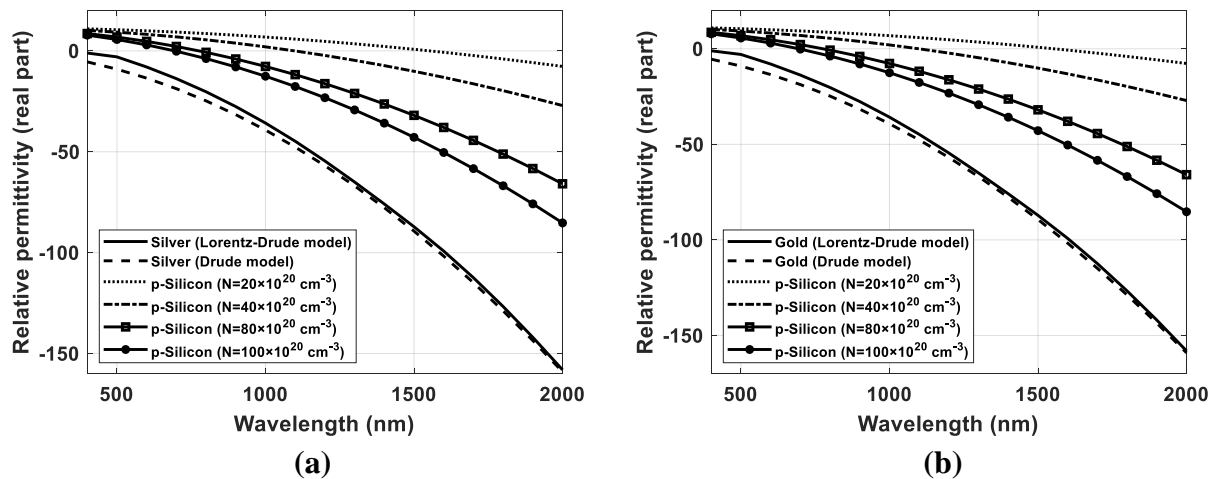
Figure 3.5: The real part of relative permittivity for (a) silver and p-silicon, (b) gold and p-silicon for different value of carrier concentration of p-silicon.
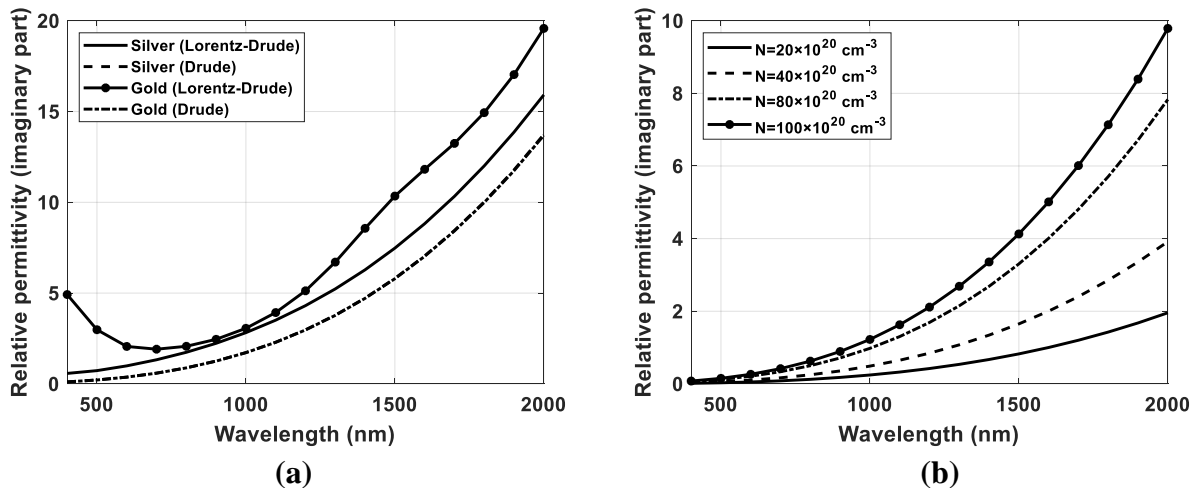
Figure 3.6: Imaginary part of relative permittivity for (a) silver and gold, (b) p-silicon for different value of carrier concentration.

25

From Figure 3.5, it is observed that silver, gold, and p-silicon; all of them have a negative real part of the permittivity after a certain wavelength. The real part of the complex permittivity for both gold and silver is larger than the p-silicon. This is mainly due to their high carrier concentration ($\approx 10^{23}$ cm^{-3}). The large real part of the permittivity causes polarization mismatch when the interface is created with an insulator in plasmonic devices. Thus, it is desirable to have a smaller value of real permittivity for having a balanced polarization response. Since p-silicon has a comparatively smaller real part, it will be advantageous in forming plasmonic devices compared to both gold and silver. Comparison between the imaginary parts of the dielectric permittivity is shown in Figure 3.6. The imaginary parts of the permittivity of both gold and silver are much larger than that of p-silicon even at a higher carrier concentration of p-silicon. Since the large value of the imaginary part is responsible for larger optical loss, plasmonic devices formed with p-silicon will suffer much lower optical loss than the conventional metal plasmonic devices.

3.3   Heavily doped n-Silicon

Like p-silicon, heavily doped n-silicon can also show negative real permittivity after doping more than a certain carrier concentration. An improved dielectric function has been demonstrated by Basu et al. [120]. The model has been proposed after considering the effect of temperature, impurity scattering, lattice scattering, and temperature-dependent carrier mobility. Basu et al.[120] have predicted the dielectric function of n-type silicon for doping concentrations of 10^{18} cm^{-3}, 10^{19} cm^{-3}, 10^{20} cm^{-3}, 10^{21} cm^{-3} at 400 K. The real parts and imaginary parts of the dielectric permittivity of n-doped silicon at different carrier concentration proposed by Basu et al. [120] are shown in Figure 3.7.
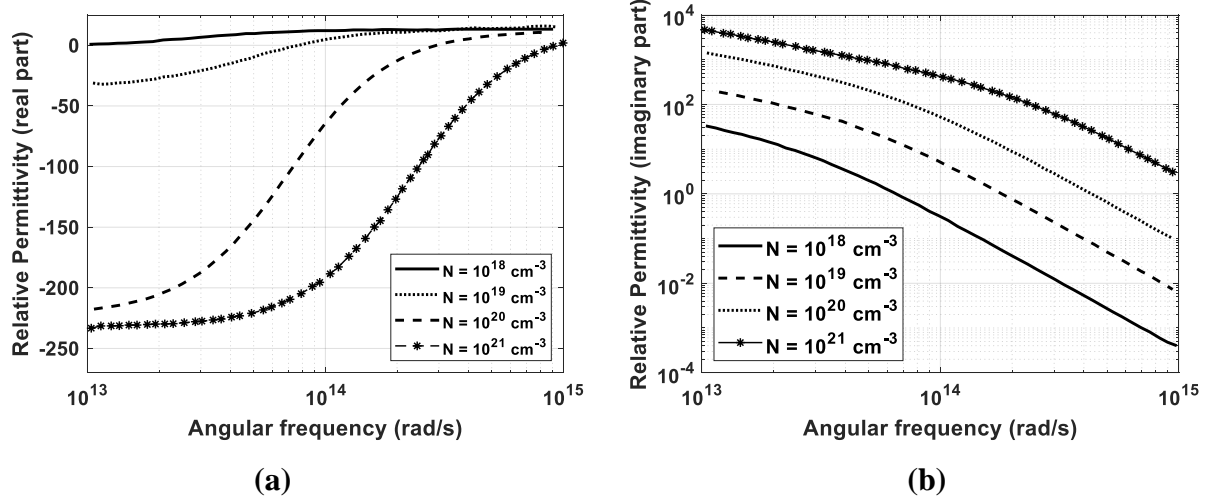
Figure 3.7: (a) Real part, (b) imaginary part of the dielectric function of n-doped silicon at 400K for different carrier concentrations proposed by Basu et al [120].

3.3.1 Model of n-Silicon

Like p-silicon, the frequency-dependent dielectric permittivity of heavily doped n-silicon can also be described by the Lorentz-Drude model given in (3.1) and (3.3). For n-doped silicon, $\mu = 100$ [112] and $m_{eff} = 0.26 \times m_0$, where, m_0 is the mass of the electron [119, 121].

The values of different parameters of (3.3) for heavily doped n-silicon at carrier concentration of 10^{18} cm^{-3}, 10^{19} cm^{-3}, 10^{20} cm^{-3}, 10^{21} cm^{-3} is given in Table 3.4.

Table 3.4: Model parameters of heavily doped n-silicon by Lorentz-Drude model

Paramet ers	Values			
	Carrier Concentration of 10^{18} cm^{-3}	Carrier Concentration of 10^{19} cm^{-3}	Carrier Concentration of 10^{20} cm^{-3}	Carrier Concentration of 10^{21} cm^{-3}
ε_0	11.7	11.7	11.7	11.7
e	$1.60217662 \times 10^{-19}$	$1.60217662 \times 10^{-19}$	$1.60217662 \times 10^{-19}$	$1.60217662 \times 10^{-19}$
μ	100	100	100	100
m_{eff}	$2.3684397 \times 10^{-31}$	$2.3684397 \times 10^{-31}$	$2.3684397 \times 10^{-31}$	$2.3684397 \times 10^{-31}$
τ	$8.27827737 \times 10^{11}$	$8.27827737 \times 10^{11}$	$8.27827737 \times 10^{11}$	$8.27827737 \times 10^{11}$
σ	$8.97218907 \times 10^{06}$	$8.97218907 \times 10^{07}$	$8.97218907 \times 10^{08}$	$8.97218907 \times 10^{09}$

Comparison between the real parts of the dielectric permittivity calculated from (3.3) and the values predicted by Basu et al. [120] for carrier concentration of 10^{18} cm^{-3}, 10^{19} cm^{-3}, 10^{20} cm^{-3}, 10^{21} cm^{-3}has been shown in Figure 3.8.
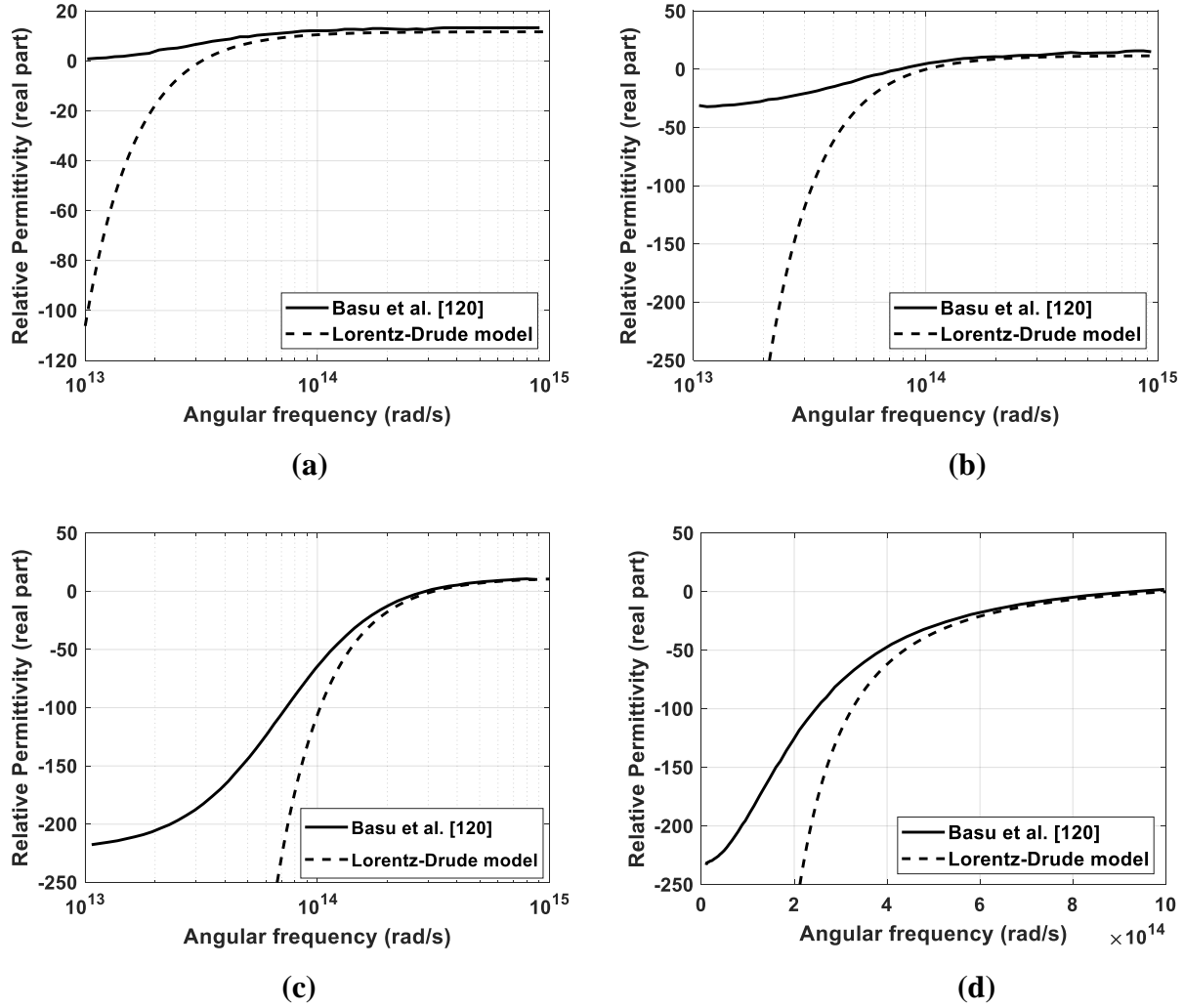
Figure 3.8: Comparison of the real parts of the permittivity between the values calculated using (3.3) and the values proposed by Basu et al. [120] for carrier concentrations of (a) 10^{18} cm^{-3}, (b) 10^{19} cm^{-3}, (c) 10^{20} cm^{-3}, (d) 10^{21} cm^{-3}.

The percentages of error between the theoretically calculated value of dielectric permittivity of n-silicon using Lorentz-Drude model and the values predicted by Basu et al. [120] at different wavelengths for n-silicon carrier concentration of 10^{18} cm^{-3}, 10^{19} cm^{-3}, 10^{20} cm^{-3} and 10^{21} cm^{-3} has been shown in Table 3.5, Table 3.6, Table 3.7 and Table 3.8 respectively.

Table 3.5: Comparison of real parts of relative permittivity of n-Silicon between the values calculated using Lorentz-Drude model and values predicted by Basu et al. [120] for carrier concentration of 10^{18} cm^{-3}.

Angular Frequency, ω ($\times 10^{13}$rad/s)	Wavelength (μm)	Values of Relative Permittivity (Real Part)		Percentage of Error (%)
		Basu et al. [120]	Lorentz-Drude Model	
3.53	53.39	6.69	2.22	66.71
4.64	40.61	8.49	6.21	26.81
5.05	37.28	8.49	7.08	16.67
5.98	31.51	9.40	8.40	10.65
7.14	26.36	10.00	9.39	6.14
1.01	18.59	10.90	10.55	3.27
2.05	91.75	11.66	11.42	2.07
3.23	58.37	11.87	11.58	2.40
4.19	44.96	12.11	11.63	3.97
5.42	34.73	12.11	11.65	3.74
7.1	26.52	12.11	11.67	3.60
9.05	2.081	12.11	11.68	3.53

Table 3.6: Comparison of real parts of relative permittivity of n-Silicon between the values calculated using Lorentz-Drude model and values predicted by Basu et al. [120] for carrier concentration of 10^{19} cm^{-3}.

Angular Frequency, ω ($\times10^{13}$rad/s)	Wavelength (μm)	Values of Relative Permittivity (Real Part)		Percentage of Error (%)
		Basu et al. [120]	Lorentz-Drude Model	
7.68	24.49	-4.81	-8.24	71.07
11.28	16.68	1.62	2.45	50.94
15.89	11.85	4.94	7.03	42.34
27.70	6.79	7.31	10.16	38.92
32.88	5.72	7.87	10.60	34.80
35.76	5.26	8.49	10.77	26.83
47.63	3.95	8.98	11.18	24.42
56.53	3.33	9.43	11.33	20.04
67.08	2.80	9.69	11.43	18.02
73.06	2.57	10.82	11.47	6.07
79.47	2.37	11.14	11.51	3.27
86.58	2.17	11.17	11.54	3.29

Table 3.7: Comparison of real parts of relative permittivity of n-Silicon between the values calculated using Lorentz-Drude model and values predicted by Basu et al. [120] for carrier concentration of 10^{20} cm^{-3}.

Angular Frequency, ω ($\times 10^{13}$rad/s)	Wavelength (μm)	Values of Relative Permittivity (Real Part)		Percentage of Error (%)
		Basu et al. [120]	Lorentz-Drude Model	
9.23	20.39	-73.11	-126.46	72.98
10.55	17.84	-59.08	-94.14	59.33
12.23	15.40	-45.18	-67.10	48.50
20.32	9.26	-12.01	-16.82	40.03
36.91	5.10	4.42	3.04	31.09
43.79	4.30	6.70	5.55	17.15
47.69	3.94	7.49	6.51	13.02
51.95	3.62	8.28	7.33	11.51
73.14	2.57	10.36	9.49	8.39
79.67	2.36	10.66	10.14	4.88
86.80	2.16	10.96	10.83	1.22

Table 3.8: Comparison of real parts of relative permittivity of n-Silicon between the values calculated using Lorentz-Drude model and values predicted by Basu et al. [120] for carrier concentration of 10^{21} cm^{-3}.

Angular Frequency, ω ($\times 10^{13}$rad/s)	Wavelength (μm)	Values of Relative Permittivity (Real Part)		Percentage of Error (%)
		Basu et al. [120]	Lorentz-Drude Model	
25.83	7.29	-96.42	-164.94	71.05
28.74	6.55	-83.36	-130.97	57.12
32.88	5.73	-68.81	-97.35	41.48
37.6	5.01	-55.02	-71.67	30.26
44.2	4.26	-40.46	-48.64	20.19
-30.8	3.58	-27.7	-30.8	11.17
58.09	3.24	-21.44	-23.23	8.34
63.24	2.98	-16.99	-17.78	4.64
68.84	2.74	-12.72	-13.17	3.6
83.09	2.27	-5.3	-5.37	1.44
90.55	2.08	`-2.68	-2.71	1.27

From Table 3.5, it is observed that, for a carrier concentration of 10^{18} cm^{-3}, the error between the two models is comparatively higher (>10%) for wavelengths greater than 31.51 μm, smaller (<10%) for wavelengths smaller than 31.51 μm and very small (<5%) for wavelengths smaller than 18.59 μm. For carrier concentration of 10^{19} cm^{-3}, Table 3.6 shows that the error percentage is high (>25%) for wavelengths greater than 5.26 μm, moderate (5% to 25%) for wavelengths

greater than 2.57 μm and very small (<5%) for wavelengths smaller than 2.37 μm. Table 3.7 shows higher (>25%) percentage of error for wavelengths greater than 5.10 μm, moderate (5% to 25%) error for wavelengths greater than 2.57 μm and very low (<5%) for wavelengths smaller than 2.36 μm for carrier concentration of 10^{20} cm^{-3}. From Table 3.8, the error percentage is found high (>25%) for wavelengths greater than 5.01 μm, moderate (5% to 25%) for wavelengths greater than 3.24 μm and very low (<5%) for wavelengths smaller than 2.98 μm for carrier concentration of 10^{21} cm^{-3}. The range of wavelengths for different percentage of errors is shown in Table 3.9.

Table 3.9: Wavelength ranges for different error percentage between the Lorentz-Drude model and model proposed by Basu et al. [120].

Carrier Concentration (cm^{-3})	Wavelength Range (μm)			Smallest wavelength for low error (μm)
	For high error (>25%)	For moderate error (5% to 25%)	For very low error (<5%)	
10^{18}	> 40.61	26.36 – 37.25	< 18.59	
10^{19}	> 5.26	2.57 – 3.95	< 2.37	< 2.36
10^{20}	> 5.10	2.57 – 4.30	< 2.36	
10^{21}	> 5.01	3.24 – 4.26	< 2.95	

As observed in Table 3.9, for all carrier concentrations of n-silicon, the error percentage is very low (<5%) for wavelengths smaller than 2.36 μm. The error percentage becomes smaller as the wavelength becomes shorter. Thus, for wavelengths smaller than 2 μm, the error percentage between the two models will be very negligible. Since most of the plasmonic applications are in the range of wavelengths smaller than 2 μm, the Lorentz-Drude model can be considered as a verified model as it matches with another already established model of n-silicon.

The frequency-dependent complex dielectric permittivity can be modeled at other frequencies and for other doping concentrations of n-silicon using the Lorentz-Drude model given by (3.3). Like p-silicon, the relationship of both the real part and imaginary part of the permittivity with

carrier concentration and wavelength is almost linear. The variation of dielectric permittivity with the change of doping concentration of n-silicon at different wavelengths is shown in Figure 3.9. The relationship with wavelength for different doping concentration of n-silicon is shown in Figure 3.10.
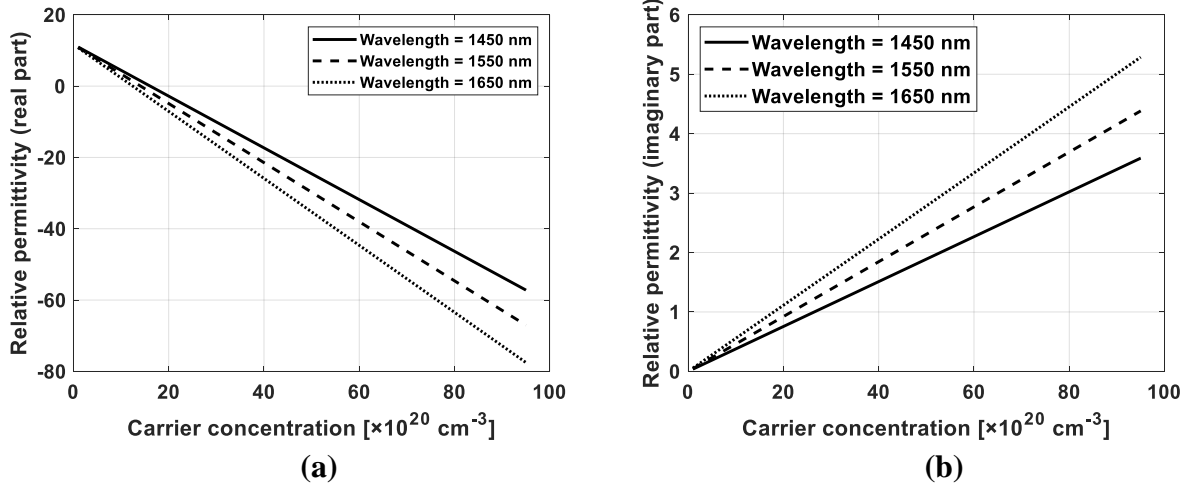
Figure 3.9: Relative permittivity (a) real part, (b) imaginary part versus carrier concentration at different wavelength**s.**
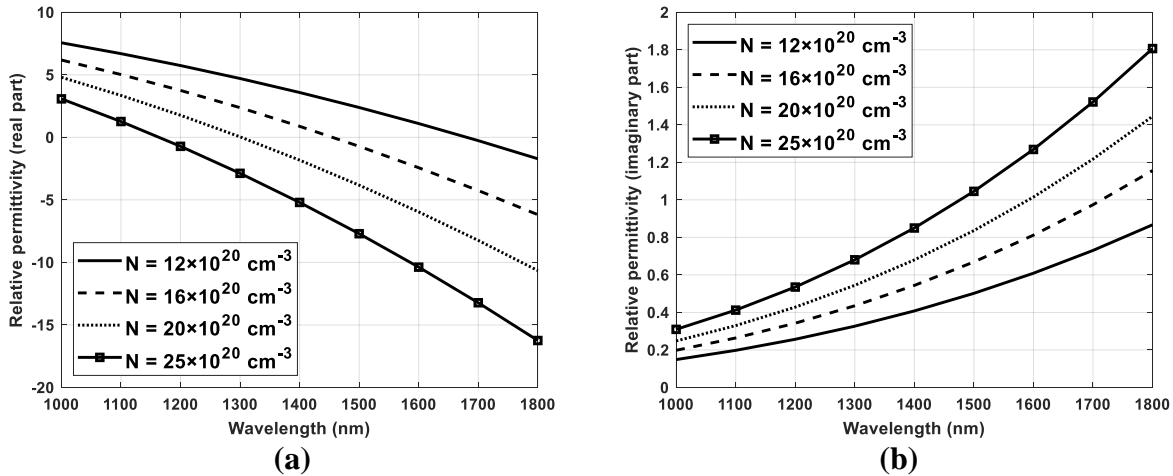
Figure 3.10: Relative permittivity (a) real part, (b) imaginary part versus wavelength at different carrier concentration.

3.3.2 Comparison with Conventional Plasmonic Metals

Like p-silicon, the complex dielectric permittivity of n-silicon can be compared with the dielectric permittivity of commonly used metals like gold and silver in order to have some idea about the performance of n-silicon in plasmonic devices. Since the relative permittivity is a

complex quantity, it will have both real and imaginary part. Figure 3.11 shows the real part of both gold and silver plotted along with the real part of the permittivity of n-silicon for different carrier concentration. The comparison between the imaginary parts is shown in Figure 3.12.
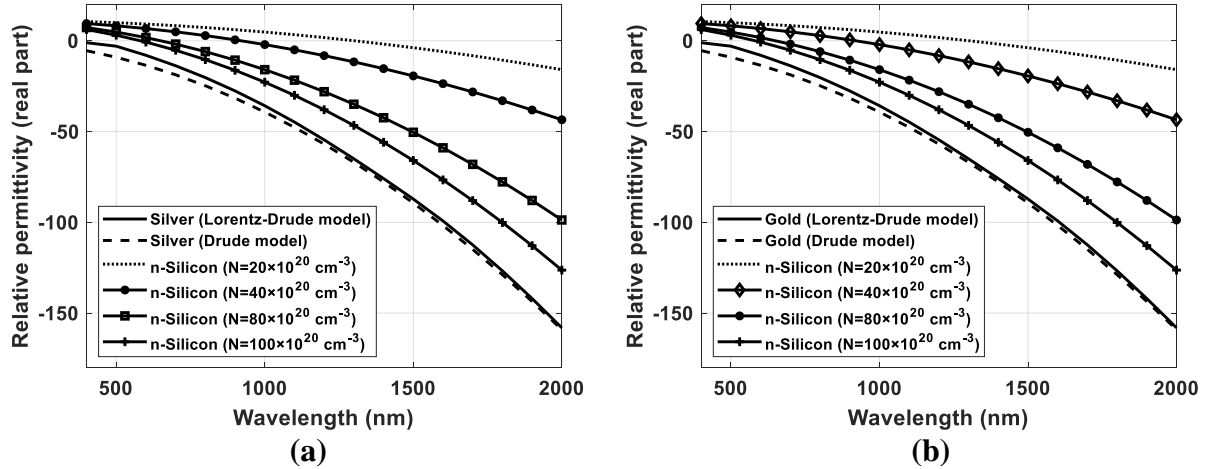
Figure 3.11. The real part of relative permittivity for (a) silver and n-silicon, (b) gold and n-silicon for different value of carrier concentration of n-silicon.
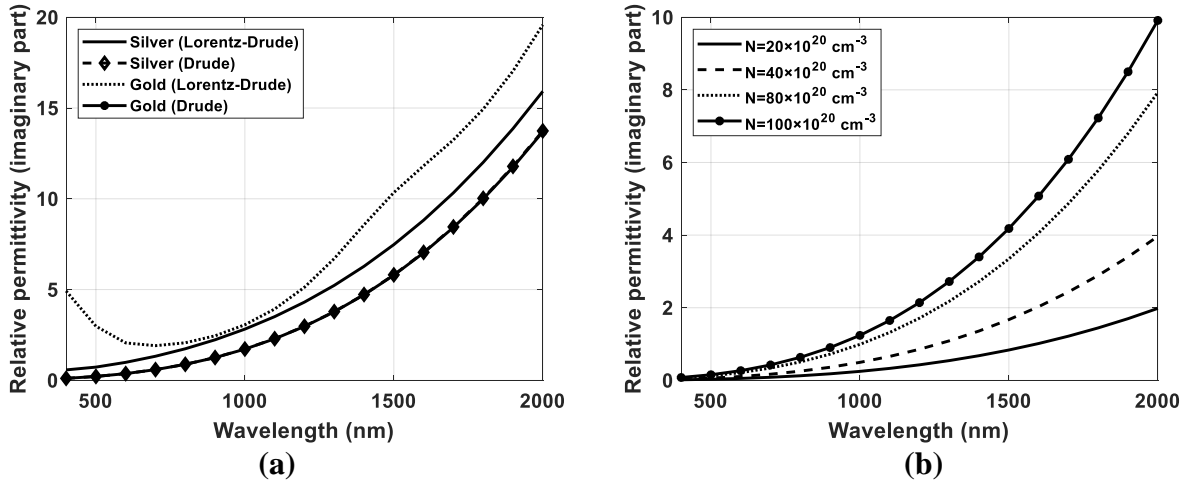
Figure 3.12: Imaginary part of relative permittivity for (a) silver and gold, (b) n-silicon for different value of carrier concentration.

From Figure 3.11, it is observed that silver, gold, and n-silicon, all of them have a negative real part of the permittivity after a certain wavelength. The real part of the complex permittivity for both gold and silver is larger than the n-silicon. This is mainly due to their high carrier concentration ($\approx 10^{23}$ cm^{-3}). The large real part of the permittivity causes polarization mismatch when the interface is created with an insulator in plasmonic devices. Thus, it is desirable to have a smaller value of real permittivity for having a balanced polarization response. Since n-silicon

has a comparatively smaller real part, it will be advantageous in forming plasmonic devices compared to both gold and silver. Comparison between the imaginary parts of the dielectric permittivity is shown in Figure 3.12. The imaginary parts of the permittivity of both gold and silver are much larger than that of n-silicon even at a higher carrier concentration of n-silicon. Since the large value of the imaginary part is responsible for larger optical loss, plasmonic devices formed with n-silicon will suffer much lower optical loss than the conventional metal plasmonic devices.

CHAPTER 4

WAVEGUIDE DESIGN AND RESULT ANALYSIS

Plasmonic waveguides play an essential role in guiding SPPs in plasmonic devices. An improved transmission characteristic of a plasmonic waveguide can enhance the performance of the plasmonic devices. The conventional plasmonic waveguides are mainly formed with two types of structures, namely, metal-insulator-metal (MIM) and insulator-metal-insulator (IMI). Between these two type of structures, MIM structures have gain more popularity due to their ability of light confinement. Present plasmonic waveguides use gold or silver as the metal and air as the insulator. Here, the plasmonic waveguide will be designed with doped silicon instead of metal and air as the insulator and will be investigated numerically. The simulations are done with commercial simulation software COMSOL Multiphysics which employs Finite Element Method (FEM) for simulation purpose.

4.1 FEM for Electromagnetic Field

The fundamental equations for electromagnetic field calculations are the Maxwell equations[122]:

$$\nabla \cdot D = \rho_{ch} \text{...(4.1)}$$

$$\nabla \cdot B = 0 \text{...(4.2)}$$

$$\nabla \times E = \frac{\partial B}{\partial t} \text{...(4.3)}$$

$$\nabla \times H = J + \frac{\partial D}{\partial t} \text{...(4.4)}$$

where, E is the electric field strength vector, D is the electric flux density vector, B is the magnetic flux density vector, H is the magnetic field strength vector, J is the current density vector and, ρ_{ch} is the charge density.

4.1.1 Potential Formulation and Electric Field Calculation:

The magnetic potential vector A and the electrical voltage V, defined by[123]:

$$B = \nabla \times A \dots\dots\dots\dots\dots\dots\dots\dots\dots\dots\dots\dots\dots\dots\dots(4.8)$$

$$E = -\nabla \times V \dots\dots\dots\dots\dots\dots\dots\dots\dots\dots\dots\dots\dots\dots(4.9)$$

From (4.3) and (4.8), Faraday-Lenz'slaw of electric field can be transformed into:

$$\nabla \times E = -\nabla \times \left(\frac{\partial A}{dt} \right) \dots\dots\dots\dots\dots\dots\dots\dots\dots\dots\dots(4.10)$$

When the electric field potential for the non-static fields is extended with an induced voltage, (4.10) becomes:

$$E = -\nabla V - \left(\frac{\partial A}{\partial t} \right) \dots\dots\dots\dots\dots\dots\dots\dots\dots\dots\dots(4.11)$$

When conductors are involved, the source term representing the charge density vanishes and it is replaced Dirichlet type boundary conditions. The potential equation reduces to a Laplace equation[124].

$$\nabla \cdot (\varepsilon \nabla V) = 0 \dots\dots\dots\dots\dots\dots\dots\dots\dots\dots\dots\dots(4.12)$$

Usually, ε is represented by a diagonal tensor, as the off-diagonal coupling terms are most of the time negligible:

$$\varepsilon = \begin{bmatrix} \varepsilon_x & 0 & 0 \\ 0 & \varepsilon_y & 0 \\ 0 & 0 & \varepsilon_z \end{bmatrix} \dots\dots\dots\dots\dots\dots\dots\dots\dots\dots\dots(4.13)$$

The energy associated with the electric field is expressed by:

$$W_E = \int_V \frac{D \cdot E}{2} dV = \int_V \frac{\varepsilon |E|^2}{2} dV \dots\dots\dots\dots\dots\dots(4.14)$$

S-parameters can be calculated using the equation:

$$S_{ij} = \frac{\displaystyle\int_{port\ i} (E_j \cdot E_i^*) dA_i}{\displaystyle\int_{port\ i} (E_j \cdot E_j^*) dA_i} \dots\dots\dots\dots\dots\dots\dots\dots(4.15)$$

The time average power transmittance, T can be obtained using the equation:

$$T = |S_{ij}|^2 \dots\dots\dots\dots\dots\dots\dots\dots\dots\dots\dots\dots\dots(4.16)$$

4.2 Simulation Result Validation

For the validation of simulation result by COMSOL Multiphysics, two plasmonic refractive index sensors proposed by Wu et al. [35] and Zou et al. [125] have been resimulated and the results are compared. The basic structures of the sensors have been shown in Figure 4.1. Figure 4.2 shows the comparison of the simulation result obtained by COMSOL Multiphysics with the results obtained by Wu et al. [35] and Zou et al. [125].

(a)   **(b)**
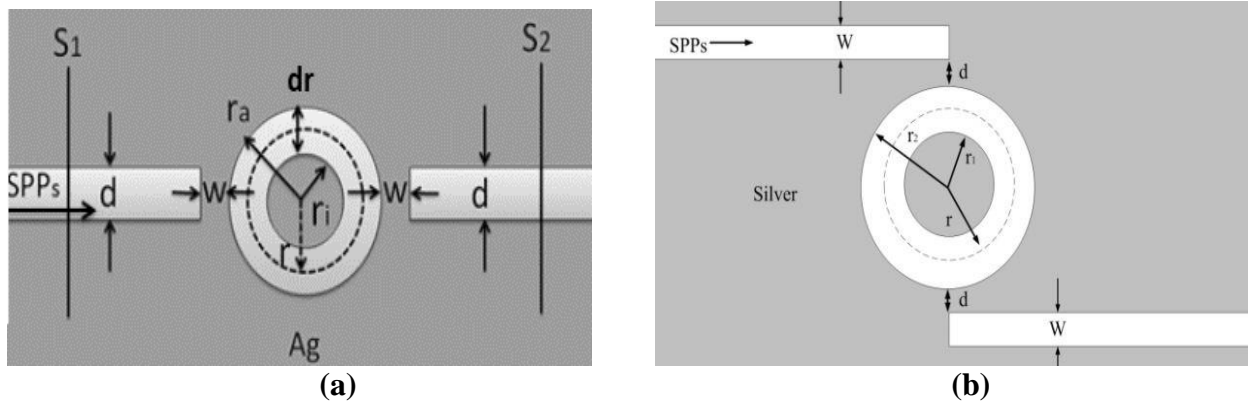
Figure 4.1: Basic structure of the sensor proposed by (a) Wu et al. [35] (b) Zou et al.[125].

(a)   **(b)**
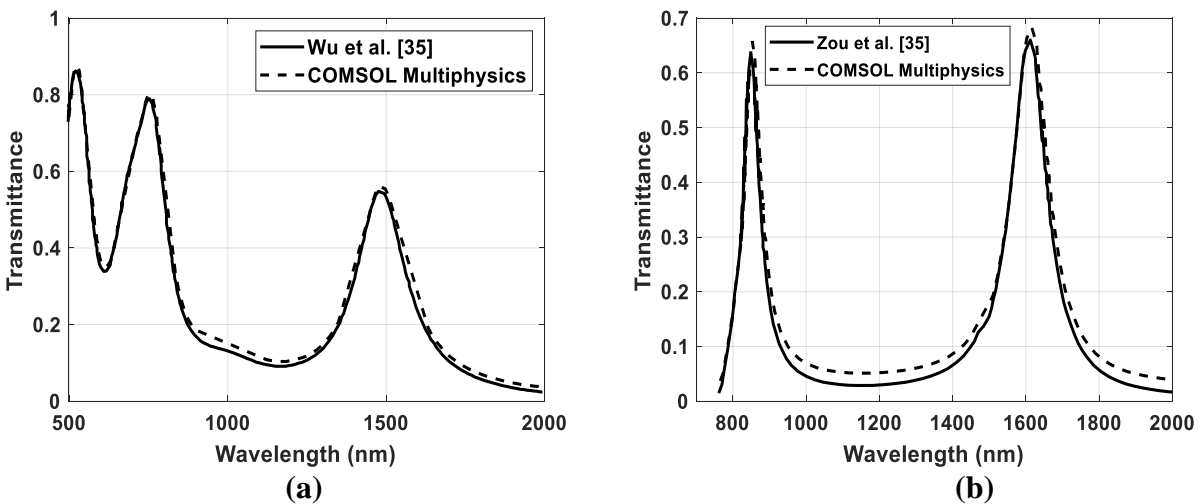
Figure 4.2: Comparison of the transmission characteristics obtained by COMSOL simulation with (a) Wu et al. [35], (b) Zou et al. [125].

Table 4.1: Comparison between the simulation result COMSOL and Wu et al. [35]

	Peak I (nm)	Peak II (nm)	Peak III (nm)
COMSOL	528.5	762.5	1491
Wu et al. [35]	526	760	1488
Percentage of Error	0.475%	0.329%	0.202%

Table 4.2: Comparison between the simulation result COMSOL and Zou et al. [125]

	Peak I (nm)	Peak II (nm)
COMSOL	854	1615
Zou et al. [125]	850	1609
Percentage of Error	0.47%	0.37%

The percentage of error between COMSOL simulation results and the results obtained by Wu et al. [35] and Zou et al. [125] have been shown in Table 4.1 and Table 4.2 respectively. In both cases the percentage of errors are very low (< 1%). Thus, the simulation results are verified.

4.3   Waveguide Design

The performance of the plasmonic waveguides can be analyzed from the transmission characteristics. The transmittance of a plasmonic waveguide mainly depends on the plasmonic properties of the material used to form the plasmonic waveguide. The real part and imaginary part of the complex dielectric permittivity is mainly responsible for higher or lower transmittance of the plasmonic waveguide formed. The negative real part of the permittivity is responsible for SPP formation and propagation. Thus, a large negative real part will create more SPPs and increase the transmittance of the waveguide. The imaginary part of the permittivity accounts for the optical loss. The small imaginary part will reduce optical loss and thus increase the transmittance. Both the real part and imaginary part of the permittivity of doped semiconductors will depend on the doping concentration. With the increase in doping concentration, the real part will increase, which will increase the transmittance and also the imaginary part will increase, which will decrease the transmittance. In the case of a doped semiconductor, the imaginary part

of the permittivity is smaller compared to the imaginary parts of silver or gold. Thus an increase in doping concentration will have a lower effect on the optical loss of the waveguide. Thus, higher doping concentration will increase the transmittance of the waveguide. However, achieving higher doping concentration in semiconductors is a challenge. Thus, the doping concentration of the semiconductors used to form the waveguide must be kept as low as possible depending on the applications where higher transmittance is not a requirement e.g., plasmonic sensors, plasmonic modulators.

4.4   p-Silicon waveguide

A straight waveguide is formed with p-silicon instead of metal and air as the insulator. The waveguide structure is shown in Figure 4.3. The width of the air waveguide, w is chosen to be 50 nm initially as most of the plasmonic waveguides or devices use w = 50 nm. Then it is varied to observe the change in the transmission characteristics. The length, L and the breadth, b is also varied, and the transmission characteristics are analyzed.
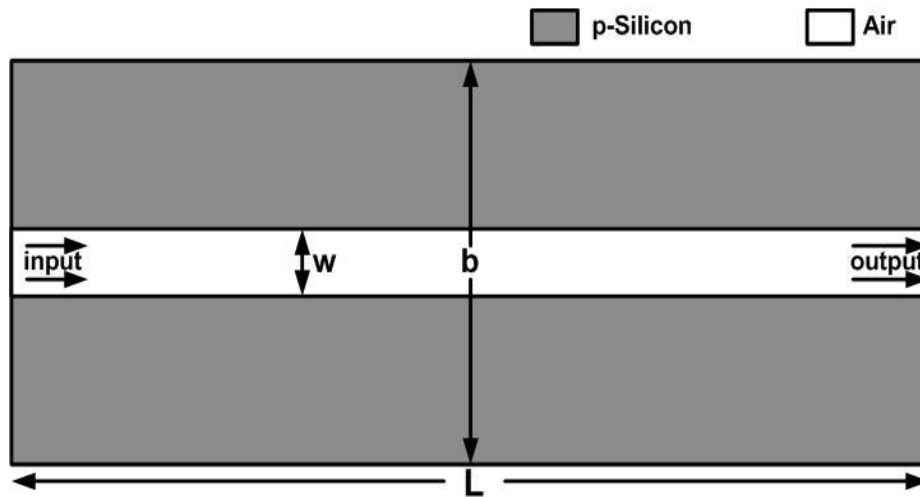
Figure 4.3: Schematic diagram of the waveguide formed with p-silicon and air.

The transmittance of the waveguide for different doping concentration (N) of p-silicon is shown in Figure 4.4. It is observed from Figure 4.4 that, the transmittance of the waveguide increases with the increase in carrier concentration. This is because the real party becomes more and more negative with the increase in carrier concentration which causes more SPPs to be generated and

propagated. The other parameters of the waveguide, the length, L and the breadth, b and the width of the air waveguide, w is also varied, and the transmission characteristics are analyzed.
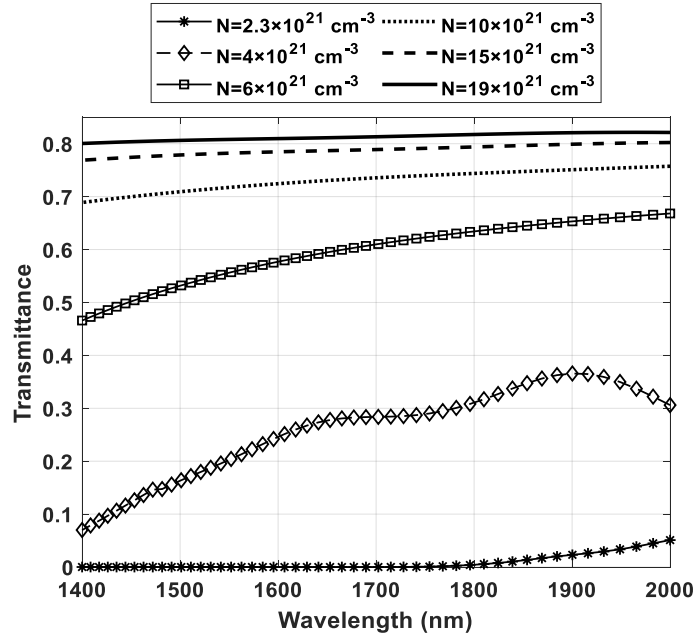
Figure 4.4: Transmission characteristics of the waveguide with w = 50 nm, b = 500 nm and L = 2 µm for different carrier concentrations of p-silicon.
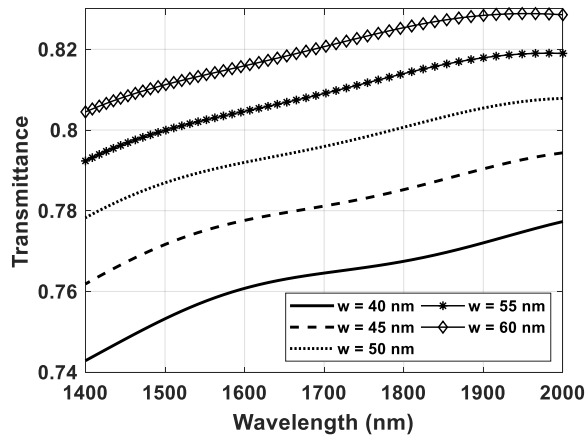
Figure 4.5: Transmission characteristics of the waveguide with N = 16×10^{21} cm^{-3}, L = 2 µm and b = 500 nm for different values of w.
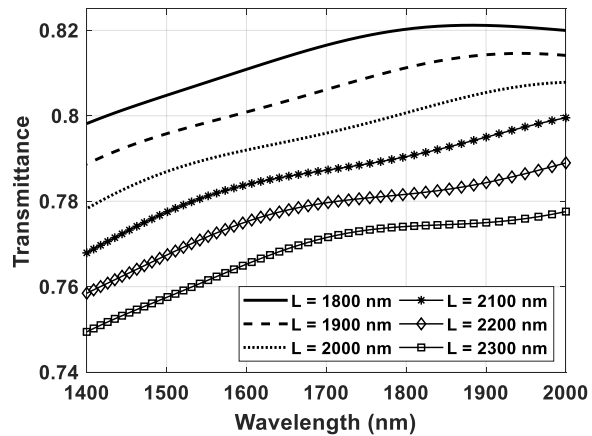
Figure 4.6: Transmission characteristics of the waveguide with N = 16×10^{21} cm^{-3}, w = 50 nm and b = 500 nm for different values of L.

The transmittance increases with an increase of w, decreases with the increase of L and b does not affect the transmission characteristics. These relationships of transmittance with different parameters are similar to the conventional plasmonic waveguides with gold or silver. The

transmission characteristics with the variation of w and L are shown in Figure 4.5, and Figure 4.6 respectively.

4.4.1 Comparison with Silver-Air-Silver Waveguide

The transmission characteristic of the p-silicon waveguide with w = 50 nm, b = 500 nm and L = 2 μm and silver-air-silver waveguide are shown in Figure 4.7.
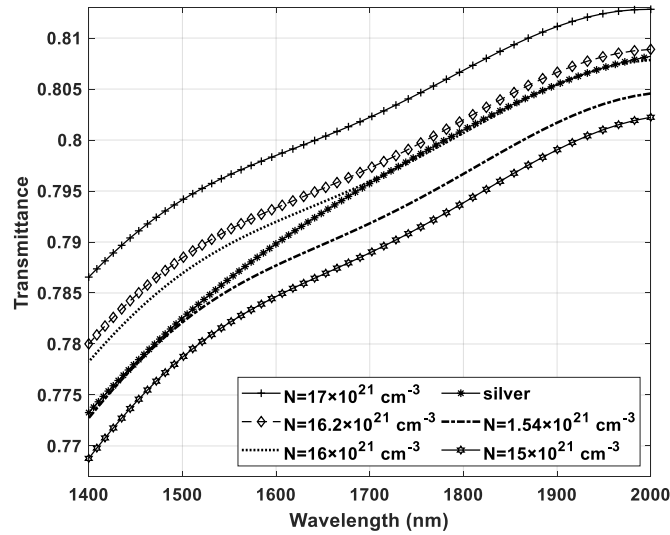
Figure 4.7: Comparison of the transmission characteristics of the p-silicon waveguide (with w = 50 nm, b = 500 nm and L = 2 μm) and silver-air-silver waveguide.

From the transmission characteristics shown in Figure 4.7, it is observed that the transmittance of the p-silicon waveguide is less than silver waveguide for carrier concentration less than 1.54×10^{22} cm^{-3} and more than silver waveguide for carrier concentration greater than 1.62×10^{22} cm^{-3}. The same observation is true for other values of w and L, which is shown in Figure 4.8, and Figure 4.9 respectively.
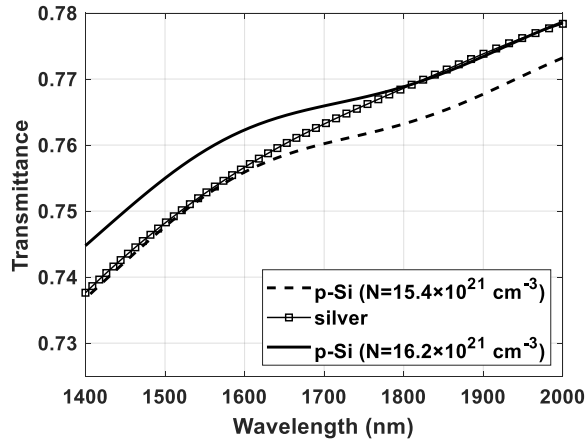
Figure 4.8: Comparison of the transmission characteristics of the p-silicon waveguide (with b = 500 nm and L = 2 μm) and silver-air-silver waveguide for (a) w = 40 nm, (b) w = 50 nm and (c) w = 60 nm.

(c)

Figure 4.9: Comparison of the transmission characteristics of the p-silicon waveguide (with w = 50 nm and b = 500 nm) and silver-air-silver waveguide for (a) L = 1500 nm, (b) L = 2000 nm and (c) L = 2500 nm.

Thus, in order to achieve a transmittance higher than the silver-air-silver waveguide, p-silicon must have a doping concentration more than 1.62×10^{22} cm^{-3}.

4.4.2 Comparison with Gold-Air-Gold Waveguide

The transmission characteristic of the p-silicon waveguide with w = 50 nm, b = 500 nm and L = 2 μm and gold-air-gold waveguide are shown in Figure 4.10.

Figure 4.10: Comparison of the transmission characteristics of the p-silicon waveguide (with w = 50 nm, b = 500 nm and L = 2 μm) and gold-air-gold waveguide.

45
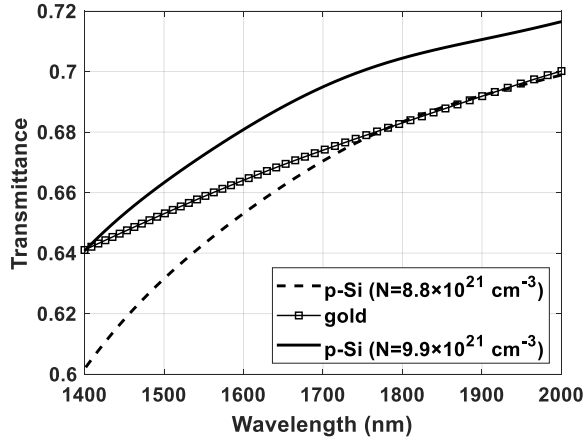
Figure 4.11: Comparison of the transmission characteristics of the p-silicon waveguide (with b = 500 nm and L = 2 µm) and gold-air-gold waveguide for (a) w = 40 nm, (b) w = 50 nm and (c) w = 60 nm.

From the transmission characteristics shown in Figure 4.10, it is observed that the transmittance of the p-silicon waveguide is less than gold waveguide for carrier concentration less than 0.88×10^{22} cm^{-3} and more than silver waveguide for carrier concentration greater than 0.99×10^{22} cm^{-3}. The same observation is true for other values of w and L, which is shown in Figure 4.11, and Figure 4.12 respectively.

Figure 4.12: Comparison of the transmission characteristics of the p-silicon waveguide (with w = 50 nm and b = 500 nm) and gold-air-gold waveguide for (a) L = 1500 nm, (b) L = 2000 nm and, (c) L = 2500 nm.

Thus, in order to achieve a transmittance higher than the gold-air-gold waveguide, p-silicon must have a doping concentration more than 0.99×10^{22} cm^{-3}.

4.5 n-Silicon waveguide

The same waveguide shown in Figure 4.3 is formed with n-silicon instead of metal and air as the insulator. The transmission characteristics with the variation of a carrier concentration of n-silicon, N, the width of air waveguide, w and the length of the waveguide, L are shown in Figure 4.13, Figure 4.14, and Figure 4.15 respectively. The relationships between transmittance and the parameters n, w and b are exactly same as those was obtained for the p-silicon waveguide.
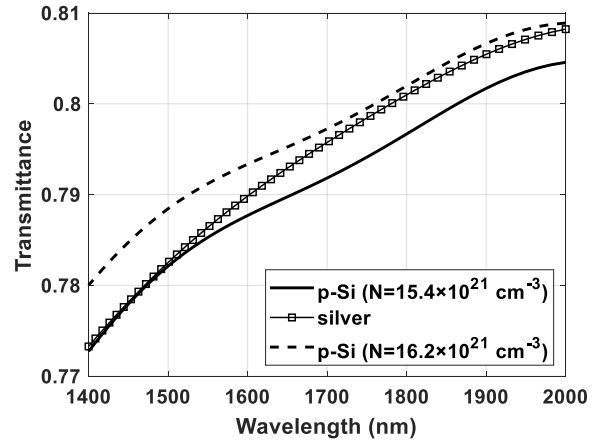
Figure 4.13: Transmission characteristics of the waveguide with w = 50 nm, b = 500 nm and L = 2 μm for different carrier concentrations of n-silicon.
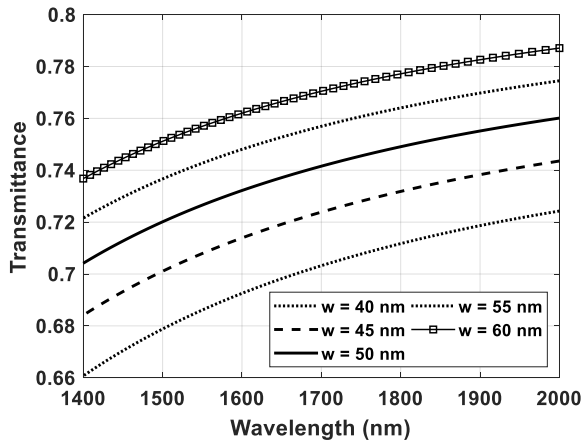
Figure 4.14: Transmission characteristics of the n-silicon waveguide with N = 8×10^{21} cm^{-3}, L = 2 μm and b = 500 nm for different values of w.
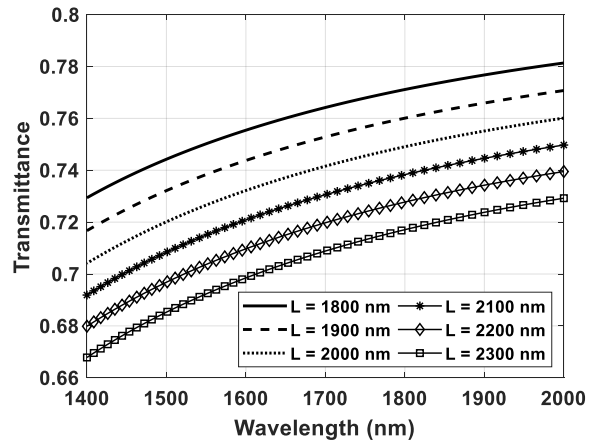
Figure 4.15: Transmission characteristics of the n-silicon waveguide with N = 8×1021 cm-3, w = 50 nm and b = 500 nm for different values of L.

4.5.1 Comparison with Silver-Air-Silver Waveguide

The transmission characteristic of the n-silicon waveguide with w = 50 nm, b = 500 nm and L = 2 µm and silver-air-silver waveguide are shown in Figure 4.16.
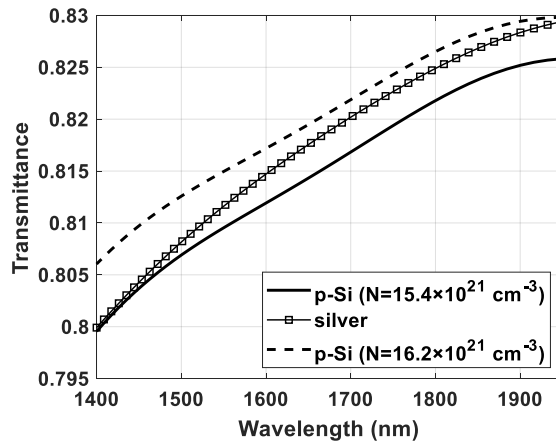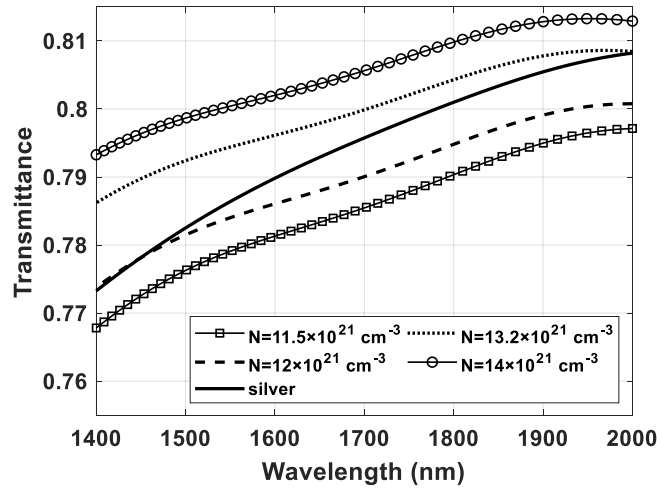

Figure 4.16: Comparison transmission characteristics of the n-silicon waveguide (with w = 50 nm, b = 500 nm and L = 2 µm) and silver-air-silver waveguide.

From the transmission characteristics shown in Figure 4.16, it is observed that the transmittance of the n-silicon waveguide is less than silver waveguide for carrier concentration less than 1.2×10^{22} cm^{-3} and more than silver waveguide for carrier concentration greater than 1.32×10^{22} cm^{-3}. The same observation is true for other values of w and L, which is shown in Figure 4.17, and Figure 4.18 respectively.
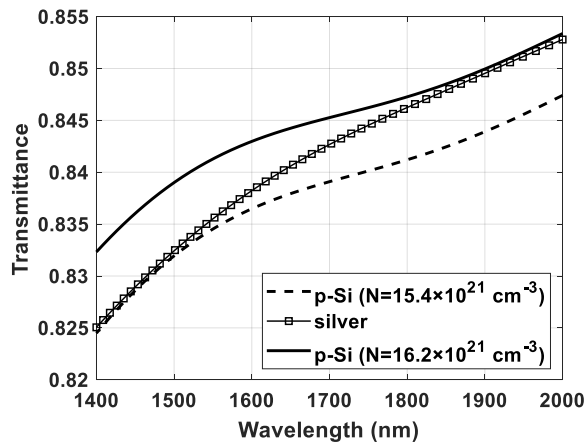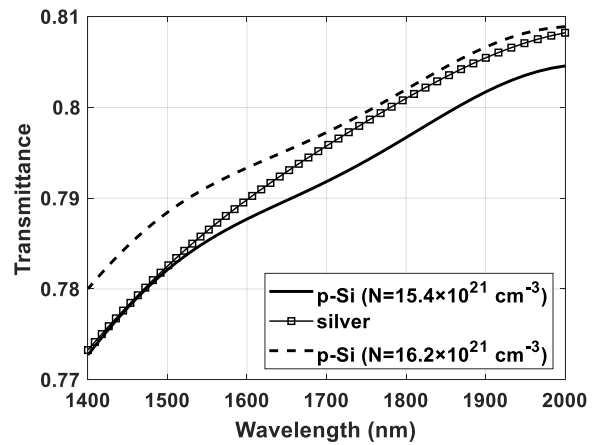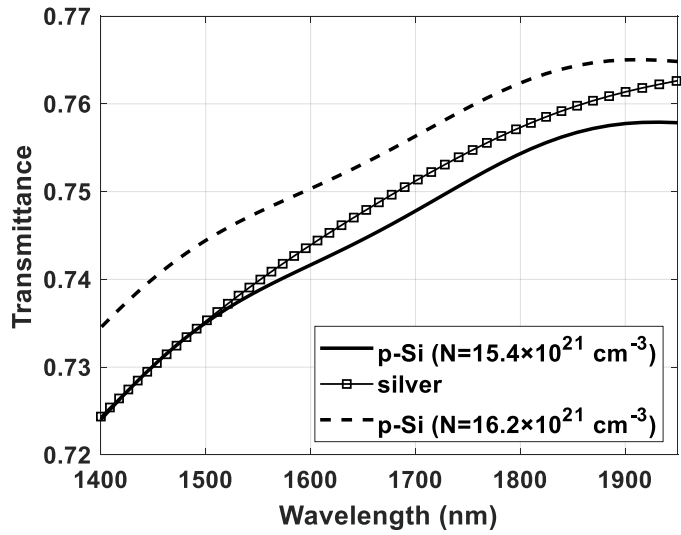

(a)

(b)
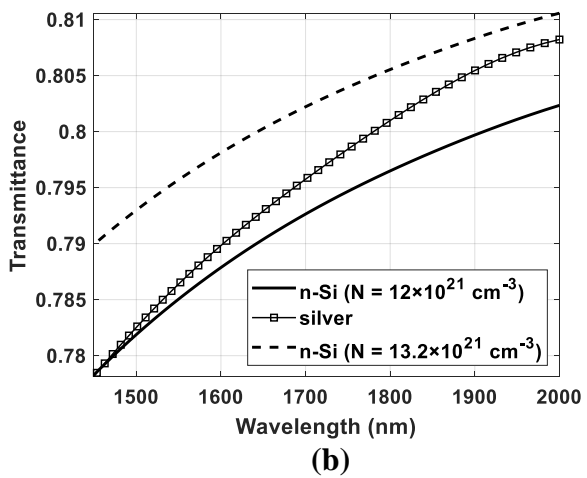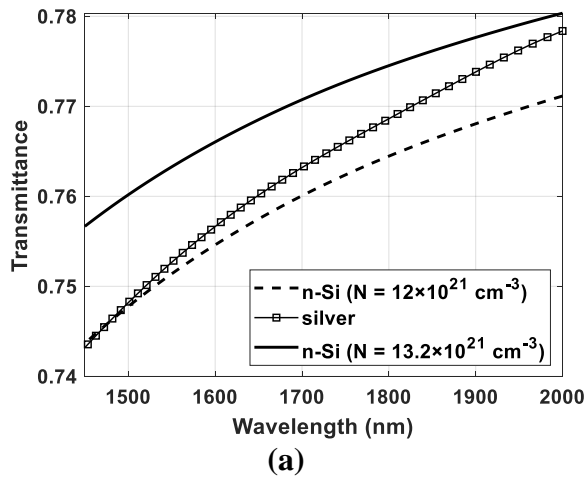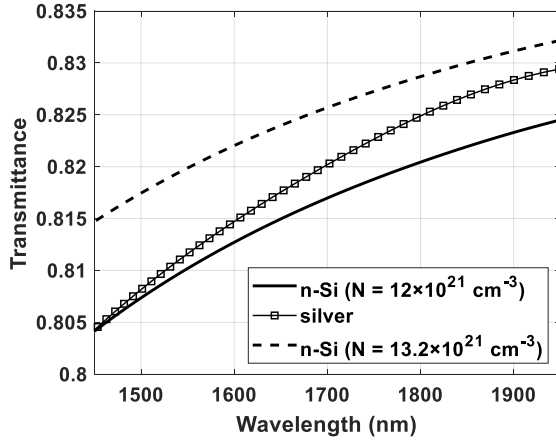
(c)

Figure 4.17: Comparison of the transmission characteristics of the n-silicon waveguide (with b = 500 nm and L = 2 µm) and silver-air-silver waveguide for (a) w = 40 nm, (b) w = 50 nm and, (c) w = 60 nm.
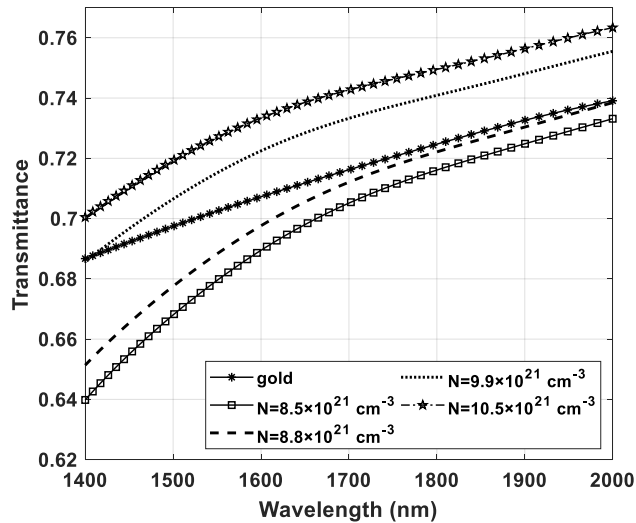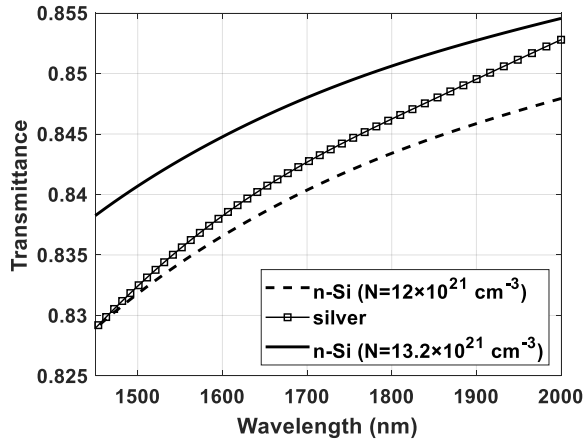

(a)
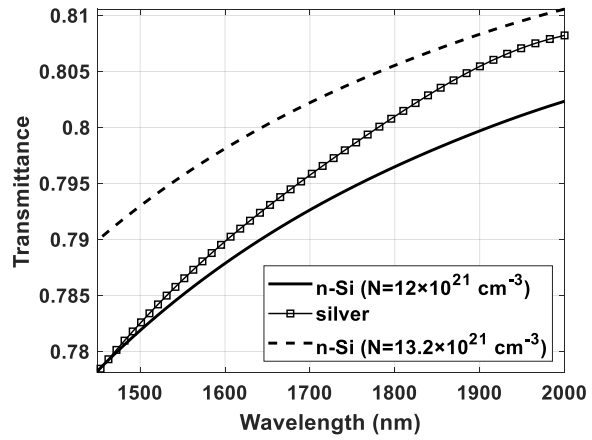
(b)
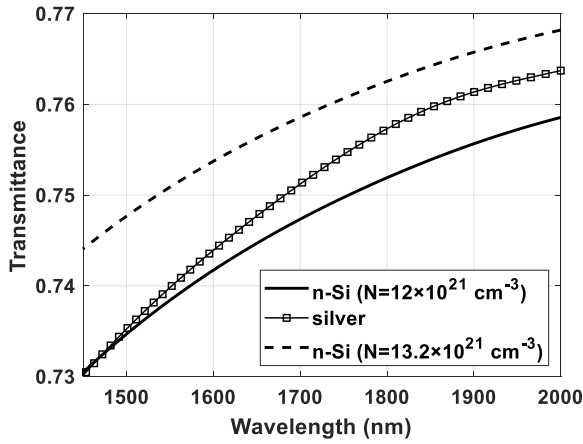
(c)

Figure 4.18: Comparison of the transmission characteristics of the n-silicon waveguide (with w = 50 nm and b = 500 nm) and silver-air-silver waveguide for (a) L = 1500 nm, (b) L = 2000 nm and, (c) L = 2500 nm.

Thus, in order to achieve a transmittance higher than the silver-air-silver waveguide, n-silicon must have a doping concentration more than 1.32×10^{22} cm^{-3}.

4.5.2 Comparison with Gold-Air-Gold Waveguide

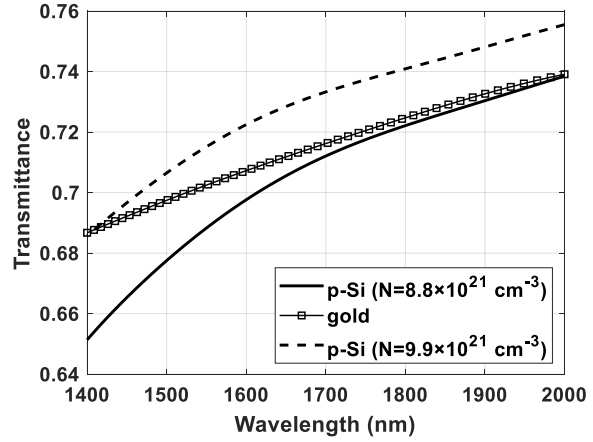The transmission characteristic of the n-silicon waveguide with w = 50 nm, b = 500 nm and L = 2 µm and gold-air-gold waveguide are shown in Figure 4.19.
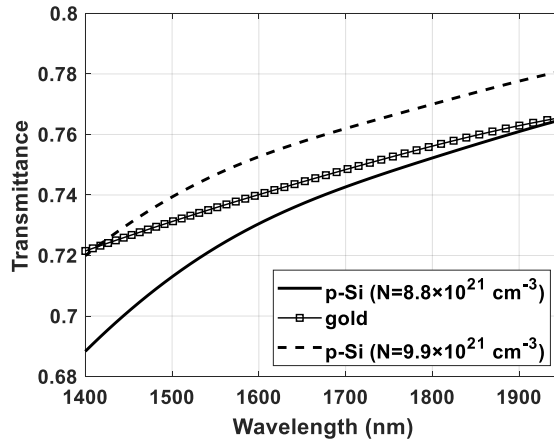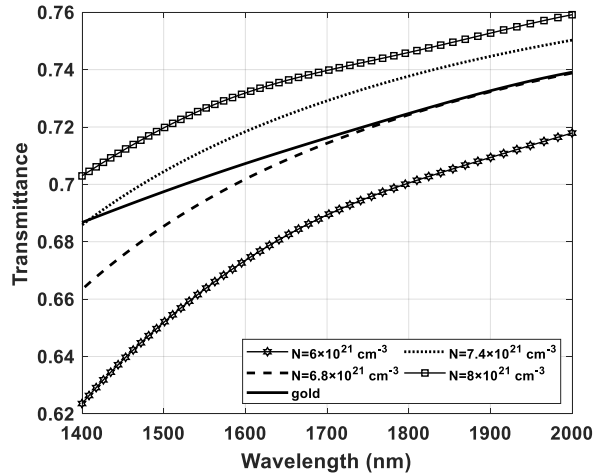

Figure 4.19: Comparison of the transmission characteristics of the n-silicon waveguide (with w = 50 nm, b = 500 nm and L = 2 µm) and gold-air-gold waveguide.

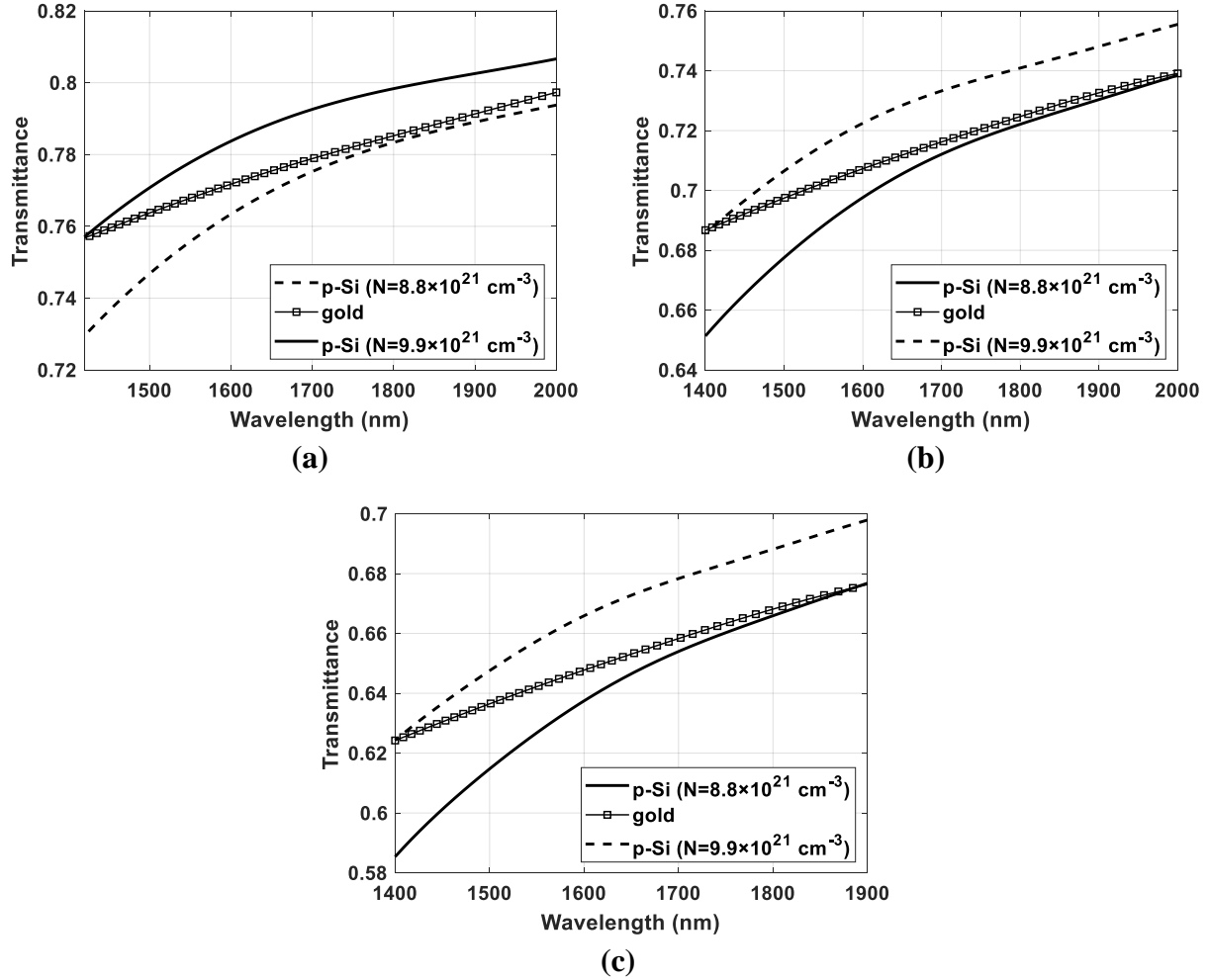From the transmission characteristics shown in Figure 4.19, it is observed that the transmittance of the n-silicon waveguide is less than gold waveguide for carrier concentration less than 0.68×10^{22} cm^{-3} and more than silver waveguide for carrier concentration greater than 0.74×10^{22} cm^{-3}. The same observation is true for other values of w and L, which is shown in Figure 4.20, and Figure 4.21 respectively.
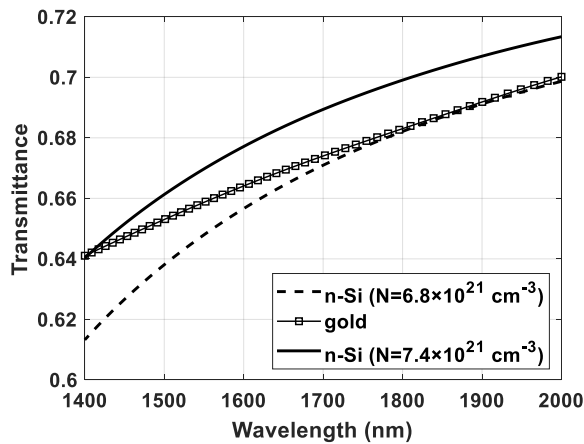
(a)
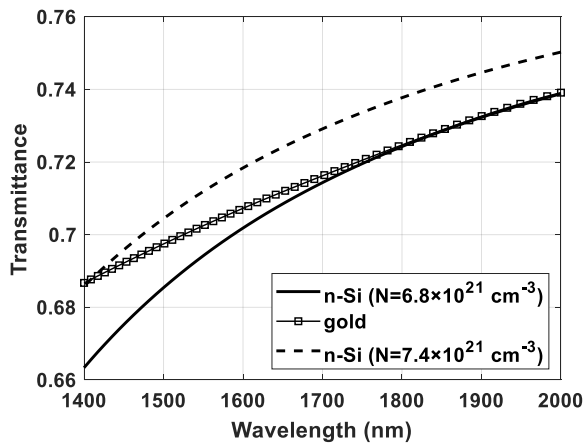
(b)
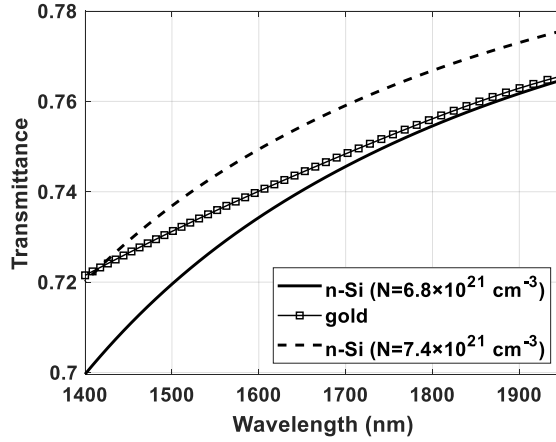
(c)

Figure 4.20: Comparison of the transmission characteristics of the n-silicon waveguide (with b = 500 nm and L = 2 µm) and gold-air-gold waveguide for (a) w = 40 nm, (b) w = 50 nm and, (c) w = 60 nm.
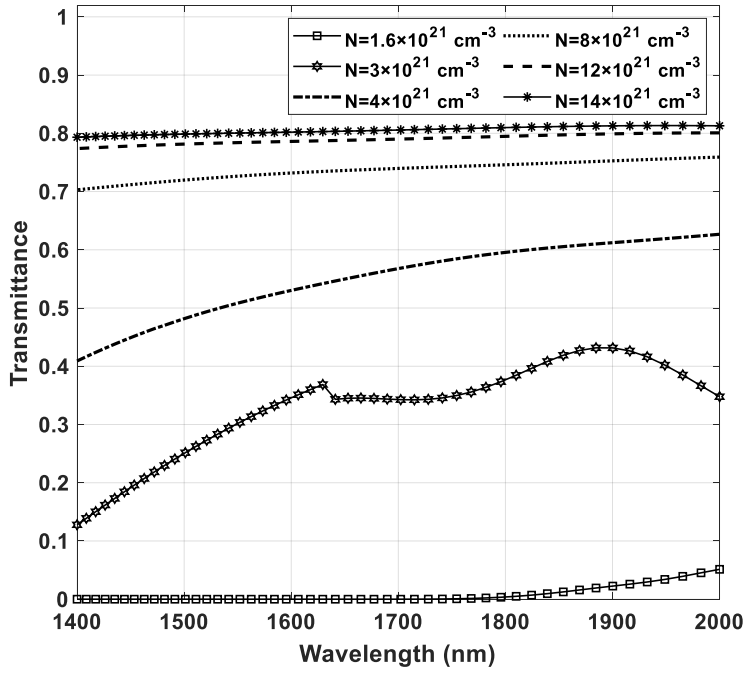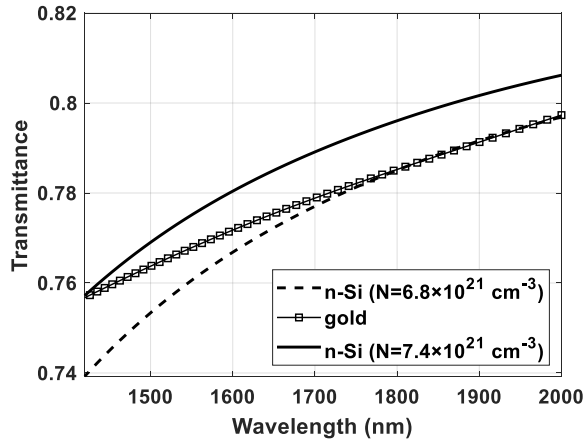

(a)
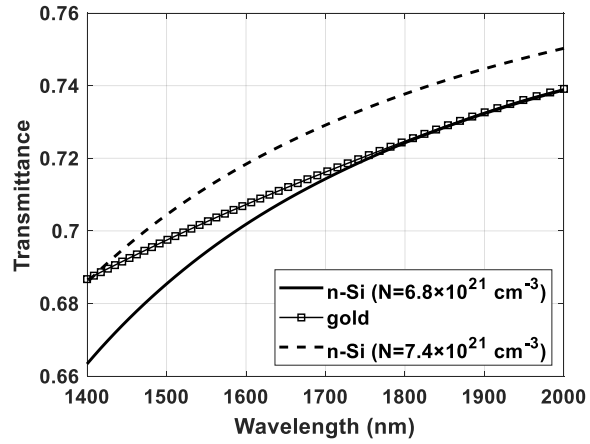
(b)
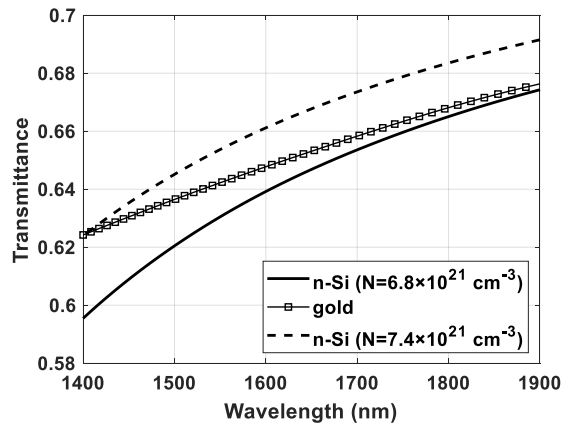
(c)

Figure 4.21: Comparison of the transmission characteristics of the n-silicon waveguide (with w = 50 nm and b = 500 nm) and gold-air-gold waveguide for (a) L = 1500 nm, (b) L = 2000 nm and, (c) L = 2500 nm.

Thus, in order to achieve a transmittance higher than the gold-air-gold waveguide, n-silicon must have a doping concentration more than 0.74×10^{22} cm^{-3}.

4.3 Selection of Suitable Waveguide

Both the waveguide formed with p-silicon and n-silicon can achieve transmittance greater than silver or gold waveguide. However, p-silicon waveguides require a higher doping concentration (1.62×10^{22}cm^{-3}) compared to n-silicon (1.32×10^{22} cm^{-3}) to achieve transmittance more than silver waveguides. Such high p-type doping in silicon is still a challenge. The maximum doping concentration reported in p-type silicon is 1×10^{21} cm^{-3} which is much lower than the required doping concentration. On the other hand, the maximum doping concentration reported in n-type silicon is 2×10^{22} cm^{-3} [126] as shown in Figure 4.22, which is higher than the doping concentration required to achieve transmittance more than silver waveguide. Thus, using n-silicon waveguide where higher transmittance is required would be an appropriate choice though p-silicon waveguide can be used in other applications where higher transmittance is not a major concern. Since n-silicon can achieve the same transmittance as p-silicon for lower carrier concentration, n-silicon waveguides are used here for designing of the plasmonic devices.
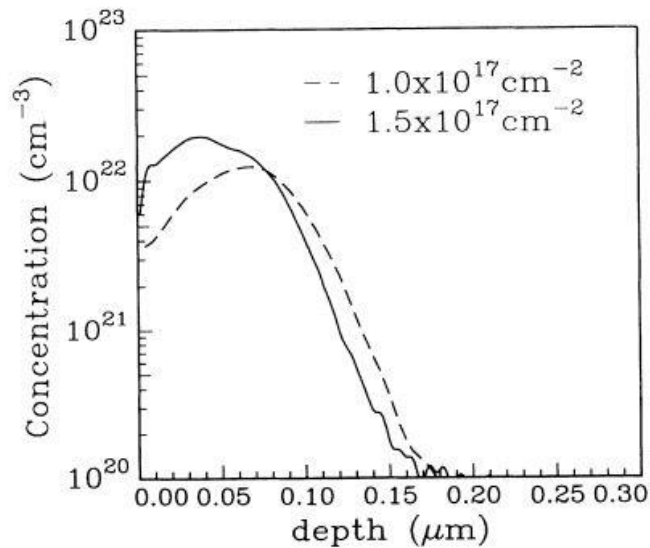
Figure 4.22: Carrier concentration measurements of the As-implanted As profiles. The dashed line refers to a sample implanted 1×10^{17} cm^{-2} at 100 keV, and the solid line to a sample which received an additional implantation of 0.5×10^{17} cm^{-2} at 50 keV as investigated by Nobili et al [126].

CHAPTER 5

PLASMONIC DEVICE DESIGN AND PERFORMANCE ANALYSIS

Optical waveguide devices are making their way towards realizing low-cost, high sensitivity, and small size devices, leading to many applications such as biological, environmental, and chemical applications [1, 7, 8]. However, most of the plasmonic devices are based on the MIM waveguide structure. This makes the integration process difficult since metals are not compatible with CMOS technology. On the other hand, silicon is the most widely used material in conventional electronic devices. Thus, designing plasmonic devices with CMOS compatible material like doped silicon may provide a way towards combining conventional electronics and plasmonics.

Among the plasmonic devices, plasmonic sensors have many applications as most of the integrated circuits require different sensing devices. Plasmonic sensors have comparatively higher sensitivity than most other sensors and are very small in size. As a result, they are suitable for being integrated into optical circuits. Researchers have proposed a number of sensors with different sensing characteristics which are already discussed in Article 1.3.4. Most of the sensors have MIM structure like the other conventional plasmonic devices. Here, two plasmonic refractive index sensors are designed with CMOS compatible material instead of metal with two different structures, one has a straight waveguide with gratings in it and the other has a ring resonator structure. Both the sensors have high sensitivity comparable with other proposed sensors.

5.1   Refractive Index Sensors

Refractive index sensors are mainly designed to sense the change in the refractive index of the material under sensing. Most of the plasmonic refractive index sensors use different types of resonator structures like ring, gratings, octagon, pentagon, rectangle, etc. to obtain a resonance peak in the transmission characteristics. The resonant peak gets shifted with the change of

refractive index of the material under sensing. The sensitivity of the device can be calculated from the resonance shift using the formula,

$$S = \frac{\Delta\lambda}{\Delta n} \dots\dots\dots\dots\dots\dots\dots\dots\dots\dots\dots\dots\dots\dots..(5.1)$$

where, S is the sensitivity, $\Delta\lambda$ is the resonant wavelength shift and Δn is the change of refractive index. Calculation of sensitivity has been explained in Figure 5.1. The device should have sensitivity, S as high as possible and Δn as small as possible to detect a very small change in the refractive index of the material under sensing.
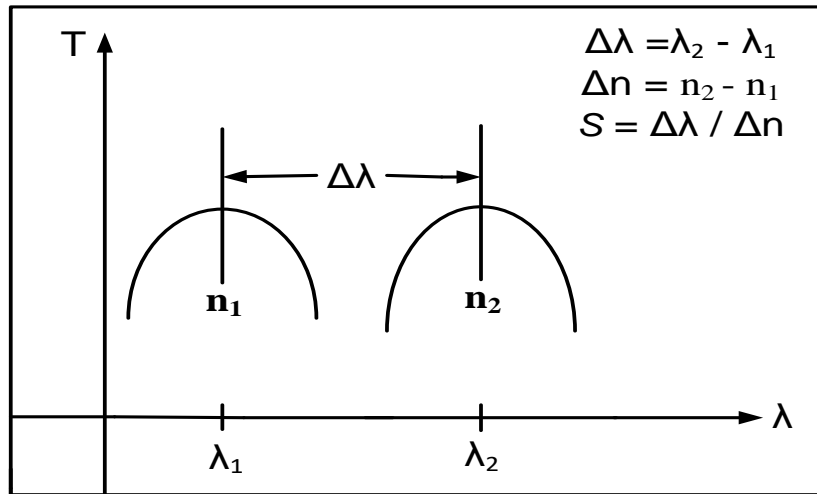
Figure 5.1: Sensitivity calculation from resonance peak shift.

5.2 Refractive Index Sensor with Gratings in a Straight Waveguide

A plasmonic refractive index (RI) sensor using heavily n-doped silicon waveguide is designed and numerically simulated using the finite element method (FEM). The sensor reported here is based on gratings inside a heavily doped silicon waveguide structure instead of conventional metal-insulator-metal structure. This feature enables the device to overcome the problems with conventional plasmonic devices. Besides, it is made up of silicon instead of metal which makes it compatible with complementary metal oxide semiconductor (CMOS) technology and thus provides an easier way of incorporation in integrated circuits. The sensor presented here has a highest sensitivity of 1208.9 nm/RIU and a resolution as small as 0.005, which is comparable with conventional plasmonic sensors reported till date. The main advantage of this plasmonic

sensor is that it has a very simple structure compared to the other plasmonic sensors and uses silicon instead of metal.

5.2.1 Basic Structure

The basic structure of the sensor is very simple. It consists of a hollow straight waveguide with grating inside a layer of n-doped silicon. The hollow space in the straight waveguide will be used to hold the material under sensing. The number of gratings may vary depending on the application. Here, the best result is obtained for two gratings in the waveguide. The basic model of the sensor is shown in Figure 5.2. For practical designing, a silicon substrate must be used under the main sensor structure. The width of the straight waveguide and the grating, w is chosen to be 20 nm, the length of the grating, h = 450 nm and the gap between two gratings, d = 250 nm. Though, for practical designing, the height of the device is also an important parameter, the sensor proposed here has been simulated in 2D like most other proposed work in order to enforce an efficient simulation [127]. For practical case, any height greater than 50 nm will provide a result which will be very close to the simulation result [15]. The 2D designing parameters of the sensor are varied during the simulation process, and the best parameters are chosen after observing the transmission characteristics.
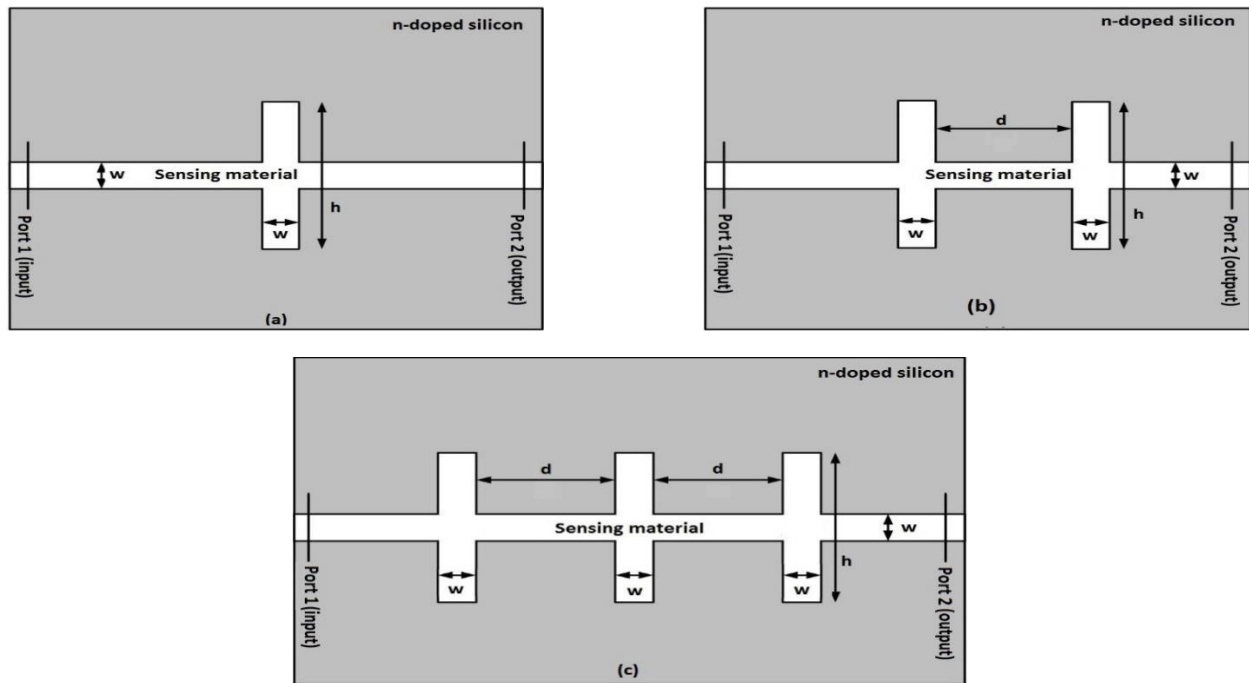
Figure 5.2: The basic structure of the sensor with (a) single grating, (b) two gratings and, (c) three gratings.

56

5.2.2 Results and Discussions

To simulate the designed sensor, commercial simulation software COMSOL Multiphysics is employed. For the simulation purpose, it utilizes the finite element method (FEM) with scattering boundary condition. At first, the simulation is done for a single grating, two gratings, and three gratings sequentially. The field distribution pattern for two gratings is shown in Figure 5.3.
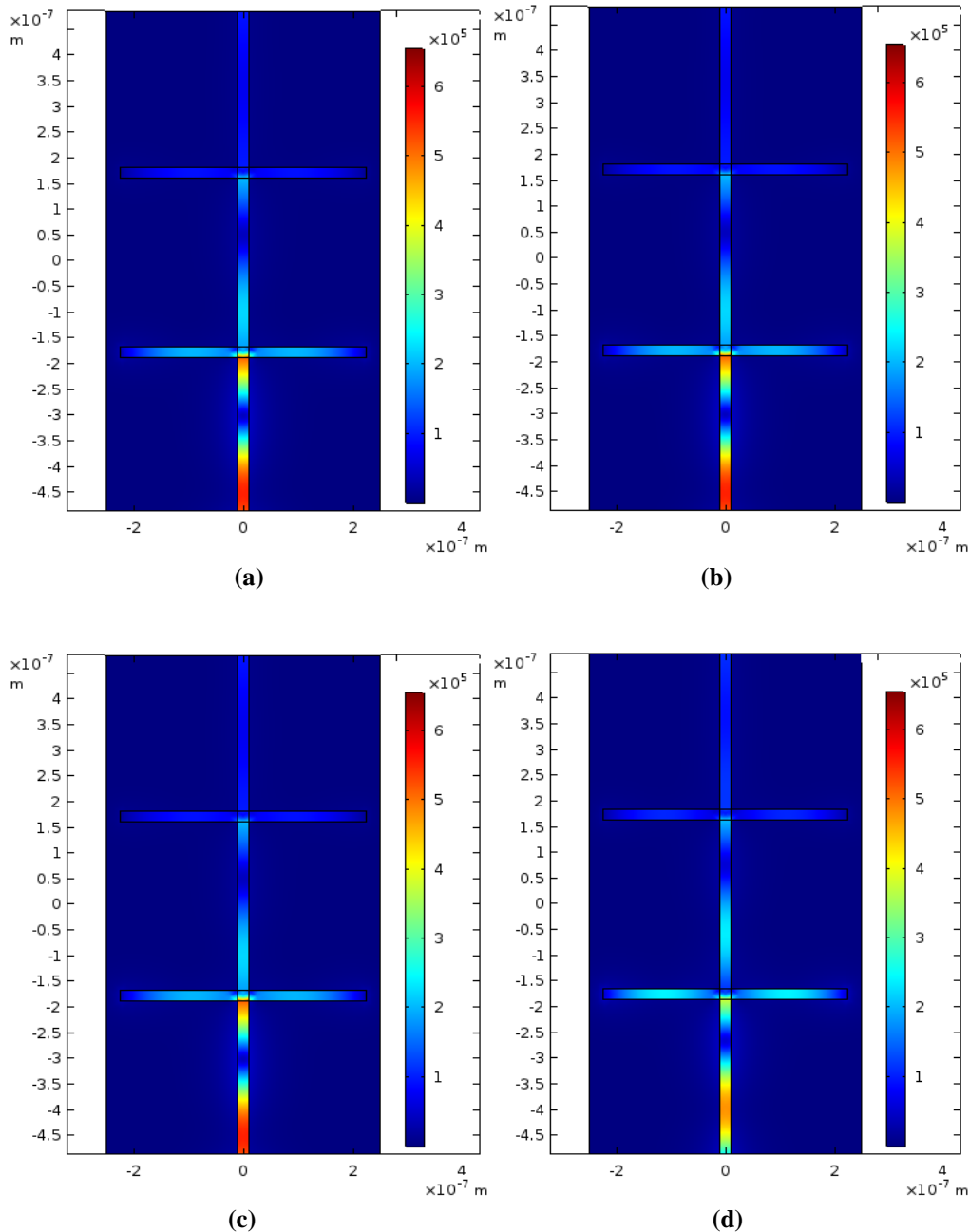
Figure 5.3: Normalized Electric Field (V/m) at frequencies (a) 1.75×10^{14} Hz, (b) 2×10^{14} Hz, (c) 2.25×10^{14} Hz and, (d) 2.5×10^{14} Hz for two gratings in the straight waveguide structure.

The transmission characteristics are shown in Figure 5.4. From the transmission characteristics in Figure 5.4, it is observed that the transmission peak with a single grating is not sharp enough. As a result, the shifting of the wave shape with the change of the refractive index will not be detectable very easily. Thus, it is not considered as a suitable structure to be used as a refractive index sensor. Next, the number of the grating is increased to two. As the wave shape with two gratings indicates, the resonance peak is sharper than the peak with a single grating and thus, can be considered as a suitable structure for the refractive index sensor. With three gratings, two resonance peaks are obtained. However, the transmittances of both the peaks are lower than the peak with two gratings. Nevertheless, it can also be utilized for the sensor structure. The number of gratings is not increased further since more gratings will cause the transmittance to be much lower.
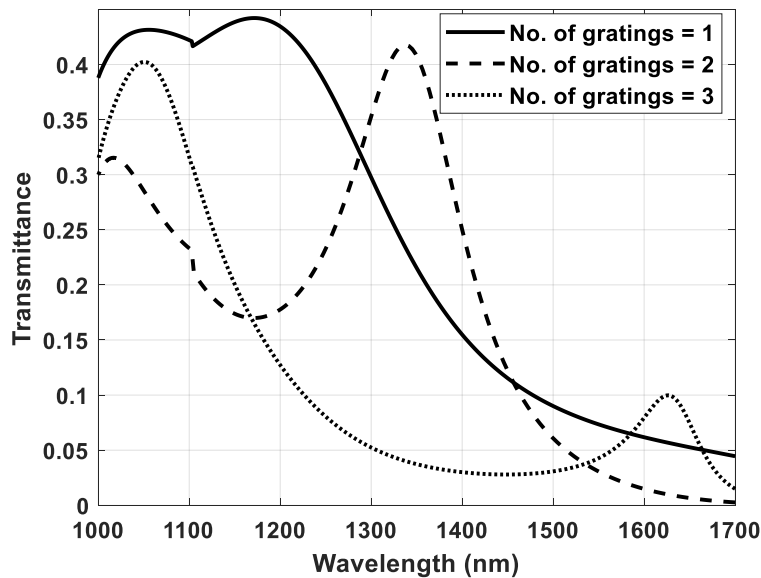
Figure 5.4: Transmission characteristics with different number of gratings with w = 20 nm, h = 400 nm and d = 250 nm.

The width of the straight waveguide and the gratings, w is then varied, and the transmission characteristics ate observed. The initial value of w was 20 nm. Now, it is varied from 10 nm to 30 nm, with a step of 5 nm. The transmission characteristics are shown in Figure 5.5. From the transmission characteristics shown in Figure 5.5, it is observed that the wave shape is distorted for w = 10 nm. For the other values of w, the transmittance gradually increases with the increase in width, w and the resonance peak also suffers a left shift. For w = 15 nm, 20 nm, 25 nm, and 30 nm, the resonance peaks have transmittances 0.27, 0.32, 0.34 and 0.35 respectively. Though each

of the structures with w = 20 nm, 25 nm, and 30 nm have a higher transmission, resonance peak of the structure with w = 25 nm and 30 nm suffers a large left shift and resonance occurs at wavelengths smaller than 1200 nm. Since we tried to design a sensor which operates between 1300 nm and 1400 nm, we have chosen w = 20 nm. For the sensors which will be operated in any other ranges like greater than 1400 nm, 1100 nm to 1200 nm, smaller than 1100 nm, the values of w = 15 nm, 25 nm and 30 nm respectively may be chosen.
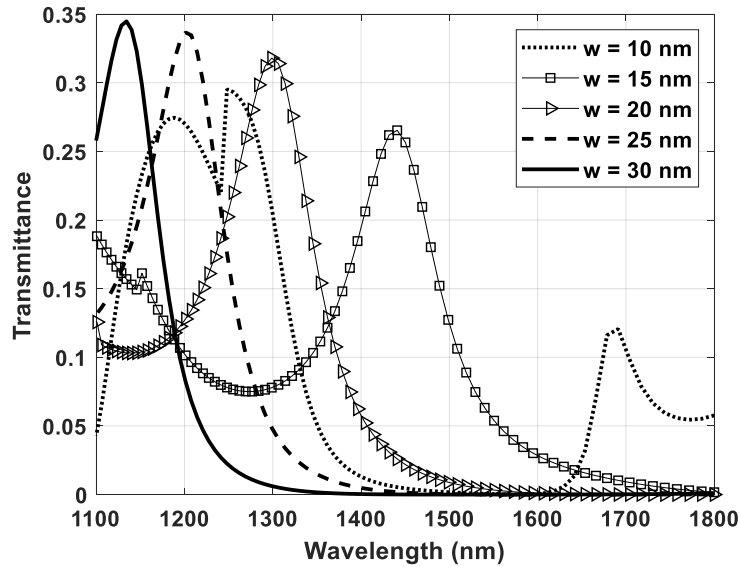
Figure 5.5: Transmission characteristics of the sensor with h = 400 nm, d = 250 nm and different values of w.

The distance between the two gratings, d is then varied from 200 nm to 350 nm, and the transmission characteristics are analyzed. The transmission characteristics are shown in Figure 5.6. With the increase in distance between the gratings, the transmittance of the resonance peak gradually reduces, and the resonance peak suffers a right shift. The structure with a smaller gap between the gratings has provided a better transmittance of the resonance peak. The resonance peak of the smallest gap, d = 200 nm, is obtained in the range smaller than 1200 nm. Thus the value of d is chosen to be 250 nm to have a reasonably high transmittance (> 0.3) of the resonance peak and also to keep the operating point between 1300 nm to 1400 nm.
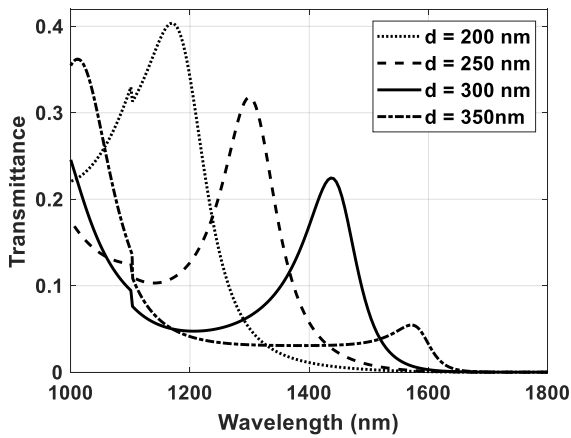
Figure 5.6: Transmission characteristics of the sensor with w = 20 nm, h = 400 nm and different values of d.
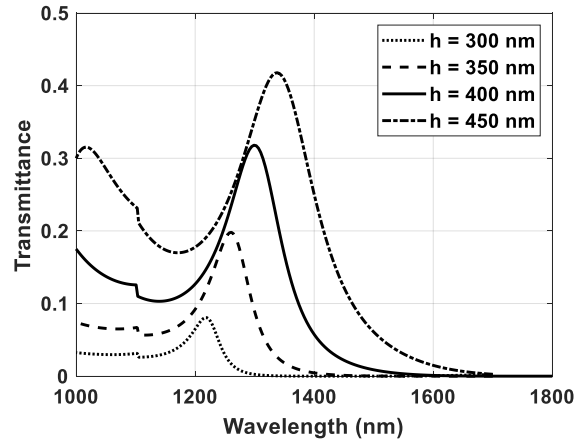
Figure 5.7: Transmission characteristics of the sensor with w = 20 nm, d = 250 nm and different values of h.

Lastly, the length of the grating, h, is varied, and the effects of variations are evaluated. The smallest value of h is chosen to be 300 nm, as the transmittance becomes very low with h smaller than 300 nm. h is then varied up to 450 nm, and the transmission characteristics with different values of h are shown in Figure 5.7. As observed in Figure 5.7, the transmittance of the resonance peak is highest for the largest value of h. The resonance peak is also within the operating range of 1300 nm to 1400 nm. Thus, h = 450 nm is chosen for further simulation of the sensor.

With the parameters of the sensor structure chosen to be w = 20 nm, d = 250 nm and h = 450 nm, the refractive index of the material under sensing, n, is gradually increased from 1 with a step of 0.005 and the transmission characteristics are observed which is shown in Figure 5.8. The resonance peaks are observed to be shifted with the change of the value of n. The sensitivity can be calculated from the resonance shift using (5.1).

The resonance peak shift with the change of the refractive index of the sensing material and the sensitivities for different values of n is shown in Table 5.1. From Table 5.1, it is seen that a maximum sensitivity of 1208.9 nm/RIU is obtained for the designed sensor. It can detect a change in the refractive index as small as 0.005. The plot of the resonance peak against the refractive index is shown in Figure 5.9, which shows that the resonance wavelength shift with the change of the refractive index is almost linear. Thus, it can be expected to have a linear

resonance shift for refractive indices beyond 1.03 and can be used to sense those. The number of gratings is then increased to three, and the transmission characteristics are analyzed for refractive indices 1 and 1.01. The transmission spectrum is shown in Figure 5.10. The resonant peaks are obtained at 1050.3 nm and 1058.5 nm for n = 1 and n = 1.01 respectively. The sensitivity obtained here is 825.64 nm/RIU. Since the sensitivity of the device reduces for this structure, the sensor with three or more gratings is not taken into consideration.
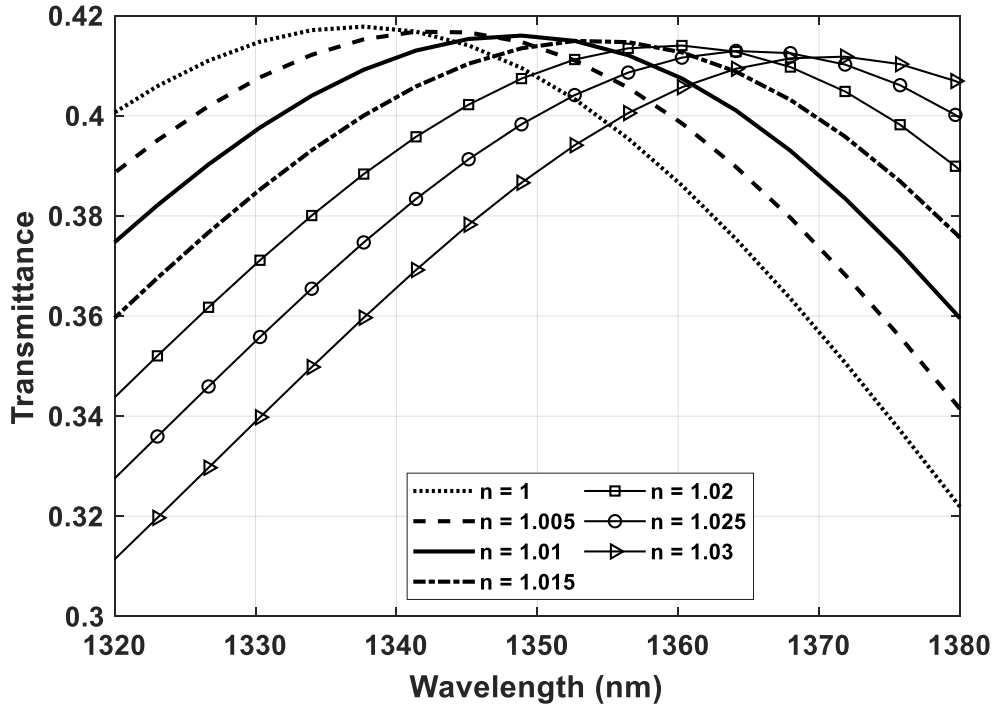
Figure 5.8: Transmission characteristics of the sensor with w = 20 nm, d = 250 nm, h = 450 nm and n = 1, 1.005, 1.01, 1.015, 1.02, 1.025 and 1.03.

Table 5.1: Resonance shift and sensitivity for different values of n.

n	Resonance Peak (nm)	Resonance Shift (nm)	Sensitivity (nm/RIU)
1	1337.7	-------	-------
1.005	1343.1	5.4128	1082.6
1.01	1348.9	5.7879	1157.6
1.015	1354.4	5.4754	1095.1
1.02	1360.3	5.9145	1182.9
1.025	1365.8	5.5395	1107.9
1.03	1371.9	6.0444	1208.9
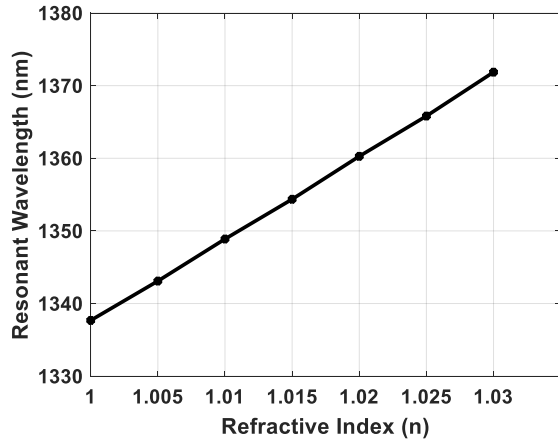
Figure 5.10: Transmission characteristics of the sensor with three gratings with w = 20 nm, d = 250 nm, h = 450 nm and   n = 1, 1.01.
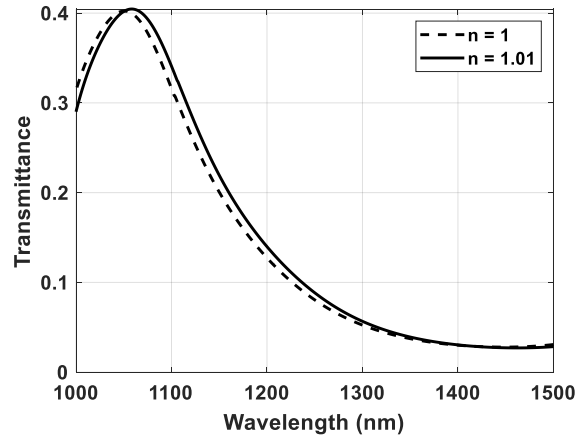
Figure 5.9: Resonant wavelength shifts with the change of the refractive index.

5.2.3   Conclusions

A plasmonic sensor with alternative plasmonic material is designed here. The sensor has a very simple structure with a straight waveguide with gratings. The device is made up of silicon only, which makes it similar to Silicon-On-Insulator (SOI) structures. Thus, it becomes compatible with CMOS technology. The maximum sensitivity of the device is 1208.9 nm/RIU, and it can sense refractive index change as small as 0.005, which is comparable with the other proposed plasmonic sensors. Thus, it can be used in the integrated circuits for refractive index sensing applications very easily.

5.3 Refractive Index Sensor with a Ring Resonator

A plasmonic refractive index (RI) sensor based on highly doped silicon waveguide is proposed and investigated numerically. The RI sensor utilizes a heavily doped silicon waveguide instead of conventional MIM waveguide which makes it CMOS compatible. A ring waveguide is coupled with the straight waveguide like MIM ring resonator structures, and similar resonance phenomenon is observed. The sensitivity is investigated, and a sensitivity of 4900 nm/RIU is realized. The plasmonic sensor consists of a simple framework and uses only silicon waveguide and does not require any special material which makes it suitable for sensing system in integrated optical circuits.

5.3.1 Basic Structure

The basic scheme of the plasmonic sensor is composed of a straight waveguide of silicon-air-silicon structure which is connected with a ring cavity inside the silicon layer in which there will be the material under sensing. Refractive index and temperature sensor of the similar structure have been investigated by Wu et al. [35] where a highest sensitivity of 3460 nm/RIU has been observed. This is one of the highest sensitivity reported for plasmonic refractive index sensor till date. Figure 5.11 shows the 3D and 2D models of the sensor, respectively. Here, w = 10 nm, r = 170 nm, d = 50 nm is chosen. The same structure has also been investigated here using heavily doped n-type silicon instead of silver. The device has been tuned to operate for wavelengths smaller than 2300 nm since the modeling of n-silicon gave a low percentage of error for this wavelength range.
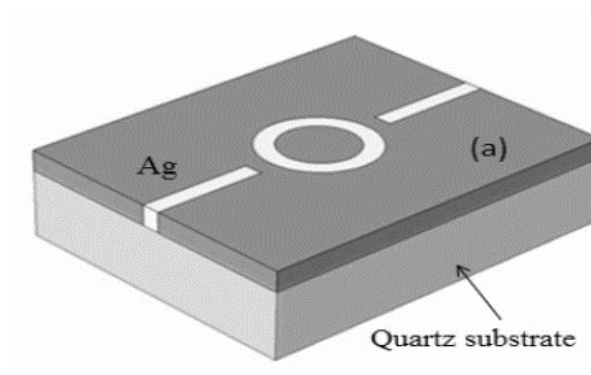
(a)
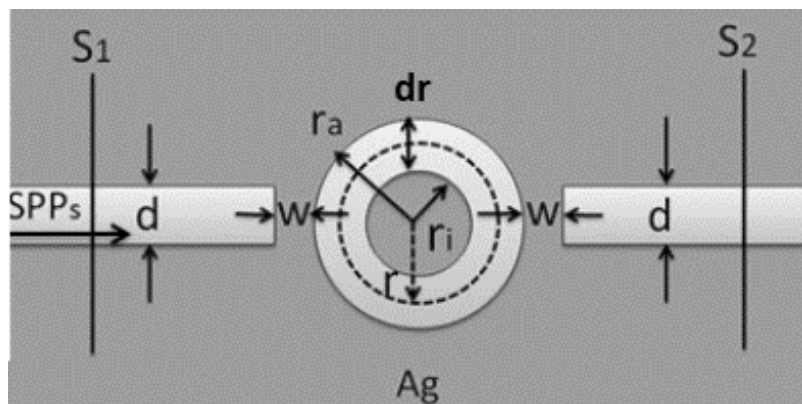
(b)

Figure 5.11: (a) 3D and, (b) 2D model of the sensor proposed by Wu et al. [35].

5.3.2 Results and Discussions

The same structure is simulated using COMSOL with n-silicon with a carrier concentration of 1.32×10^{22} cm^{-3}, the minimum carrier concentration for which it has transmittance more than silver waveguide. The field distribution pattern is shown in Figure 5.12. The transmission characteristic is shown in Figure 5.13. For this structure, the resonance peaks occur at 1573.5 nm, 1589 nm, 1604.3 nm and 1619.5 nm for n = 1, 1.01, 1.02 and 1.03 respectively. The sensitivities obtained are 1550 nm/RIU, 1530 nm/RIU and 1520 nm/RIU, respectively. Thus,a maximum sensitivity of 1550 nm/RIU is obtained for the device structure.

(a)

(b)

(c)

(d)
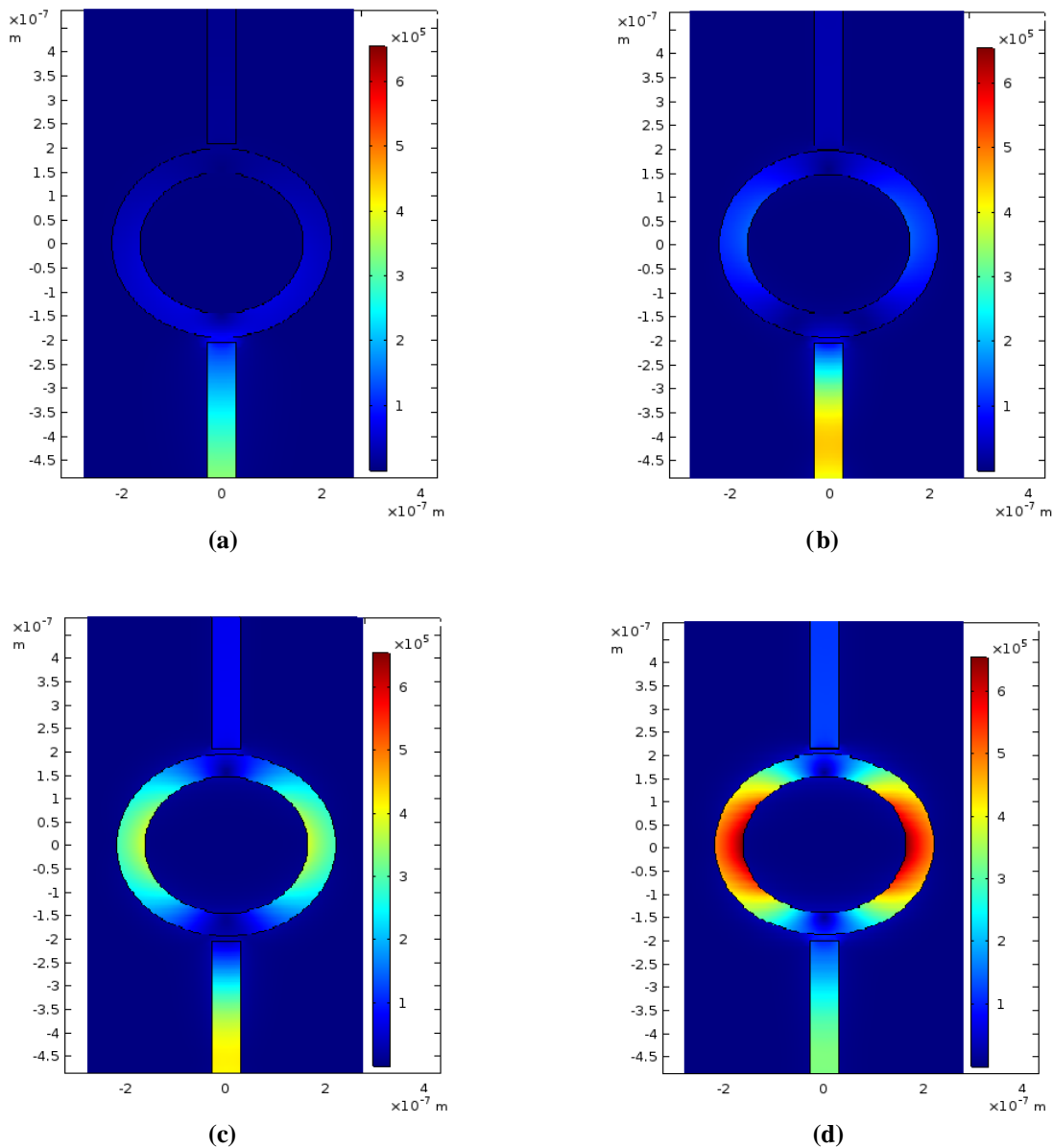
Figure 5.12: Normalized Electric Field (V/m) at frequencies (a) 1.75×10^{14} Hz, (b) 2×10^{14} Hz, (c) 2.25×10^{14} Hz and, (d) 2.5×10^{14} Hz for the ring resonator sensor.

64

The width of the ring, dr is varied for getting maximum sensitivity. For dr = 40 nm, 50 nm and 60 nm, the transmission characteristics are observed for n = 1 and n = 1.01, which is shown in Fig 5.14. The resonance peaks and the sensitivities for different values of dr are shown in table 5.2. From Table 5.2, it is observed that the sensitivity increases with the decrease of the radius of the ring. However, it exceeds our highest operating wavelength for ring width smaller than 20 nm. Thus, ring width, dr = 20 nm is chosen to obtain the highest sensitivity. The resonance peaks obtained for dr = 20 nm is at 2204 nm, and sensitivity is as high as 4201.9 nm/RIU.
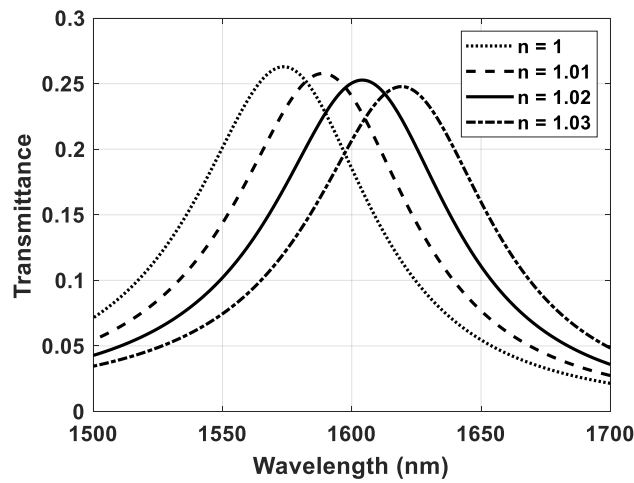
Figure 5.13: Transmission characteristics of the sensor with w = 10 nm, r = 170 nm and d = 50 nm for different values of n.
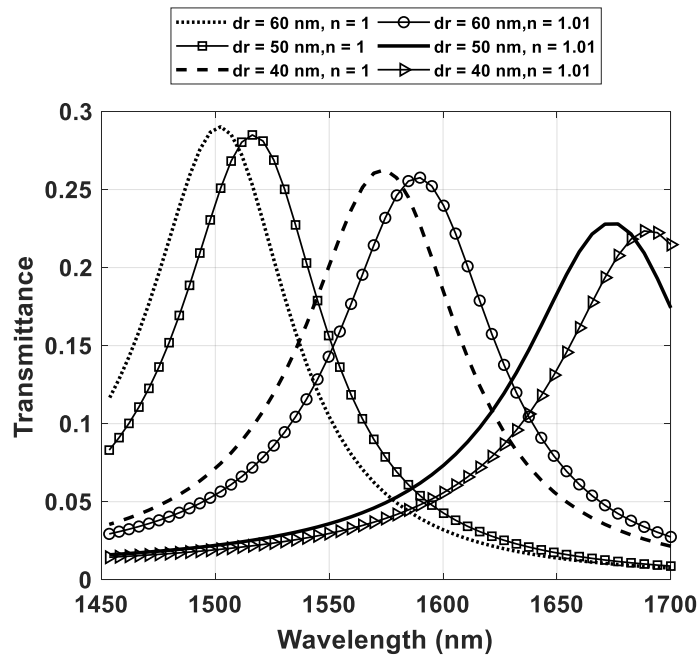
Figure 5.14: Transmission characteristics of the sensor with w = 10 nm, r = 170 nm and ds = 50 nm for different values of dr for n = 1 and n = 1.01.

Table 5.2: The resonance peaks and the sensitivities for different values of ring width, ds.

Ring width, dr (nm)	Resonance peaks (nm)		Sensitivity (nm/RIU)
	n = 1	n = 1.01	
20	2204.881	2246.9	4201.9
30	1827.5	1844.7	1720
40	1674.2	1689.8	1689.8
50	1574	1589	1589
60	1501.7	1516.05	1516.05
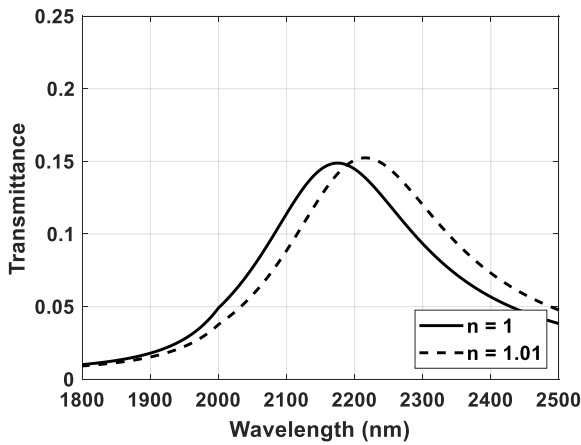
(a)
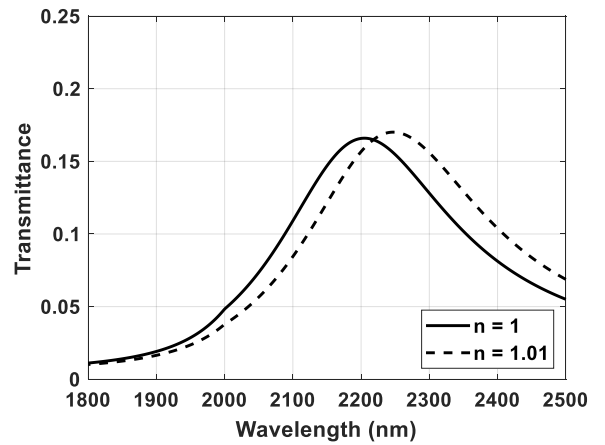
(b)
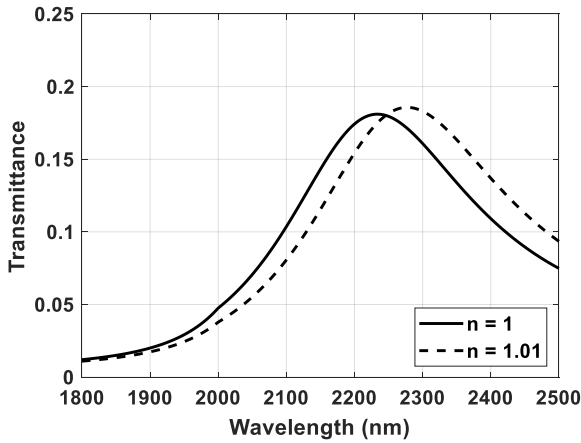
(c)
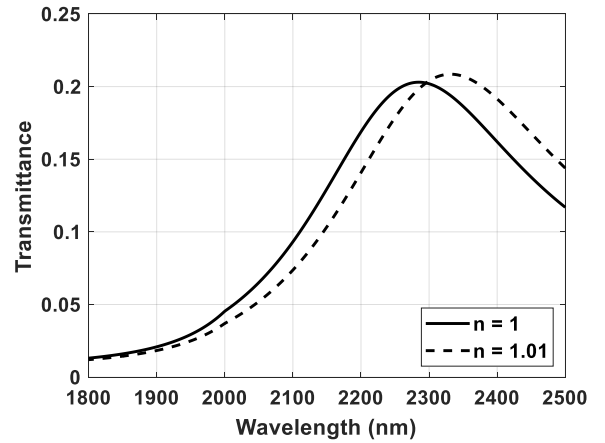
(d)

Figure 5.15: Transmission characteristics of the sensor with w = 10 nm, r = 170 nm and dr = 20 nm, for (a) ds = 40 nm, (b) ds = 50 nm, (c) ds = 60 nm, and (d) ds = 80nm, for n = 1 and n = 1.01.

The width of the straight waveguide, ds is then varied for n = 1 and n= 1.01 to obtain the value of ds for maximum sensitivity. The transmission characteristics and the resonance peaks for

different values of ds are shown in Figure 5.15 and Table 5.3, respectively. The sensitivity of the device increases with the increase of ds and the resonance peak for n = 1moves beyond 2300 nm for ds greater than 80 nm. Thus, ds = 80 nm is chosen where the sensitivity obtained is 4650 nm/RIU.

Table 5.3: The resonance peaks and the sensitivities for different values of ds.

Width of the straight waveguide, ds (nm)	Resonance peaks (nm)		Sensitivity (nm/RIU)
	n = 1	n = 1.01	
40	2175.2	2215	3980
50	2204.88	2246.9	4202
60	2230	2272.5	4250
70	2255	2300	4500
80	2285	2331.5	4650
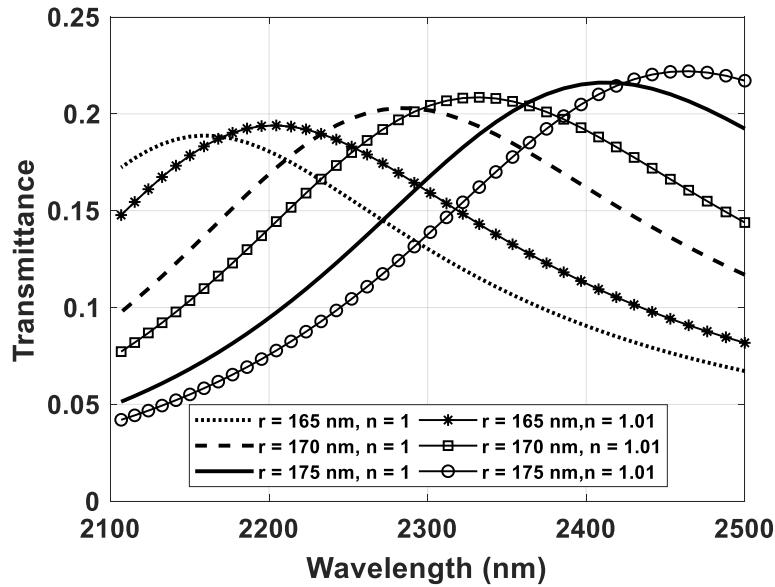
Figure 5.16: Transmission characteristics of the sensor with w = 10 nm, dr = 20 nm and ds = 80 nm for different values of rfor n = 1 and n = 1.01.
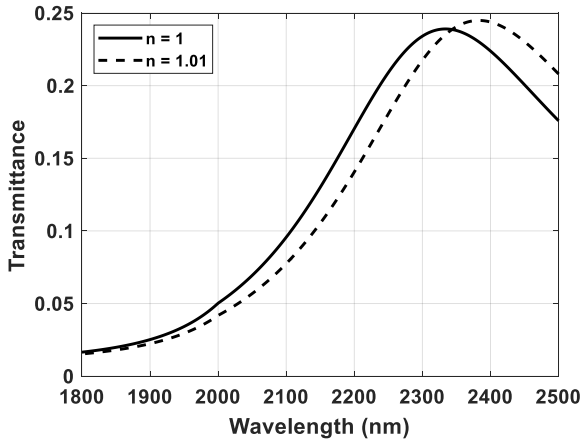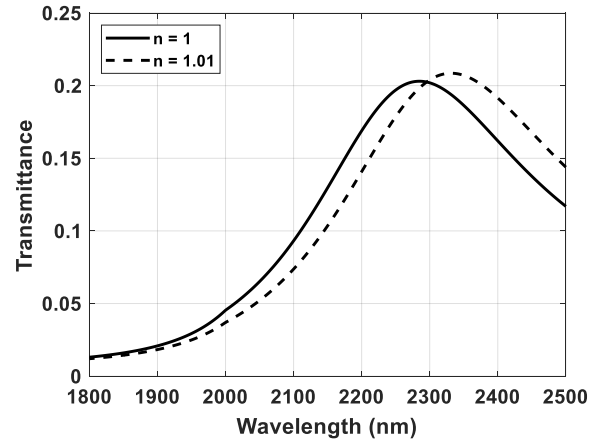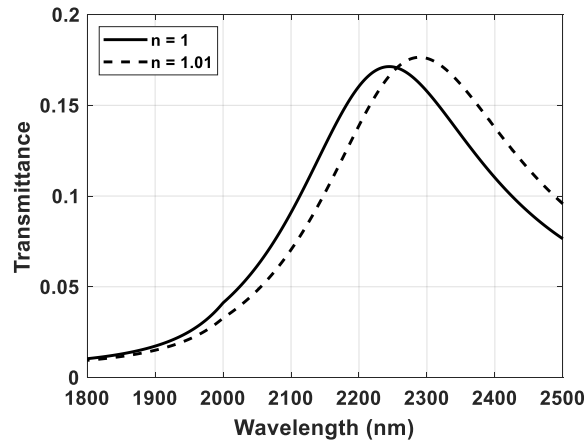
Figure 5.17: Transmission characteristics of the sensor with ds = 80 nm, r = 170 nm and dr = 20 nm for (a) w = 9 nm, (b) w = 10 nm, and (c) w = 11 nm, for n = 1 and n = 1.01.

The other parameters to choose are the radius of the ring, r and the gap between the straight waveguide and ring waveguide, w. These parameters are also varied similarly, and the best values of r and w are chosen for best sensitivity and suitable operating wavelengths. The transmission characteristics with the variation of r and w are shown in Figure 5.16, and Figure 5.17 respectively. The resonance peaks and sensitivities for different values of r and w are shown in Table 5.4 and Table 5.5, respectively. From table 5.4 and Table 5.5, the best value of r is chosen to be 170 nm, and the best value of w is chosen to be 10 nm.

Table 5.4: The resonance peaks and the sensitivities for different values of ring radius, r.

The radius of the ring waveguide, r (nm)	Resonance peaks (nm)		Sensitivity (nm/RIU)
	n = 1	n = 1.01	
165	2160	2202.7	4270
170	2285	2331.5	4650
175	2412.25	2462.3	5005

Table 5.5: Resonance peaks and sensitivities for different values of the gap between the straight and ring waveguide, w

Gap between the straight and ring waveguide, w (nm)	Resonance peaks (nm)		Sensitivity (nm/RIU)
	n = 1	n = 1.01	
9	2333.7	2382.45	4875
10	2285	2331.5	4650
11	2244.66	2289.6	4494
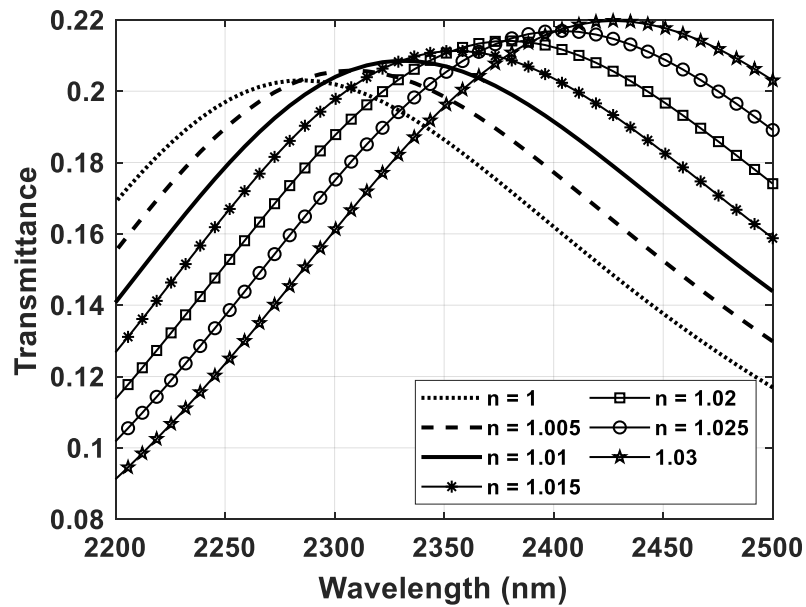
Figure 5.18: Transmission characteristics of the sensor with ds = 80 nm, r = 170 nm and dr = 20 nm and w = 10 nm for different values of n.

With all the suitable values for the sensor as dr = 20 nm, ds = 80 nm, r = 170 nm and w = 10 nm, the transmission characteristics are observed for different values of n from 1 to 1.03 with a step of 0.005. the transmission characteristics for different values of n are shown in Figure 5.18. The resonance peaks for different values of n and sensitivity is shown in Table 5.6.

Table 5.6: Resonance peaks and sensitivities for different values n.

n	Resonance peak (nm)	Sensitivity (nm/RIU)
1	2284.9	--------
1.005	2307.94	4608
1.01	2331.47	4706
1.015	2355	4706
1.02	2379	4800
1.025	2403	4800
1.03	2427.5	4900

From Table 5.6, it is observed that a highest sensitivity of 4900 nm/RIU can be obtained for the sensor.

5.3.3 Conclusions

A plasmonic refractive index sensor with high sensitivity, compact design, and using heavily doped n-silicon instead of metal has been proposed and investigated here. The sensor proposed here has the highest sensitivity of 4900 nm/RIU, which is higher than most of the plasmonic sensor reported till date. It can also detect refractive index change as small as 0.005. The main advantage of this sensor is that it is made up of silicon instead of metal which makes the device compatible with CMOS technology.

CHAPTER 6

CONCLUSION AND FUTURE WORKS

6.1   Summary and Conclusions

An investigation is made here to find a suitable alternative to metal in order to replace them in plasmonic devices. Metals show negative real part of its dielectric permittivity at optical frequencies which is mainly responsible for SPP propagation in plasmonic devices. Besides, it has a positive imaginary part of its permittivity, which causes an optical loss in plasmonic devices. Thus, an alternative material with a negative real part and smaller or zero imaginary part of its complex dielectric permittivity would be a suitable replacement of metals.

Heavily doped silicon, both p-type and n-type has been investigated as potential replacements. Both of the materials can show negative relative permittivity like metals after a certain doping concentration. In p-type silicon, the doping concentration required to achieve metal-like properties is higher than in n-type silicon. The imaginary part of the permittivity is also very small in doped silicon compared to metals. Thus, heavily doped silicon can be used as an alternative to metals in SPP formation and propagation in plasmonic devices.

Waveguides are formed with both p-type and n-type silicon and compared with conventional metal waveguides. The doping concentration required in p-type silicon waveguide is 1.62×10^{22} cm^{-3} and 1.32×10^{22} cm^{-3} in n-type silicon waveguide in order to achieve transmittance higher than silver waveguide. Such heavy doping in p-type silicon is still a challenge. On the other hand, the higher doping concentration in n-type silicon has been practically reported. Thus, heavily doped n-type silicon is chosen as the plasmonic material to replace metals in plasmonic devices.

Two plasmonic refractive index sensors have been proposed and numerically investigated using heavily doped n-type silicon instead of metal. Comparison between the other proposed sensor and the sensors proposed is shown in Table 6.1.

Table 6.1: Comparison with other proposed sensors.

Proposed Sensor	Maximum Sensitivity (nm/RIU)	CMOS Compatibility
Sensor with gratings in a straight waveguide proposed here	1208.9	Yes
Sensor with ring resonator proposed here	4900	Yes
Wu et al. [35]	3460	No
Zhang et al. [14]	1200	No
Zhang et al. [15]	1060	No
Butt et al. [16]	800	No
Zhang et al. [128]	1100	No
Tu et al. [129]	363	Yes

From table 6.1, it can be observed that the sensor with the ring resonator proposed here has higher sensitivity than the other proposed sensors. Besides, both the sensors have CMOS compatibility, unlike most other sensors. Thus, the plasmonic sensors proposed here with alternative plasmonic material can be considered as high performing and compatible with the present technology compared to the conventional plasmonic devices.

6.2   Future Works

With the current progress of the work, several future goals can be achieved.

- Since the mathematical model is verified for doped silicon, other doped semiconductors like germanium; GaAs etc. can be modeled and used for simulating plasmonic structures.
- Heavily doped p-type and n-type silicon can be used to design other plasmonic devices like filters, couplers, splitters etc. with improved performances.

References

[1]   W. L. Barnes, A. Dereux, and T. W. Ebbesen, "Surface plasmon subwavelength optics," *nature,* vol. 424, p. 824, 2003.

[2]   Z. Han, L. Liu, and E. Forsberg, "Ultra-compact directional couplers and Mach–Zehnder interferometers employing surface plasmon polaritons," *Optics communications,* vol. 259, pp. 690-695, 2006.

[3]   Z. Kang and G. P. Wang, "Coupled metal gap waveguides as plasmonic wavelength sorters," *Optics Express,* vol. 16, pp. 7680-7685, 2008.

[4]   D. K. Gramotnev and S. I. Bozhevolnyi, "Nanofocusing of electromagnetic radiation," *Nature Photonics,* vol. 8, p. 13, 2014.

[5]   V. A. Zenin, A. Andryieuski, R. Malureanu, I. P. Radko, V. S. Volkov, D. K. Gramotnev*, et al.*, "Boosting local field enhancement by on-chip nanofocusing and impedance-matched plasmonic antennas," *Nano letters,* vol. 15, pp. 8148-8154, 2015.

[6]   R. Kirchain and L. Kimerling, "A roadmap for nanophotonics," *Nature Photonics,* vol. 1, p. 303, 2007.

[7]   H. Lu, X. Liu, G. Wang, and D. Mao, "Tunable high-channel-count bandpass plasmonic filters based on an analogue of electromagnetically induced transparency," *Nanotechnology,* vol. 23, p. 444003, 2012.

[8]   H. Wang, J. Yang, J. Zhang, J. Huang, W. Wu, D. Chen*, et al.*, "Tunable band-stop plasmonic waveguide filter with symmetrical multiple-teeth-shaped structure," *Optics letters,* vol. 41, pp. 1233-1236, 2016.

[9]   J. Tian, S. Yu, W. Yan, and M. Qiu, "Broadband high-efficiency surface-plasmon-polariton coupler with silicon-metal interface," *Applied Physics Letters,* vol. 95, p. 013504, 2009.

[10]   S. Bahadori-Haghighi, R. Ghayour, and M. H. Sheikhi, "All-Optical Cross-Bar Switch Based on a Low-Loss Suspended Graphene Plasmonic Coupler," *Plasmonics,* vol. 14, pp. 447-456, 2019.

[11]   N. Gogoi and P. P. Sahu, "All-optical tunable power splitter based on a surface plasmonic two-mode interference waveguide," *Applied optics,* vol. 57, pp. 2715-2719, 2018.

[12]   N. Nozhat and N. Granpayeh, "Analysis of the plasmonic power splitter and MUX/DEMUX suitable for photonic integrated circuits," *Optics Communications,* vol. 284, pp. 3449-3455, 2011.

[13]   Y. Guo, L. Yan, W. Pan, B. Luo, K. Wen, Z. Guo*, et al.*, "A plasmonic splitter based on slot cavity," *Optics Express,* vol. 19, pp. 13831-13838, 2011.

[14]   Y. Zhang, Y. Kuang, Z. Zhang, Y. Tang, J. Han, R. Wang*, et al.*, "High-sensitivity refractive index sensors based on Fano resonance in the plasmonic system of splitting ring cavity-coupled MIM waveguide with tooth cavity," *Applied Physics A,* vol. 125, p. 13, 2019.

[15]   Z. Zhang, J. Yang, X. He, J. Zhang, J. Huang, D. Chen*, et al.*, "Plasmonic refractive index sensor with high figure of merit based on concentric-rings resonator," *Sensors,* vol. 18, p. 116, 2018.

[16]   M. Butt, S. Khonina, and N. Kazanskiy, "Hybrid plasmonic waveguide-assisted Metal–Insulator–Metal ring resonator for refractive index sensing," *Journal of Modern Optics,* vol. 65, pp. 1135-1140, 2018.

[17]   Y. Shen, J. Zhou, T. Liu, Y. Tao, R. Jiang, M. Liu*, et al.*, "Plasmonic gold mushroom arrays with refractive index sensing figures of merit approaching the theoretical limit," *Nature communications,* vol. 4, p. 2381, 2013.

[18]   H. Wang, "Plasmonic refractive index sensing using strongly coupled metal nanoantennas: nonlocal limitations," *Scientific reports,* vol. 8, p. 9589, 2018.

[19]   O. Daneshmandi, A. Alighanbari, and A. Gharavi, "Characteristics of new hybrid plasmonic Bragg reflectors based on sinusoidal and triangular gratings," *Plasmonics,* vol. 10, pp. 233-239, 2015.

[20]   A. Hosseini and Y. Massoud, "A low-loss metal-insulator-metal plasmonic bragg reflector," *Optics express,* vol. 14, pp. 11318-11323, 2006.

[21]   J.-Q. Liu, L.-L. Wang, M.-D. He, W.-Q. Huang, D. Wang, B. Zou*, et al.*, "A wide bandgap plasmonic Bragg reflector," *Optics Express,* vol. 16, pp. 4888-4894, 2008.

[22]   C. Haffner, W. Heni, Y. Fedoryshyn, J. Niegemann, A. Melikyan, D. L. Elder*, et al.*, "All-plasmonic Mach–Zehnder modulator enabling optical high-speed communication at the microscale," *Nature Photonics,* vol. 9, p. 525, 2015.

[23]   Q. Gan, Y. Gao, and F. J. Bartoli, "Vertical plasmonic Mach-Zehnder interferometer for sensitive optical sensing," *Optics express,* vol. 17, pp. 20747-20755, 2009.

[24]   Y. Gao, Q. Gan, Z. Xin, X. Cheng, and F. J. Bartoli, "Plasmonic Mach–Zehnder interferometer for ultrasensitive on-chip biosensing," *ACS nano,* vol. 5, pp. 9836-9844, 2011.

[25]   J. Capmany and D. Novak, "Microwave photonics combines two worlds," *Nature photonics,* vol. 1, p. 319, 2007.

[26]   J. Capmany, B. Ortega, and D. Pastor, "A tutorial on microwave photonic filters," *Journal of Lightwave Technology,* vol. 24, pp. 201-229, 2006.

[27]   D. Liu, J. Wang, F. Zhang, Y. Pan, J. Lu, and X. Ni, "Tunable plasmonic band-pass filter with dual side-coupled circular ring resonators," *Sensors,* vol. 17, p. 585, 2017.

[28]   Y. Song, J. Wang, Q. Li, M. Yan, and M. Qiu, "Broadband coupler between silicon waveguide and hybrid plasmonic waveguide," *Optics express,* vol. 18, pp. 13173-13179, 2010.

[29]   M. Alam, J. Aitchison, and M. Mojahedi, "Polarization-independent hybrid plasmonic coupler for a silicon on insulator platform," *Optics letters,* vol. 37, pp. 3417-3419, 2012.

[30]   F. Lou, Z. Wang, D. Dai, L. Thylen, and L. Wosinski, "Experimental demonstration of ultra-compact directional couplers based on silicon hybrid plasmonic waveguides," *Applied Physics Letters,* vol. 100, p. 241105, 2012.

[31]   X. Gao, L. Zhou, X. Y. Yu, W. P. Cao, H. O. Li, H. F. Ma*, et al.*, "Ultra-wideband surface plasmonic Y-splitter," *Optics express,* vol. 23, pp. 23270-23277, 2015.

[32]   F. Lou, D. Dai, and L. Wosinski, "Ultracompact polarization beam splitter based on a dielectric–hybrid plasmonic–dielectric coupler," *Optics letters,* vol. 37, pp. 3372-3374, 2012.

[33]   K.-W. Chang and C.-C. Huang, "Ultrashort broadband polarization beam splitter based on a combined hybrid plasmonic waveguide," *Scientific reports,* vol. 6, p. 19609, 2016.

[34]   S. A. Maier, *Plasmonics: fundamentals and applications*: Springer Science & Business Media, 2007.

[35]   T. Wu, Y. Liu, Z. Yu, Y. Peng, C. Shu, and H. Ye, "The sensing characteristics of plasmonic waveguide with a ring resonator," *Optics express,* vol. 22, pp. 7669-7677, 2014.

[36]   T. Srivastava, R. Das, and R. Jha, "Highly sensitive plasmonic temperature sensor based on photonic crystal surface plasmon waveguide," *Plasmonics,* vol. 8, pp. 515-521, 2013.

[37]   M. Y. Azab, M. F. O. Hameed, and S. Obayya, "Temperature Sensors Based on Plasmonic Photonic Crystal Fiber," in *Computational Photonic Sensors*, ed: Springer, 2019, pp. 179-201.

[38]   A. Tittl, H. Giessen, and N. Liu, "Plasmonic gas and chemical sensing," *Nanophotonics,* vol. 3, pp. 157-180, 2014.

[39]   J. M. Bingham, J. N. Anker, L. E. Kreno, and R. P. Van Duyne, "Gas sensing with high-resolution localized surface plasmon resonance spectroscopy," *Journal of the American Chemical Society,* vol. 132, pp. 17358-17359, 2010.

[40]   A. G. Brolo, "Plasmonics for future biosensors," *Nature Photonics,* vol. 6, p. 709, 2012.

[41]   W.-C. Law, K.-T. Yong, A. Baev, and P. N. Prasad, "Sensitivity improved surface plasmon resonance biosensor for cancer biomarker detection based on plasmonic enhancement," *ACS nano,* vol. 5, pp. 4858-4864, 2011.

[42]   R. F. Oulton, V. J. Sorger, D. Genov, D. Pile, and X. Zhang, "A hybrid plasmonic waveguide for subwavelength confinement and long-range propagation," *nature photonics,* vol. 2, p. 496, 2008.

[43]   M. Rattier, H. Benisty, R. P. Stanley, J.-F. Carlin, R. Houdré, U. Oesterle*, et al.*, "Toward ultrahigh-efficiency aluminum oxide microcavity light-emitting diodes: Guided mode extraction

by photonic crystals," *IEEE Journal of selected topics in quantum electronics,* vol. 8, pp. 238-247, 2002.

[44]   J. Wierer, D. Kellogg, and N. Holonyak Jr, "Tunnel contact junction native-oxide aperture and mirror vertical-cavity surface-emitting lasers and resonant-cavity light-emitting diodes," *Applied physics letters,* vol. 74, pp. 926-928, 1999.

[45]   A. Melikyan, L. Alloatti, A. Muslija, D. Hillerkuss, P. C. Schindler, J. Li*, et al.*, "High-speed plasmonic phase modulators," *Nature Photonics,* vol. 8, p. 229, 2014.

[46]   Z. Liu, J. M. Steele, W. Srituravanich, Y. Pikus, C. Sun, and X. Zhang, "Focusing surface plasmons with a plasmonic lens," *Nano letters,* vol. 5, pp. 1726-1729, 2005.

[47]   H. Fischer and O. J. Martin, "Engineering the optical response of plasmonic nanoantennas," *Optics express,* vol. 16, pp. 9144-9154, 2008.

[48]   V. E. Ferry, L. A. Sweatlock, D. Pacifici, and H. A. Atwater, "Plasmonic nanostructure design for efficient light coupling into solar cells," *Nano letters,* vol. 8, pp. 4391-4397, 2008.

[49]   C. Min and G. Veronis, "Absorption switches in metal-dielectric-metal plasmonic waveguides," *Optics Express,* vol. 17, pp. 10757-10766, 2009.

[50]   X. Lu, R. Wan, and T. Zhang, "Metal-dielectric-metal based narrow band absorber for sensing applications," *Optics express,* vol. 23, pp. 29842-29847, 2015.

[51]   A. W. Sanders, D. A. Routenberg, B. J. Wiley, Y. Xia, E. R. Dufresne, and M. A. Reed, "Observation of plasmon propagation, redirection, and fan-out in silver nanowires," *Nano letters,* vol. 6, pp. 1822-1826, 2006.

[52]   H. Liu, Y. Gao, B. Zhu, G. Ren, and S. Jian, "A T-shaped high resolution plasmonic demultiplexer based on perturbations of two nanoresonators," *Optics Communications,* vol. 334, pp. 164-169, 2015.

[53]   G. Wang, H. Lu, X. Liu, D. Mao, and L. Duan, "Tunable multi-channel wavelength demultiplexer based on MIM plasmonic nanodisk resonators at telecommunication regime," *Optics Express,* vol. 19, pp. 3513-3518, 2011.

[54]   E. Ozbay, "Plasmonics: merging photonics and electronics at nanoscale dimensions," *science,* vol. 311, pp. 189-193, 2006.

[55]   H. A. Atwater, "The promise of plasmonics," *Sci. Am,* vol. 296, pp. 56-62, 2007.

[56]   E. Ferreiro-Vila, J. B. González-Díaz, R. Fermento, M. U. González, A. García-Martín, J. M. García-Martín*, et al.*, "Intertwined magneto-optical and plasmonic effects in Ag/Co/Ag layered structures," *Physical review B,* vol. 80, p. 125132, 2009.

[57]   P. R. West, S. Ishii, G. V. Naik, N. K. Emani, V. M. Shalaev, and A. Boltasseva, "Searching for better plasmonic materials," *Laser & Photonics Reviews,* vol. 4, pp. 795-808, 2010.

[58]   M. G. Blaber, M. D. Arnold, and M. J. Ford, "A review of the optical properties of alloys and intermetallics for plasmonics," *Journal of Physics: Condensed Matter,* vol. 22, p. 143201, 2010.

[59]   A. Ciattoni, C. Rizza, and E. Palange, "All-optical active plasmonic devices with memory and power-switching functionalities based on ε-near-zero nonlinear metamaterials," *Physical Review A,* vol. 83, p. 043813, 2011.

[60]   G. V. Naik and A. Boltasseva, "A comparative study of semiconductor-based plasmonic metamaterials," *Metamaterials,* vol. 5, pp. 1-7, 2011.

[61]   A. Grigorenko, M. Polini, and K. Novoselov, "Graphene plasmonics," *Nature photonics,* vol. 6, p. 749, 2012.

[62]   I. Tokarev and S. Minko, "Tunable plasmonic nanostructures from noble metal nanoparticles and stimuli-responsive polymers," *Soft Matter,* vol. 8, pp. 5980-5987, 2012.

[63]   H. Kim, M. Osofsky, S. Prokes, O. Glembocki, and A. Piqué, "Optimization of Al-doped ZnO films for low loss plasmonic materials at telecommunication wavelengths," *Applied Physics Letters,* vol. 102, p. 171103, 2013.

[64]   L. Gao, Y. Huo, J. S. Harris, and Z. Zhou, "Ultra-compact and low-loss polarization rotator based on asymmetric hybrid plasmonic waveguide," *IEEE Photonics Technology Letters,* vol. 25, pp. 2081-2084, 2013.

[65] S. Zuccon, P. Zuppella, M. Cristofani, S. Silvestrini, A. J. Corso, M. Maggini*, et al.*, "Functional palladium metal films for plasmonic devices: an experimental proof," *Journal of Optics,* vol. 16, p. 055001, 2014.

[66] W. Cao, J. Li, H. Chen, and J. Xue, "Transparent electrodes for organic optoelectronic devices: a review," *Journal of Photonics for Energy,* vol. 4, p. 040990, 2014.

[67] Y. Zhong, S. D. Malagari, T. Hamilton, and D. M. Wasserman, "Review of mid-infrared plasmonic materials," *Journal of Nanophotonics,* vol. 9, p. 093791, 2015.

[68] D. Y. Fedyanin, D. I. Yakubovsky, R. V. Kirtaev, and V. S. Volkov, "Ultralow-loss CMOS copper plasmonic waveguides," *Nano letters,* vol. 16, pp. 362-366, 2015.

[69] Z. Wei, X. Li, J. Yin, R. Huang, Y. Liu, W. Wang*, et al.*, "Active plasmonic band-stop filters based on graphene metamaterial at THz wavelengths," *Optics express,* vol. 24, pp. 14344-14351, 2016.

[70] J. Song, L. Zhang, Y. Xue, Q. Y. S. Wu, F. Xia, C. Zhang*, et al.*, "Efficient excitation of multiple plasmonic modes on three-dimensional graphene: An unexplored dimension," *ACS Photonics,* vol. 3, pp. 1986-1992, 2016.

[71] W. Heni, Y. Kutuvantavida, C. Haffner, H. Zwickel, C. Kieninger, S. Wolf*, et al.*, "Silicon–organic and plasmonic–organic hybrid photonics," *ACS Photonics,* vol. 4, pp. 1576-1590, 2017.

[72] Y. Ding, X. Guan, X. Zhu, H. Hu, S. I. Bozhevolnyi, L. K. Oxenløwe*, et al.*, "Efficient electro-optic modulation in low-loss graphene-plasmonic slot waveguides," *Nanoscale,* vol. 9, pp. 15576-15581, 2017.

[73] C. Hanske, M. N. Sanz-Ortiz, and L. M. Liz-Marzán, "Silica-Coated Plasmonic Metal Nanoparticles in Action," *Advanced Materials,* vol. 30, p. 1707003, 2018.

[74] M. Xia, "2D materials-coated plasmonic structures for SERS applications," *Coatings,* vol. 8, p. 137, 2018.

[75] R. Secondo, D. Fomra, N. Izyumskaya, V. Avrutin, J. Hilfiker, A. Martin*, et al.*, "Reliable modeling of ultrathin alternative plasmonic materials using spectroscopic ellipsometry," *Optical Materials Express,* vol. 9, pp. 760-770, 2019.

[76] L. D. Landau, J. Bell, M. Kearsley, L. Pitaevskii, E. Lifshitz, and J. Sykes, *Electrodynamics of continuous media* vol. 8: elsevier, 2013.

[77] D. P. Edward and I. Palik, "Handbook of optical constants of solids," ed: Academic, Orlando, Florida, 1985.

[78] A. D. Rakić, A. B. Djurišić, J. M. Elazar, and M. L. Majewski, "Optical properties of metallic films for vertical-cavity optoelectronic devices," *Applied optics,* vol. 37, pp. 5271-5283, 1998.

[79] D. Barchiesi and T. Grosges, "Fitting the optical constants of gold, silver, chromium, titanium, and aluminum in the visible bandwidth," *Journal of Nanophotonics,* vol. 8, p. 083097, 2014.

[80] M. G. Blaber, M. D. Arnold, and M. J. Ford, "Search for the ideal plasmonic nanoshell: the effects of surface scattering and alternatives to gold and silver," *The Journal of Physical Chemistry C,* vol. 113, pp. 3041-3045, 2009.

[81] J. B. Khurgin and A. Boltasseva, "Reflecting upon the losses in plasmonics and metamaterials," *MRS bulletin,* vol. 37, pp. 768-779, 2012.

[82] W. Cai, U. K. Chettiar, A. V. Kildishev, and V. M. Shalaev, "Optical cloaking with metamaterials," *Nature photonics,* vol. 1, p. 224, 2007.

[83] R. Cohen, G. Cody, M. Coutts, and B. Abeles, "Optical properties of granular silver and gold films," *Physical Review B,* vol. 8, p. 3689, 1973.

[84] Y. Yagil and G. Deutscher, "Transmittance of thin metal films near the percolation threshold," *Thin Solid Films,* vol. 152, pp. 465-471, 1987.

[85] F. Abelès, Y. Borensztein, and T. López-Rios, "Optical properties of discontinuous thin films and rough surfaces of silver," in *Advances in Solid State Physics*, ed: Springer, 1984, pp. 93-117.

[86] K. Fuchs, "The conductivity of thin metallic films according to the electron theory of metals," in *Mathematical Proceedings of the Cambridge Philosophical Society*, 1938, pp. 100-108.

[87]   F. Warkusz, "Electrical and mechanical properties of thin metal films: size effects," *Progress in Surface Science,* vol. 10, pp. 287-382, 1980.

[88]   E. Kretschmann, "Decay of non radiative surface plasmons into light on rough silver films. Comparison of experimental and theoretical results," *Optics Communications,* vol. 6, pp. 185-187, 1972.

[89]   D.-L. Hornauer, "Light scattering experiments on silver films of different roughness using surface plasmon excitation," *Optics Communications,* vol. 16, pp. 76-79, 1976.

[90]   Y.-H. Chou, C.-J. Chang, T.-R. Lin, and T.-C. Lu, "Surface plasmon polariton nanolasers: Coherent light sources for new applications," *Chinese Physics B,* vol. 27, p. 114208, 2018.

[91]   W. Campbell and U. Thomas, "Films on freshly abraded copper surfaces," *Nature,* vol. 142, p. 253, 1938.

[92]   G. H. Chan, J. Zhao, E. M. Hicks, G. C. Schatz, and R. P. Van Duyne, "Plasmonic properties of copper nanoparticles fabricated by nanosphere lithography," *Nano Letters,* vol. 7, pp. 1947-1952, 2007.

[93]   H. Bennett, R. Peck, D. Burge, and J. Bennett, "Formation and growth of tarnish on evaporated silver films," *Journal of applied physics,* vol. 40, pp. 3351-3360, 1969.

[94]   D. Burge, J. Bennett, R. Peck, and H. Bennett, "Growth of surface films on silver," *Surface science,* vol. 16, pp. 303-320, 1969.

[95]   G. Bemski, "Recombination properties of gold in silicon," *Physical Review,* vol. 111, p. 1515, 1958.

[96]   L. Yau and C. Sah, "Measurement of trapped-minority-carrier thermal emission rates from Au, Ag, and Co traps in silicon," *Applied Physics Letters,* vol. 21, pp. 157-158, 1972.

[97]   J. A. Dionne, L. A. Sweatlock, M. T. Sheldon, A. P. Alivisatos, and H. A. Atwater, "Silicon-based plasmonics for on-chip photonics," *IEEE Journal of Selected Topics in Quantum Electronics,* vol. 16, pp. 295-306, 2010.

[98]   A. Hryciw, Y. C. Jun, and M. L. Brongersma, "Plasmonics: Electrifying plasmonics on silicon," *Nature materials,* vol. 9, p. 3, 2010.

[99]   R. Soref, J. Hendrickson, and J. W. Cleary, "Mid-to long-wavelength infrared plasmonic-photonics using heavily doped n-Ge/Ge and n-GeSn/GeSn heterostructures," *Optics express,* vol. 20, pp. 3814-3824, 2012.

[100]   B. S. Williams, "Terahertz quantum-cascade lasers," *Nature photonics,* vol. 1, p. 517, 2007.

[101]   T. Minami, "Transparent conducting oxide semiconductors for transparent electrodes," *Semiconductor science and technology,* vol. 20, p. S35, 2005.

[102]   G. J. Exarhos and X.-D. Zhou, "Discovery-based design of transparent conducting oxide films," *Thin solid films,* vol. 515, pp. 7025-7052, 2007.

[103]   L. Wang, C. Clavero, K. Yang, E. Radue, M. Simons, I. Novikova*, et al.*, "Bulk and surface plasmon polariton excitation in RuO 2 for low-loss plasmonic applications in NIR," *Optics express,* vol. 20, pp. 8618-8628, 2012.

[104]   J. Cleary, R. Peale, D. Shelton, G. Boreman, C. Smith, M. Ishigami*, et al.*, "IR permittivities for silicides and doped silicon," *JOSA B,* vol. 27, pp. 730-734, 2010.

[105]   K. S. Novoselov, V. Fal, L. Colombo, P. Gellert, M. Schwab, and K. Kim, "A roadmap for graphene," *nature,* vol. 490, pp. 192-200, 2012.

[106]   M. G. Saber, Z. Xing, D. Patel, E. El-Fiky, N. Abadía, Y. Wang*, et al.*, "A CMOS compatible ultracompact silicon photonic optical add-drop multiplexer with misaligned sidewall Bragg gratings," *IEEE Photonics Journal,* vol. 9, pp. 1-10, 2017.

[107]   D. Thomson, A. Zilkie, J. E. Bowers, T. Komljenovic, G. T. Reed, L. Vivien*, et al.*, "Roadmap on silicon photonics," *Journal of Optics,* vol. 18, p. 073003, 2016.

[108]   R. Soref, "The past, present, and future of silicon photonics," *IEEE Journal of selected topics in quantum electronics,* vol. 12, pp. 1678-1687, 2006.

[109]   A. Hryciw, "Jun. YC & Brongersma, ML Electrifying plasmonics on silicon," *Nature Mater,* vol. 9, pp. 3-4, 2010.

[110] R. Soref, "Mid-infrared photonics in silicon and germanium," *Nature photonics,* vol. 4, p. 495, 2010.

[111] M. Balkanski, A. Aziza, and E. Amzallag, "Infrared Absorption in Heavily Doped n-Type Si," *physica status solidi (b),* vol. 31, pp. 323-330, 1969.

[112] D. K. Schroder, R. N. Thomas, and J. C. Swartz, "Free carrier absorption in silicon," *IEEE Journal of solid-state circuits,* vol. 13, pp. 180-187, 1978.

[113] F. A. Trumbore, "Solid solubilities of impurity elements in germanium and silicon," *Bell System Technical Journal,* vol. 39, pp. 205-233, 1960.

[114] H. Barber, "Effective mass and intrinsic concentration in silicon," *Solid-State Electronics,* vol. 10, pp. 1039-1051, 1967.

[115] M. Shahzad, G. Medhi, R. E. Peale, W. R. Buchwald, J. W. Cleary, R. Soref*, et al.*, "Infrared surface plasmons on heavily doped silicon," *Journal of Applied Physics,* vol. 110, p. 123105, 2011.

[116] M. G. Saber, N. Abadía, and D. V. Plant, "CMOS compatible all-silicon TM pass polarizer based on highly doped silicon waveguide," *Optics express,* vol. 26, pp. 20878-20887, 2018.

[117] Z. Qi, G. Hu, L. Li, B. Yun, R. Zhang, and Y. Cui, "Design and analysis of a compact soi-based aluminum/highly doped p-type silicon hybrid plasmonic modulator," *IEEE Photonics Journal,* vol. 8, pp. 1-11, 2016.

[118] Y.-B. Chen and Z. Zhang, "Heavily doped silicon complex gratings as wavelength-selective absorbing surfaces," *Journal of Physics D: Applied Physics,* vol. 41, p. 095406, 2008.

[119] M. Van Exter and D. Grischkowsky, "Carrier dynamics of electrons and holes in moderately doped silicon," *Physical Review B,* vol. 41, p. 12140, 1990.

[120] S. Basu, B. J. Lee, and Z. Zhang, "Near-field radiation calculated with an improved dielectric function model for doped silicon," *Journal of Heat Transfer,* vol. 132, p. 023302, 2010.

[121] G. Masetti, M. Severi, and S. Solmi, "Modeling of carrier mobility against carrier concentration in arsenic-, phosphorus-, and boron-doped silicon," *IEEE Transactions on electron devices,* vol. 30, pp. 764-769, 1983.

[122] P. P. Silvester and R. L. Ferrari, *Finite elements for electrical engineers*: Cambridge university press, 1996.

[123] K. J. Binns, C. Trowbridge, and P. Lawrenson, *The analytical and numerical solution of electric and magnetic fields*: Wiley, 1992.

[124] P. Dular, W. Legros, H. De Gersem, and K. Hameyer, "Floating potentials in various electromagnetic problems using the finite element method," in *Proceedings of 4th International workshop on Electric and Magnetic fields*, 1998, pp. 409-414.

[125] S. Zou, F. Wang, R. Liang, L. Xiao, and M. Hu, "A nanoscale refractive index sensor based on asymmetric plasmonic waveguide with a ring resonator: A review," *IEEE Sensors Journal,* vol. 15, pp. 646-650, 2014.

[126] D. Nobili, S. Solmi, A. Parisini, M. Derdour, A. Armigliato, and L. Moro, "Precipitation, aggregation, and diffusion in heavily arsenic-doped silicon," *Physical Review B,* vol. 49, p. 2477, 1994.

[127] S. Naghizadeh and Ş. E. Kocabaş, "Guidelines for designing 2D and 3D plasmonic stub resonators," *JOSA B,* vol. 34, pp. 207-217, 2017.

[128] X. Zhang, Y. Qi, P. Zhou, H. Gong, B. Hu, and C. Yan, "Refractive index sensor based on fano resonances in plasmonic waveguide with dual side-coupled ring resonators," *Photonic Sensors,* vol. 8, pp. 367-374, 2018.

[129] Z. Tu, D. Gao, M. Zhang, and D. Zhang, "High-sensitivity complex refractive index sensing based on Fano resonance in the subwavelength grating waveguide micro-ring resonator," *Optics express,* vol. 25, pp. 20911-20922, 2017.